



HAL
open science

Design and implementation of piezoelectric technology based power devices

Yuan-Ping Liu

► **To cite this version:**

Yuan-Ping Liu. Design and implementation of piezoelectric technology based power devices. Micro and nanotechnologies/Microelectronics. École normale supérieure de Cachan - ENS Cachan, 2009. English. NNT: . tel-00505837

HAL Id: tel-00505837

<https://theses.hal.science/tel-00505837>

Submitted on 26 Jul 2010

HAL is a multi-disciplinary open access archive for the deposit and dissemination of scientific research documents, whether they are published or not. The documents may come from teaching and research institutions in France or abroad, or from public or private research centers.

L'archive ouverte pluridisciplinaire **HAL**, est destinée au dépôt et à la diffusion de documents scientifiques de niveau recherche, publiés ou non, émanant des établissements d'enseignement et de recherche français ou étrangers, des laboratoires publics ou privés.

國立臺灣大學工學院工程科學及海洋工程研究所

博士論文

Department of Engineering Science and Ocean Engineering

College of Engineering

National Taiwan University

Doctoral Dissertation

壓電功率轉換裝置的設計與實現

Design and Implementation of Piezoelectric Technology Based

Power Devices



Yuan-Ping Liu

指導教授：李世光 博士、吳文中 博士

François Costa 博士、Dejan Vasic 博士

Advisors: Chih-Kung Lee, Ph.D., Wen-Jong Wu, Ph.D.

François Costa, Ph. D., Dejan Vasic, Ph. D.

中華民國 98 年 10 月

October, 2009

國立臺灣大學博士學位論文
口試委員會審定書

壓電功率轉換裝置的設計與實現

Design & Implementation
of Piezoelectric Technology Based Power Devices

本論文係劉元平君（學號：F93525013）在國立臺灣大學工程科學及海洋工程學系完成之博士學位論文，於民國 98 年 10 月 19 日承下列考試委員審查通過及口試及格，特此證明

口試委員：

李世光 李世光 *Chih-Kyung* 吳文中 吳文中 *Wen-Tzyng Wu*
(指導教授)

François Costa Costa Dejan Vasic Vasic
(指導教授)

吳光鐘 吳光鐘 *Huang-Chong Wu*

陳秋麟 陳秋麟 *Chen-Lin Chen*

謝宗霖 謝宗霖 *Shieh-Lih*

系主任

宋家驥 宋家驥 (簽名)

中文摘要

本文係發展壓電材料做為多種電力轉換裝置的關鍵元件，進而發展出壓電式電力轉換裝置。不同於目前電力轉換器使用要是用電磁變壓器做為電能轉換關鍵元件，本論文使用壓電變壓器做為電力轉換器的關鍵元件。研究目的是希望以壓電變壓器取代電磁變壓器，來降低系統的電磁干擾、薄型化和提高轉換器的能量密度。本文主要分成壓電式冷陰極管換流器、壓電式直流對直流轉換器和壓電饋入整流器的最佳化三大部分。以往壓電變壓器主要是從最佳負載的概念做為設計的基礎。然而，實際的電力轉換器需要有電壓或電流調節的功能，在考慮電壓和電流調節的情況下，最佳負載的概念並不適合作為設計的依據。本論文改從壓電變壓器物理特性振動速度做為設計的依據，使壓電變壓器的設計更為清楚而簡潔。提出創新的設計方法使壓電變壓器的主要損耗可以被清晰的預測，而溫度的上升也可從本文所提出的設計方法中得到良好的預測趨勢。壓電式冷陰極管換流器和壓電式直流對直流轉換器都藉由此設計流程的概念，成功的設計出符合實際規格與需求的壓電變壓器，並分別實際應用在 32 吋液晶電視和 10 瓦的直流電源供應器上。此外，本論文同時分析壓電式直流對直流轉換器的電磁干擾問題。雖然壓電本身並輻射性電磁干擾的問題，使得壓電式電源轉換器有傳導性電磁干擾的問題。由於壓電的寄生電容和外接整流器的特性，使得壓電式電源轉換器的電磁干擾問題相當不同於電磁式的電源轉換器。詳細的傳導性電磁干擾分析和模型都在本論文中被分析與詳述。此外，在直流負載的考量下，由於壓電式饋入整流器為一非線性裝置，不易分析與設計。本論文提出使用壓電片的能量工作迴圈的概念，簡化過往分析複雜的問題。此外，本論文更藉由分析結果，提出最佳化的速度控制式壓電式饋入整流器。並將此技術成功的應用在壓電結構阻尼的應用上。

關鍵詞：壓電變壓器、切換式電源、諧振式電源供應器、切換式阻尼、智能結構



Abstract

In this dissertation, the piezoelectric materials were adopted to make the key components in the power device, and were further developed to piezoelectric technology based power converters. The main purpose of this dissertation is that using the piezoelectric transformers as the key component to replace the electromagnetic transformers in some power converters. The piezoelectric transformers based converter can reduce the electromagnetic interference (EMI), thickness of the converters and increase the power density of the converter. Cold cathode fluorescent lamp based inverters, DC/DC converters and the optimization of the piezoelectric layer fed rectifiers are the three main parts in this dissertation. Previous researches used the concept of the optimal loading condition as the major design criterion. However, the practical power converter requires the current or voltage regulation. Considering the power converters with the current or voltage regulation, the concept of the optimal loading condition is not suitable to be the major design criterion. In this dissertation, the vibration velocity was adopted as the major design parameter, which makes the design of the piezoelectric transformer becomes easier and clearer compared to the typical design rule. The proposed design procedure can predict the temperature rise as well as the losses of the piezoelectric transformers clearly. Both cold cathode fluorescent lamp based inverters

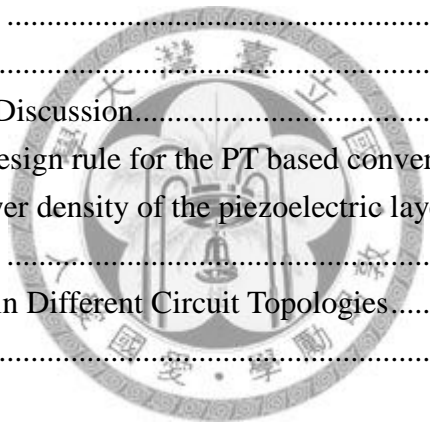
and DC/DC converters can be designed to fit the requirements and the specifications well by the proposed design rule. The 32 inches LCDTV inverter and 10Watt DC/DC converter were fully developed successfully based on the proposed design procedure. In addition, although the piezoelectric transformer itself does not have to radiated EMI problem, it owns the conducted EMI problem. According to effect of the parasitic capacitor and the connected rectifier of the piezoelectric transformers, the EMI behaviour of the piezoelectric transformers based converter is quite different from the typical converters. The model and analysis of the EMI were detail in this dissertation. On the other hand, the piezoelectric layer fed rectifier is a non-linear device, which is not easy to analyze in general. The concept of the work cycle was proposed to simplify the analysis and the design. Based on the work cycle, the velocity controlled piezoelectric layer fed rectifier was proposed to optimize the energy flow of the piezoelectric layer. This technique was also applied to the structural damping, which can suppress the structure vibration effectively.

Keywords: piezoelectric transformer, switching power supply, resonant power supply, switching damping, smart structure

CONTENTS

中文摘要	i
Abstract.....	iii
Contents.....	v
List of Figures.....	vii
List of Tables	xi
Chapter 1 Introduction.....	1
1.1 Backgrounds and motivations	1
1.2 Major results	6
Chapter 2 Basic Theory of Piezoelectricity.....	9
2.1 Piezoelectric structures	10
2.2 The vibration of the piezoelectric structures	13
2.3 The theory of deformation/vibration	16
2.4 The equivalent circuit of the piezoelectric structure	21
2.5 Piezoelectric materials with external shunt circuits	24
2.6 Summary.....	27
Chapter 3 Piezoelectric Transformers.....	29
3.1 The configurations of the piezoelectric transformers	29
3.2 Characteristics of the PT connected with a linear load	36
3.3 The input driving circuits of PTs.....	43
3.4 Summary.....	58
Chapter 4 Rosen-type Piezoelectric Transformers based CCFL Inverters	61
4.1 The characteristics of the CCFL (cold cathode fluorescent lamp)	61
4.2 Physical limitations of the PT and the CCFL	66
4.3 Design of the Rosen-type PT based CCFL inverter	70
4.4 Summary.....	86
Chapter 5. Piezoelectric Transformer based DC/DC Converter.....	89
5.1 Analysis of Piezoelectric Transformer fed Voltage-Mode Rectifiers	90
5.1.1 Topologies of the PT fed rectifiers	90
5.1.2 State equation of the slow system.....	94
5.1.3 State equation of the PT output capacitor.....	98
5.1.4 State Equations of the Fast System.....	100
5.1.5 Selection of the PT fed rectifiers	106
5.2 Design of Piezoelectric Transformer based DC/DC converter.....	108
5.2.1 The relationship between the PT fed rectifier and the mechanical current	108

5.2.2 Dimensional constraints of the PT configurations	116
5.2.3 Energy Balance	122
5.2.4 Experimental Model Correction	125
5.2.5 Design of the Multilayer Disk-type PT	128
5.3 EMI Analysis of a DC/DC Converter Using a Piezoelectric Transformer ...	138
5.3.1 Background.....	138
5.3.2 EMI Emission in the DC/DC Converter.....	140
5.3.3 Circuit Models for conducted EMI.....	147
5.3.4 Experimental Results and Discussions	151
5.4 Summary.....	155
Chapter 6 Velocity controlled Piezoelectric Layer fed Rectifiers	157
6.1 Work Cycle Observation for the Piezoelectric Layer	157
6.2 Velocity-Controlled Switching Piezoelectric Damping.....	165
6.3 Analysis of velocity-controlled switching piezoelectric damping.....	173
6.4 Experiment Setup	177
6.5 Summary.....	183
Chapter 7 Summary and Discussion.....	185
7-1. The systematic design rule for the PT based converter.....	185
7-2. Examine the power density of the piezoelectric layer.....	189
7-3. The future works	189
Appendix A. Work Cycles in Different Circuit Topologies.....	193
Reference.....	193



List of Figures

Figure 2-1. The basic configuration of the piezoelectric structure.....	11
Figure 2-2. The configuration of the multilayer piezoelectric structure.....	11
Figure 2-3. The equivalent circuit of the piezoelectric structure.....	22
Figure 2-4. The single mode equivalent circuit of piezoelectric layer	23
Figure 2-5. The equivalent circuit of the piezoelectric layer with mechanical current source.....	24
Figure 2-6. Piezoelectric layer with a shunt circuit	26
Figure 2-7. The internal feedback system of the shunt circuit	27
Figure 2-8. The internal feedback system of the shunt circuit with capacitor charging.	27
Figure 3-1. (a) input section of the PT (piezoelectric actuator) (b) output section of the PT (piezoelectric harvester).....	31
Figure 3-2. (a) Combining two piezoelectric layers (b) the single mode equivalent circuit of the PT with the load	33
Figure 3-3. The internal loop of the PT	36
Figure 3-4. The measurement of the mechanical current	36
Figure 3-5. The single mode equivalent circuit of the PT with the load	37
Figure 3-6. (a) The voltage gain and (b) the power characteristics of the PT with resistive load	38
Figure 3-7. The equivalent circuit of PT with a resistive load	39
Figure 3-8. (a) The voltage gain and (b) the power characteristics of the PT with series inductor and resistive load	42
Figure 3-9. (a) The voltage gain and (b) the power characteristics of the PT with parallel inductor and resistive load	43
Figure 3-10. The half-bridge driving circuits with a piezoelectric transformer	45
Figure 3-11. The operation of the ZVS-mode half-bridge circuit with a PT.....	49
Figure 3-12. The waveforms of the ZVS-mode half-bridge circuit with a piezoelectric transformer.....	49
Figure 3-13. The anticipated relationship between the voltage v_{ds2} and the input current i_1	53
Figure 3-14. The impedance and phase of the (a) LC resonance (b) PT with the load variation	56
Figure 3-15. (a) The impedance magnitude and (b) impedance phase of piezoelectric transformers with a series inductor.....	57
Figure 4-1 (a) The voltage-current curve and (b) The power-resistance curve of the lighting CCFL.....	62
Figure 4-2. The small-signal perturbation of the fluorescent lamp operating at high	

frequency	64
Figure 4-3. Equivalent circuit of half-bridge PT based CCFL inverter.....	66
Figure 4-4. PT fed by resistive load	67
Figure 4-5. The mechanical currents versus lengths of the Rosen-type PT with (a) different lamp currents (b) different products of the PT width and the PT thickness	69
Figure 4-6. Output power of the piezoelectric transformer (a) versus frequencies (b) versus loads	71
Figure 4-7. The dimensional variation of the Rosen-type piezoelectric transformers: (a) length (a) width (c) thickness	80
Figure 4-8. the fully optimal procedure of the single-layer Rosen-type piezoelectric transformer.....	82
Figure 4-9. optimal width and thickness of piezoelectric transformers with length 53mm	83
Figure 4-10. The specimens of the Rosen-type piezoelectric transformers.....	84
Figure 4-11. The piezoelectric transformer based inverter for two CCFLs.....	85
Figure 4-12. The piezoelectric transformer based inverter for commercial 32” LCDTV backlight	86
Figure 5-1. The block diagram of the PT based DC/DC converter	91
Figure 5-2. High-bridge PT based DC/DC converter with voltage mode rectifier	92
Figure 5-3. The PT fed (a) half wave and (b) full-wave voltage-mode rectifier	93
Figure 5-4. The voltage and current waveform in the input side of (a) the half wave and (b) the full-wave voltage-mode rectifier.....	93
Figure 5-5. The equivalent circuit of the fast system	101
Figure 5-6. The block diagram of the converter (a) large signal dynamic model (b) small signal dynamic model.....	104
Figure 5-7. The block diagram of the converter.....	105
Figure 5-8. Voltage and current waveforms of the PT fed full-wave rectifier.....	108
Figure 5-9. (a) Mechanical current and (b) efficiency with load variations when the diode voltage drop is neglected.	114
Figure 5-10. (a) Mechanical current and (b) efficiency with load variations when the contribution of the load voltage is neglected.....	114
Figure 5-11. (a) Mechanical current and (b) efficiency with load variations when α value is fixed ($\alpha = 7$).....	116
Figure 5-12. (a) uniformly-poled longitudinal PT, (b) uniformly-poled disk-type PT, (c) stacked disk-type PT.....	118
Figure 5-13. side view of the stacked disk-type PT	119
Figure 5-14. Measurement of the mechanical current.....	126

Figure 5-15. (a) quality factor and (b) mechanical current versus numbers of layers..	128
Figure 5-16. The design flow of the PT.....	130
Figure 5-17. The waveform of the input voltage v_{in} (dotted line) and the input current (solid line).....	136
Figure 5-18. The waveform of the rectifier voltage v_{rec} (dotted line) and the rectifier current i_{rec} (solid line)	137
Figure 5-19. The burst-mode input current of PT-1	137
Figure 5-20. The total efficiency of the proposed converter: (a) PT-1 (b) PT-2 (solid line: prediction, dot: measurement)	138
Figure 5-21. The temperature rise of (a) PT-1 (b) PT-2 (solid line: prediction, dot: measurement).....	138
Figure 5-22. The block diagram of the piezoelectric transformer based DC/DC converter	140
Figure 5-23. Circuit topology of a half-bridge DC/DC converter using a piezoelectric transformer with the series inductor	141
Figure 5-24. Equivalent circuit of the DC-DC converter with LISN setup for common mode noises measurement.....	142
Figure 5-25. Pictures of the stacked disk-type piezoelectric transformer operating in radial mode	143
Figure 5-26 Equivalent circuit of the PT parasitic capacitances coupling common mode noises	144
Figure 5-27. Experimental setup for the measurement on conducted noise in the PT based DC/DC converter.....	145
Figure 5-28. The PT and the half-bridge circuit connecting configurations: (a) middle point of the half-bridge is connected with the PT top electrode; (b) middle point of the half-bridge is connected with the PT bottom electrode	146
Figure 5-29. Experimental circuit board for measurement on conducted noises in a PT based DC-DC converter.....	146
Figure 5-30. The equivalent circuit model for the common mode current analysis.....	147
Figure 5-31. The waveforms in the configuration of Figure 5-28a.....	148
Figure 5-32. The waveforms of the common mode current i_{cm} and the PT output voltage in the configuration of Figure 5-28 (b).....	150
Figure 5-33. Complete circuit model with parasitic effects on the common mode noises conduction used in PSIM simulation.....	151
Figure 5-34. The simulation results of the common mode current i_{cm} : (a) i_{cm} in configuration of Figure 5-28a (b) i_{cm} in configuration of Figure 5-28b ...	151
Figure 5-35. Left plots: waveforms v_{K2} in 10V/div and v_{rec} in 10V/div of configuration Figure 5-28a.....	152

Figure 5-36. The spectrum of the common mode current when middle point of the half-bridge is connected at the top PT electrode (the configuration of Figure 5-28a).....	154
Figure 5-37. The spectrum of the common mode current when middle point of the half-bridge is connected at the bottom PT electrode. (the configuration of Figure 5-28b)	155
Figure 6-1. Mechanical and electrical coupling of the piezoelectric 31-type vibration	158
Figure 6-2. The block diagram of the velocity-controlled piezoelectric layer fed rectifier	162
Figure 6-3. The velocity controlled piezoelectric layer fed rectifier (VPR).....	162
Figure 6-4. The ideal waveform of the velocity controlled piezoelectric fed switching rectifier.....	162
Figure 6-5. Equivalent circuit of the PT with a shunt circuit	166
Figure 6-6. The system block diagram and circuit topology of the VSPD system	168
Figure 6-7. The piezoelectric resonant shunt damping topology	171
Figure 6-8. The work cycle of the piezoelectric resonant shunt damping topology (a) mismatches the resonant frequency (b) matches the resonant frequency (solid line: the apparent work cycle; dotted line: the real work cycle).....	172
Figure 6-9. The work cycles (the apparent work cycle and the real work cycle overlapping) of VSPD	173
Figure 6-10. Experimental setup of the piezoelectric switching damping	178
Figure 6-11. The frequency response the VSPD system	181
Figure 6-12. The experimental waveform of the VSPD system (a) the displacement and the voltage waveforms (b) the work cycle.....	182
Figure 6-13. The experimental results (points) and the theoretical prediction (line) of the VSPD	182
Figure 6-14. The experimental results (points) and the theoretical prediction (line) of the maximum dc voltage (Red points: 16.6Hz, Blue points: 16.5Hz, Green points: 16.4Hz)	183

List of Tables

Table 2-1. Three kinds of piezoelectric materials.....	10
Table 2-2. The manufacturing process of the piezoelectric ceramics.....	11
Table 2-3. The self-vibration modes of the piezoelectric structures.....	15
Table 2-4. The first mode equivalent circuit of different vibration type piezoelectric layer	23
Table 3-1. Different types of PTs.....	31
Table 3-2. The relationship between the dimensional factors and the electrical equivalent components	33
Table 3-3. The tested PT model	38
Table 3-4. The equivalent circuit of the PT output capacitor with different loads	42
Table 3-5. The comparison of the practical input driving circuits.....	44
Table 3-6. The basic operation of the half-bridge circuit	45
Table 3-7. The operation of the ZVS-mode half-bridge circuit with a PT	50
Table 3-8. The relationship between the voltage v_{ds2} and the input current i_1 in different frequencies.....	54
Table 3-9. The constraints for ZVS conditions.....	57
Table 4-1. The equivalent circuit of the Rosen-type piezoelectric transformer	69
Table 4-2. The Material properties of the Rosen-type PT.....	69
Table 4-3. A piezoelectric transformer testing model.....	71
Table 4-4. The design constraints of the Rosen-type PT	77
Table 4-5. The testing size of the Rosen-type PT	79
Table 4-6. the specification of CCFL in LCDTV	82
Table 4-7. Specimens of Rosen-type piezoelectric transformers	85
Table 4-7. The testing of optimal piezoelectric transformer based inverter	85
Table 5-1. The characteristics of PT fed voltage mode rectifier.....	97
Table 5-2. The relationship between the dimensional parameter and the equivalent circuit of the stacked disk-type PT	121
Table 5-3. the result of the design example	132
Table 5-4. The PT-1 specimen for the experiment.....	133
Table 5-5. The PT-2 specimen for the experiment.....	133
Table 5-6. Geometrical dimensions of the PT under test.....	143
Table 5-7. Component values in the LISN setup.....	145
Table 6-1. The work cycles with the basic waveforms.....	159
Table 6-2. Six PT fed rectifiers.....	164
Table 6-3. The operation of the VSPD	168
Table 6-4. Comparison between SSDV and VSPD techniques.	176

Table 6-5. The piezoelectric layer and Steel Beam 178
Table 6-6. The model parameters of the piezoelectric/beam system..... 179



Chapter 1. Introduction

1.1 Backgrounds and Motivations

In our daily life, most of electronic devices need to be connected with power supplies or with batteries. However, electronics require different voltage. A converter can change the voltage and the waveform of an electrical power source, so it becomes an indispensable device. One of the key components in a converter is the transformer which can change the AC voltage from input primary (input) side to secondary (output) side while insulating the device. The classical electromagnetic transformer was developed based in Faraday's law in 1831. The electromagnetic transformer transfers electrical energy into magnetic energy, then back to electrical energy with voltage and current conversion. However, the magnetic field can be partially radiated because it is not fully enclosed in the magnetic material. Another kind of the transformer called piezoelectric transformer was thus proposed in 1958. [1] Piezoelectric transformers are based on the piezoelectric effect which was discovered by French people Pierre and Jacques Curie in 1880. Different from the electromagnetic transformer, piezoelectric transformer achieves the voltage conversion by structural vibration. The vibration energy can be transmitted in an enclosed structure which can be viewed as a waveguide. Therefore, piezoelectric transformers have higher power density and higher efficiency than the electromagnetic transformers in general. Moreover, compared to

electromagnetic transformers, piezoelectric transformers have several inherent advantages such as no electromagnetic interference (EMI) radiation, a thin housing profile, nonflammable, higher power density, and simpler automated manufacturing processes. Therefore, piezoelectric transformers are potential components which can replace the electromagnetic transformer in some applications.

On the other hand, energy is a very important issue according to the global warming. A part of generated energy may be lost during the transmission and the voltage conversion. To save energy, an efficient energy conversion is a topic of interest. The switching mode power supplies (SMPS) were proposed to improve the efficiency of typical linear power converters. Different from linear power converters operating at the frequency of power line (60Hz in Taiwan and 50Hz in Europe), SMPS operates in ultrasonic frequency range leading to decrease drastically the size of transformers. Piezoelectric transformers are also operating in ultrasonic frequency range, so piezoelectric transformers can be integrated with the SMPS.

Therefore, the major trust of this dissertation is to develop the design rules for piezoelectric transformers in SMPS and to find the optimal interface circuit topology between the SMPS and the piezoelectric transformers. The typical design rule is based on the optimal loading condition. The optimal loading condition means the most efficient condition. The typical optimal loading condition [2, 3] is derived from the

open-loop characteristics without dealing with any voltage or current regulations. However, in practice, the load voltage or load current is required to be regulated with a constant value. To discover the newly most efficient operating condition of piezoelectric transformers with the close-loop control, the vibration velocity of piezoelectric transformers is examined in detail and is adopted as the main design parameter in this dissertation. The vibration velocity is the physical limitation of piezoelectric transformers. [4, 5] However, the vibration velocity was not adopted as the design parameters of piezoelectric transformers. In fact, the vibration velocity is related to the losses in piezoelectric transformers significantly. Examining the vibration velocity of the piezoelectric transformer can understand the losses clearly in different operating conditions. Therefore, the vibration velocity is suitable to be the design parameter of the piezoelectric transformers with the close-loop regulation. Two kinds of the piezoelectric transformers based converters, CCFL (cold cathode fluorescent lamps) inverter and the DC/DC converter, which are describe as following paragraphs.

Liquid crystal displays (LCDs) are the most popular flat display panels. The thinner flat display panels were pursued to save the living space and to increase the portability. The thickness of the flat display panels can be limited by the electromagnetic transformer of the inverter circuit. Since piezoelectric transformers have the thinner profile compared to electromagnetic transformers, it can replace electromagnetic

transformers potentially. In addition, some characteristics of piezoelectric transformers fit the requirements of the CCFL, such as pure sinusoidal output voltage and the high output voltage/low output current. Many researchers worked on the different parts of the piezoelectric CCFL inverter, such as the structure of the piezoelectric transformers [6], the electrode of the piezoelectric transformers [7, 8, 9] and control strategy. [10] In this dissertation, we do not focus on the specific part in the inverter, but on a general design procedure of the piezoelectric transformers and corresponding circuit topology under the constant load current condition (constant brightness condition). Examining the CCFL load characteristics and vibration velocity of piezoelectric transformers leads to a new loading condition. The loading conditions are different from the typical optimal loading condition, which gives designer a straightforward and simple criterion for designing the piezoelectric transformer based CCFL inverter.

As to the DC/DC converter, piezoelectric transformer fit the tide of miniaturization and the system integration due to the profile and the electromagnetic compatibility (EMC). In such a case, a rectifier has to be connected to the output section of the piezoelectric transformer to obtain the DC voltage. The design of the piezoelectric transformer becomes more complex due to the nonlinearity of the rectifier. In addition, the practical use of the DC/DC converter is to supply a low voltage but high current load, which is opposite the characteristic of piezoelectric transformers. Lin and Lee first

proposed a design flow of a piezoelectric transformer in the use of the DC/DC converter.

[11, 12] In his paper, Lin states that the rectifier is equivalent to a pure resistor because the characteristics of the piezoelectric transformer are well-known in this case. This

method developed by Lin has been widely used to simplify design procedures of the piezoelectric transformers, especially for resonant converters. However, this method is

only correct when the input voltage and the input current of the rectifier are in phase at the operating frequency. If a phase difference exists between the voltage and the current,

the equivalent impedance requires involving a reactive component. In most cases, it

usually exists a phase difference between the input voltage and input current of the piezoelectric transformers fed rectifier. [13, 14] The underlying reason lies in the output

capacitor of the piezoelectric transformer, which needs to be charged and discharged at each period. Moreover, the phase difference varies with the operating frequency and the

load values. In other words, the phase difference cannot be neglected. Therefore, it is

important to examine the output voltage/current waveforms of the piezoelectric transformer directly and then incorporate it into the design procedure of the

piezoelectric transformer. In this dissertation, the relationship between the vibration velocity and the waveforms of the piezoelectric transformer fed rectifier is analyzed in

detail to develop the general design procedure of the piezoelectric transformers under the constant load voltage condition. Then, the conducted electromagnetic interference

(EMI) was then modeled and measured to prove the proposed converter have lower EMI than the electromagnetic converter.

After proposing the full design procedure of the piezoelectric transformers based converter. The best circuit topology for the piezoelectric layers fed rectifier is the next topic of interest. The concepts of the work cycle or said the energy cycle [15] are adopted to observe the energy flow of the piezoelectric transformers since the rectifier is not easily to analyze due to the non-linearity. Guyomar and Magnet, et al. first used an active switch to increase the power density of the piezoelectric transformers was first developed by [16] However, it is not the best topology. The active rectifier called “velocity controlled piezoelectric layer fed rectifier” (VPR) is thus proposed in this dissertation based on the best shape of the work cycle. This technique is then applied to the damping, called “velocity controlled piezoelectric switching damping” (VSPD), which will be proved owning the good damping performance in this dissertation.

1.2 Major Results

This dissertation includes seven chapters. A major results of each chapter is offered as follows:

Chapter 1 makes the introduction of this dissertation.

Chapter 2 presents the theory of the piezoelectric structure, and derives the general

equivalent circuit of piezoelectric structure.

Chapter 3 presents the model and the physical limitation of piezoelectric transformers.

The input section and output section of the piezoelectric transformers are analyzed. For the output section, the characteristics of the piezoelectric transformer with the resistive load are detail. For the input section, the zero voltage switching (ZVS) mode input driving circuit of piezoelectric transformer is presented.

Chapter 4 develops a complete design rule for the piezoelectric transformers based

CCFL inverter with constant load current. The CCFL load characteristics are presented first to understand the practical requirements. The vibration velocity, load power, power tendency and ZVS conditions are considered to develop the full design procedure. The Rosen-type piezoelectric transformer designed by the proposed procedure was applied to a commercial 32 inches LCD television. The experiment result shows the efficiency of the total CCFL converter can achieve 90% and the temperature rise can be within 10°C.

Chapter 5 develops a complete design rule for the piezoelectric transformers DC/DC

converter with constant load voltage. The models of two PT fed rectifier, half-wave rectifier and the full-wave rectifier are developed first. The full-wave rectifier is then selected due to the higher power density. The vibration velocity, dimensional constraints, energy balance, quality factor correction and ZVS conditions are all considered to

develop the complete design procedure. The 10Watt/15V DC/DC converter was designed based on the proposed procedure. The proposed converter can keep at least 82% efficiency and within 10°C temperature rise with 1-10 Watt load variations. The model of the conducted EMI is then developed by the converter.

Chapter 6 develops the optimal rectifier topology with the piezoelectric source. The work cycle is used to compare the different interface circuit topologies of the piezoelectric layer. The proposed rectifier is called “velocity control piezoelectric layer fed rectifier” (VPR) which can make the piezoelectric layer owns the highest power density. The VPR is applied to the damping to suppress the vibration of the host structure. The results shows the displacement of the host structure at the resonance can be suppress 23dB, which is closed to the vibration without resonance.

Chapter 7 concludes the result of this dissertation, and give some suggestions for future research.

Chapter 2. Basic Theory of Piezoelectricity

Since piezoelectric materials can couple mechanical and electrical fields, the vibration and the generated electrical energy of a piezoelectric structure is a topic of interest. There are several uses of the piezoelectric layers, such as sensors, resonators, actuators, dampers, harvester, and transformers. No matter which kind of the application, the design of each piezoelectric component is based on their electro-mechanical properties. Therefore, the purpose of this paper is to develop theoretical model to connect the mechanical vibration and the electrical properties. Several typical types of vibration are analyzed theoretically first. The analytical solution can be further represented by an equivalent electrical circuit. This equivalent circuit is useful in practice since the piezoelectric layers are usually connected with other external shunt circuits. The purposes of the shunt circuit could be got the signal or power from piezoelectric layer, such as sensors, dampers and harvester. Therefore, a piezoelectric layer connected to an external shunt circuit will be also analyzed due to the general use. The analysis shows that the shunt circuit can modify the piezoelectric structure dynamics since this circuit can be viewed as a feedback controller of the piezoelectric structure. The analysis developed in this chapter describes both basic mechanical and electrical behaviors of the piezoelectric structure, which is the basis of the following chapters.

2.1 Piezoelectric Structures

The basic configuration of the piezoelectric structure is shown in Figure 2-1. The piezoelectric structure includes two electrodes. Between the two electrodes is the main body of the piezoelectric material. There are several kinds of the piezoelectric materials.

Three widely-used piezoelectric materials are arranged in Table 2-1:

Table 2-1. Three kinds of piezoelectric materials

Piezoelectric Materials	Typical Material	Advantages or Drawbacks
Single crystal	Quartz	<ul style="list-style-type: none"> <1> Higher electromechanical coupling <2> Difficult to enlarge the size <3> High manufacturing cost
Ceramics	PZT (Lead Zirconate Titanate)	<ul style="list-style-type: none"> <1> Medium electromechanical coupling <2> Easy to mass manufacture <3> Easy crack
Polymer	PVDF (Polyvinylidene fluoride)	<ul style="list-style-type: none"> <1> Lower electromechanical coupling <2> Thinnest profile (piezoelectric)

In this paper, PZT material is adopted in the power device due to the good electromechanically coupling and easier automatic manufacturing process. To have good piezoelectric effect, the main body has to pass through the poling (polarizing) treatment. The arrow in Figure 2-1 shows the poling direction. The piezoelectric structure with two electrodes and a main body is called single layer piezoelectric structure. To increase the electromechanical coupling effect, the piezoelectric structure can be made as multilayer structure by combining several single layers, such as Figure 2-2. Although the single layer structure and the multilayer are quite similar, but their

manufacturing processes are different. The detail manufacturing process is arranged in

Table 2-2.

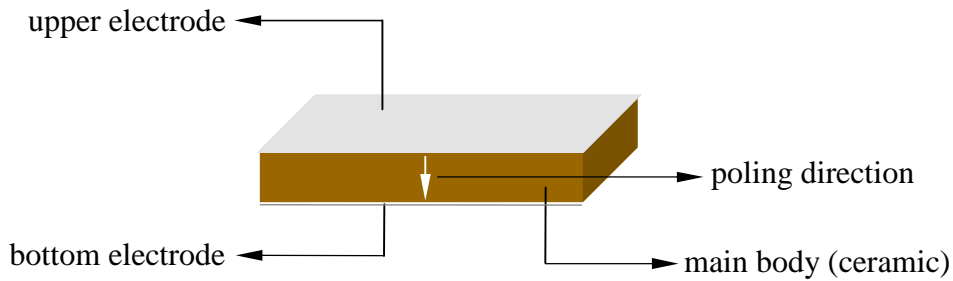


Figure 2-1. The basic configuration of the piezoelectric structure

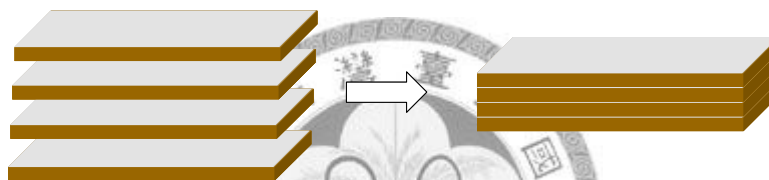


Figure 2-2. The configuration of the multilayer piezoelectric structure

Table 2-2. The manufacturing process of the piezoelectric ceramics

Single layer structure
<p><u>Preparations:</u></p> <ol style="list-style-type: none"> 1. The raw materials are mixed and milled. 2. The mixture is heated to accelerate reaction of the components 3. Add binder in order to increase the reactivity and to improve pressing properties. <p><u>Mainly sintering process:</u></p> <ol style="list-style-type: none"> 4. Shape the structure and press the powder compactly. 5. Burn out the binder. 6. Sintering process. 7. Cut, grind and polish to the desired dimension. <p><u>Post poling process:</u></p> <ol style="list-style-type: none"> 8. Apply electrodes by screen printing or sputtering. 9. Poling in the heated oil with strongly electrical fields up to several kV/mm to align the domains in the material. 10. Inspection
Multi-layer structure

Preparations:

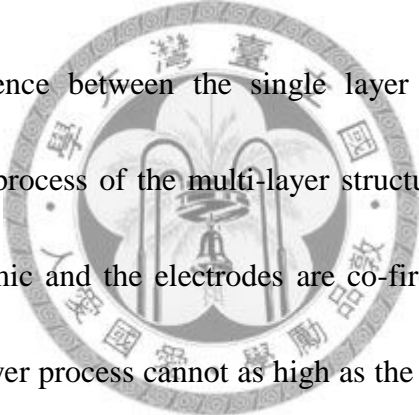
1. The raw material is mixing and milling.
2. The mixture is heated to accelerate reaction of the components.
3. Add binder in order to increase the reactivity.

Main sintering process:

4. A foil casting process which can make the thickness of the layer down to 20 μm .
5. Screen print the electrode and laminate the sheets.
6. Press to increase density and to remove air trapped between the layers.
7. The binder burnout.
8. Sintering (co-firing) process.

Post poling process:

9. Poling process.
10. Inspection



The most different difference between the single layer and the multilayer is the electrode applying. In the process of the multi-layer structure, the electrode is applied before sintering. The ceramic and the electrodes are co-fired. Therefore, the sintering temperature in the multi-layer process cannot as high as the sintering temperature in the single layer process, or the electrode may be destroyed. In addition, the electrodes of the multi-layer structure are thus made of the Ag-Pd alloy and the cost price of the multilayer structure is much higher than the single layer structure. Another manufacturing process of the multilayer structure is to glue several single layers together. The gluing process can reduce the cost price of the multilayer structure, but sacrifice the performance due to the glue material decrease the vibration quality. Adopting the single layer or multi-layer structures is based on the applications of the piezoelectric structure, which will be demonstrated in this dissertation.

2.2 The Vibration of the Piezoelectric Structures

To understand the characteristics of the piezoelectric material, the deformation behavior and the electrical behavior of the structure should be detailed. In general, to analyze an elastic body, there are three relationships of interest:

1. equations of motion,
2. the relationship between strains and displacements, and
3. constitutive law.

The equations of motion describe the relationship between the displacement (or said the acceleration) and the stress. As to the relationship between the displacements and the strains, they are related to the geometrical deformation of the structure. Constitutive law is the relationship between the stress and the strain, which is determined by the material characteristics. Therefore, constitutive law is of interest for approaching a new material.

Equation (2-1) shows constitutive equations of piezoelectric materials:

$$\begin{bmatrix} T_p \\ D_k \end{bmatrix} = \begin{bmatrix} c_{pq}^E & -e_{pi} \\ e_{kq} & \varepsilon_{ki}^S \end{bmatrix} \begin{bmatrix} S_q \\ E_i \end{bmatrix} \quad (2-1)$$

where T_p : stress

S_q : strain

D_k : electric displacement

E_i : electric field

c_{pq} : elastic stiffness matrix

ε_{ki} : dielectric or permittivity constant matrix

e_{pi} : piezoelectric stress/charge constant

where the subscript $i, k = 1 \sim 3, p, q = 1 \sim 6$ which represents the coordinates index of each parameters. This expression is based on the IEEE standard. The vibration of the piezoelectric structure is complex because the vibration is three dimensional. However, we can approximate the vibration as one dimension or two dimensions in most applications.

Table 2-3 shows several basic types of vibration for the piezoelectric structures and their corresponding dimensional conditions.

1. The first type of the vibration is called 31-type. 31-type vibration means that the electrical field (voltage) is applied along the poling direction (3-direction) to induce the vibration along the corresponding perpendicular direction (1-direction).
2. The second type of the vibration is called 33-mode. 33-type vibration means that the electrical field (voltage) is applied along the poling direction (3-direction) to induce the vibration along the corresponding parallel direction (3-direction).
3. The third type of the vibration is radial mode, which is similar to the 31-type vibration. The applied voltage is perpendicular to the direction of the vibration, but the radial mode is a two dimensional vibration based on the symmetric characteristic.
4. In addition, the piezoelectric material can also adhere to a host structure to be a

transducer. The most often used host structure is the beam structure. This configuration was called piezoelectric/beam system. In the piezoelectric/beam system, it usually operated near the resonant frequency of the host structure and the strain of the piezoelectric layer is following the strain of the beam.

Table 2-3. The self-vibration modes of the piezoelectric structures

Deformation /Vibration	Configurations		Coefficients	
	Figures	conditions	electrical	mechanical
31-mode		$T, W < L/3$	ϵ_{33}^S, e_{31}	s_{11}^E
33-mode		$L, W < T/3$	ϵ_{33}^S, e_{33}	s_{33}^D
radial mode		$D > 5T$	ϵ_{33}^S, e_{31}	$s_{33}^E(1 - \nu^2)$,

is the direction of the poling direction, and is the direction of the vibration.
 ϵ_{33}^S is the permittivity at constant strain condition, i.e. constant S (F/m)
 s_{11}^E, s_{33}^D are the compliance constants along 11/33 direction under the constant electric field E /electric displacement $D=2R$

ν is the Poisson's ratio

2.3 The Theory of Deformation/Vibration

31-mode deformation/vibration is the most often used vibration type in practice.

The relationship between the strain and the displacement along 1-direction is:

$$S_1(x,t) = \frac{\partial u_1(x,t)}{\partial x} \quad (2-2)$$

where x and t represent the spatial domain and temporal domain respectively. In the case of the 31-type deformation/vibration, the spatial domain x in equation (2-2) just represents 1-direction (or said x -direction directly). In addition, u_1 is the displacement along the 1-direction and the comma indicates the partial differentiation. The strain and the displacement are functions of both the spatial domain and the temporal domains. Based on the general constitutive equation (2-1), the relationship between the strain and the displacement in equation (2-2) and the definition of the 31-type vibration, the constitutive equation of 31-type vibration can be written as:

$$\begin{bmatrix} T_1 \\ D_3 \end{bmatrix} = \begin{bmatrix} c_{11}^E & -e_{31} \\ e_{31} & \epsilon_{33}^S \end{bmatrix} \begin{bmatrix} \frac{\partial u_1}{\partial x} \\ E_3 \end{bmatrix} \quad (2-3)$$

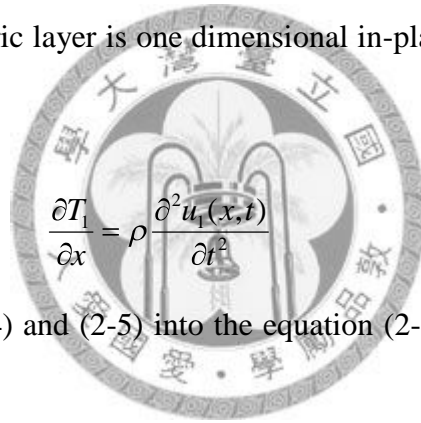
According to the configuration of the piezoelectric layer, the electric field can be expressed as:

$$E_3(x,t) = \frac{v_p(t)}{T} R(x) \quad (2-4)$$

where T is the thickness of the piezoelectric layer, v_p is the voltage on the piezoelectric

layer and R is the function of the electrode shape. In most applications, the electrode is full covered on the piezoelectric structure, *i.e.* $R(x) = H(x-L) - H(x)$, where $H(x)$ represents Heaviside function. On the other hand, the voltage on the piezoelectric layer can be DC or AC voltage. The DC voltage makes the piezoelectric layer have static deformation and AC voltage makes the piezoelectric layer vibrate.

In the following, the case of vibration is only of interest since the piezoelectric layer is usually operating near its resonant frequency in the use of power devices. The 31-type vibration of the piezoelectric layer is one dimensional in-plane motion. The equation of motion can be written as:



$$\frac{\partial T_1}{\partial x} = \rho \frac{\partial^2 u_1(x,t)}{\partial t^2} \quad (2-5)$$

Substituting equations (2-4) and (2-5) into the equation (2-3), the constitutive equation can be re-written as:

$$c_{11}^E \frac{\partial^2 u_1}{\partial x^2} - \rho \frac{\partial^2 u_1}{\partial t^2} = e_{31} \frac{\partial R}{\partial x} v_p \quad (2-6)$$

$$q = e_{31} \int_0^L \frac{\partial u}{\partial x} W dx + C_p v_p \quad (2-7)$$

where $C_p = \varepsilon_{33}^S \int_0^L R \frac{W}{T} dx$ is the piezoelectric capacitor and $q = \int_0^L D_3 W dx$ is the charge generated from the piezoelectric layer. Equations (2-6) and (2-7) mainly describe the structure dynamics and electric characteristic respectively. It should be noted that equation (2-6) is a partial differential equation. The solution of the partial differential equation is based on the boundary conditions and the initial conditions. The typical

boundary conditions are free at both ends, *i.e.*

$$T_1(0,t) = T_1(L,t) = 0 \quad (2-8)$$

Based on the partial equations (2-6), boundary conditions (2-8) and initial conditions, the solution set of the partial differential equation can be solved. There are several eigen-solutions in a partial differential equation, which represents the vibration modes of the structure. However, when the piezoelectric layers are used to transfer energy, the piezoelectric structures are usually operating near the resonant frequency due to the need of efficiency. Accordingly, the specific resonant modes of the piezoelectric structure are of interest. Equations (2-6) and (2-7) are the general equations to describe all the vibration modes of the piezoelectric structure, which can describe the all possible 31-type vibration modes theoretically. To simplify the equations (2-6) and (2-7) to the specific resonant mode, the case of the free vibration is discussed first. In this case, there is no external force or applied voltage on the piezoelectric layer. In addition, the boundary is set traction free, *i.e.* there is no stress on the boundary. Therefore,

$$\frac{\partial^2 u_1}{\partial x^2} - \frac{\rho}{c_{11}^E} \frac{\partial^2 u_1}{\partial t^2} = 0 \quad (2-9)$$

$$\frac{\partial u_1(0,t)}{\partial x} = \frac{\partial u_1(L,t)}{\partial x} = 0 \quad (2-10)$$

Assume the vibration of the piezoelectric structure is harmonic, let

$$u_1(x,t) = \sum_{j=1}^{\infty} U_j(x) e^{j\omega_j t} \quad (2-11)$$

where U_j represents the j -th mode shape of the displacement and ω_j is the j -th natural

frequency of the piezoelectric structure. Substituting equation (2-11) into equation (2-9), the partial differential equation can be reduced to the ordinary differential equation, such as:

$$\frac{d^2U_j(x)}{dx^2} + k_j^2U_j(x) = 0 \quad (2-12)$$

$$\frac{dU_j(0)}{dx} = \frac{dU_j(L)}{dx} = 0 \quad (2-13)$$

The mode shape of the vibration can be obtained by solving equations (2-12) and (2-13):

$$U_j(x) = A\cos(k_jx) \quad (2-14)$$

where k_j is wave number and has the relationship with the natural frequency, *i.e.* $k_j^2 = \rho\omega_j^2 / c_{11}^E = 2\pi / L$ and A is the weighting function of the mode shape. It should be noted that this physical mode shape has the orthogonal relationship, *i.e.*

$$\int_0^L U_i U_j dx = \delta_{ij} \quad (2-15)$$

Consider the case of the forcing vibration, let:

$$u(x, t) = \sum_{j=1}^{\infty} U_j(x)\eta_j(t) \quad (2-16)$$

where $\eta_j(t)$ is the modal coordinate. Substituting equation (2-16) into equations (2-6), (2-7) and making the integration in the both sides, we can obtain that:

$$\int_0^L \sum_{i=1}^{\infty} [U_i(x)U_j(x) \frac{d^2\eta_i(t)}{dt^2} - \frac{c_{11}^E}{\rho} \frac{d^2U_i(x)}{dx^2} U_j(x)\eta_i(t)] dx = -\frac{e_{31}v_p}{\rho} \int_0^L \frac{dR(x)}{dx} U_j(x) dx \quad (2-17)$$

$$q = e_{31}W[\int_0^L \frac{dU_j(x)}{dx} R(x) dx]\eta(t) + C_p v_p \quad (2-18)$$

Apply the orthogonal relationship shown in equation (2-15), the actuator equation (2-17)

and the sensor equation (2-18) can be arranged as the ordinary differential equations:

$$M_j \frac{d^2 \eta_j(t)}{dt^2} + K_j \eta_j(t) = -n_j^T v_p \quad (2-19)$$

$$q = n_j \eta_j(t) + C_p v_p \quad (2-20)$$

where M_j , K_j and n_j is the j -th modal mass, the j -th modal stiffness and the j -th modal coupling factor of the piezoelectric structure. Specifically,

$$M_j = \rho WT \int_0^L U_i(x) U_j(x) dx \quad (2-21)$$

$$K_j = M_j \omega_j^2 \quad (2-22)$$

$$n_j = e_{31} W \int_0^L \frac{dU_j(x)}{dx} R(x) dx \quad (2-23)$$

Equations (2-19) and (2-20) are the governing equation of the piezoelectric layer.

Different from equations (2-6) and (2-7), equations (2-19) and (2-20) describe the behavior of the piezoelectric layer operating near the resonant frequencies. More specifically, equations (2-6) and (2-7) are the governing equations of the distributed system, and equations (2-19) and (2-20) are the governing equations of the lumped system.

On the other hand, the governing equations above do not introduce losses in the piezoelectric layer. In practice, there are three kinds of losses in the piezoelectric structures, which are the mechanical loss, the dielectric loss and the piezoelectric loss.

The mechanical losses are caused by the friction of the vibration, so the larger vibration velocity leads to the larger mechanical losses. It is the damping effect of the

piezoelectric layer. Moreover, the dielectric losses are mainly related to the temperature.

The piezoelectric losses are caused by the energy transfer between the electrical energy and the mechanical energy. The piezoelectric losses are relatively very small, so they can be neglected in practice. To introduce the mechanical losses and the dielectric losses, the mechanical damping D and the electrical series resistor (ESR) R_p are introduced in the governing equations to correct the model, such as:

$$M\ddot{\eta} + D\dot{\eta} + K\eta = -n^T v_p \quad (2-24)$$

$$\dot{q}_p = n_j \dot{\eta}_j + C_p \dot{v}_p + \frac{v_p}{R_p} \quad (2-25)$$

The subscript j is neglected here for simplicity. Actually, no matter which type of the vibration is adopted, the governing equations of lumped system are still guaranteed, but the modal parameters are different in different type of vibration.

2.4 The Equivalent Circuit of the Piezoelectric Structure

In many cases, we prefer using an equivalent circuit to describe the piezoelectric layers since piezoelectric layers are usually connected to a circuit or even used as an electric component in a power device. The equivalent circuit of the piezoelectric layer can help electrical engineers to analyze the piezoelectric component in the circuit intuitively.

According to the governing equations (2-24) and (2-25), the equivalent circuit of the

piezoelectric layer can be represented in Figure 2-3. The series inductor-capacitor-resistor resonant branch is used to emulate the mechanical resonance of the vibration, where $L_m=M$, $C_m=1/K$, $R_m=D$ are called mechanical inductor, mechanical capacitor and the mechanical resistor respectively. Other resonant branches in the equivalent circuit means the parasitic resonant modes since there are infinite vibration mode in the piezoelectric structure. The mechanical current i_m can be analoged to the mechanical velocity, and the mechanical voltage v_m can be analog to the force. In addition, the ideal transformer represents the energy transformation between the mechanical energy and the electrical energy. This equivalent circuit describes the electro-mechanical behavior of the piezoelectric structure at the resonance, no matter which type of vibration.

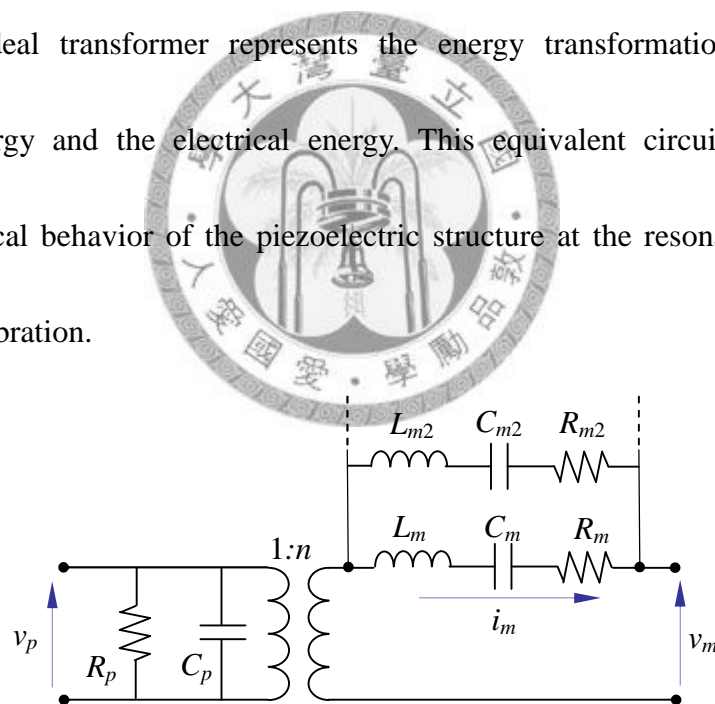


Figure 2-3. The equivalent circuit of the piezoelectric structure

However, this equivalent circuit can be simplified. Firstly, the parasitic resonant modes can be neglected since the piezoelectric structure operates at a specific frequency in most cases. In addition, if the operating frequency is set near the resonant frequency and temperature rise of the piezoelectric layer is small, the effect of the dielectric losses

is small. In such conditions, resistor R_p can be neglected. Therefore, the equivalent circuit of Figure 2-3 can be simplified to Figure 2-4. It should be noted that the relationship between the dimensional parameters and the equivalent circuit components are different in the different vibration modes. For example, the first vibration mode and the second vibration mode have different relationship between the electric circuit components and the dimensional parameters. Table 2-4 arranges the equivalent circuit components of the first mode since the first mode is the most often used vibration mode.

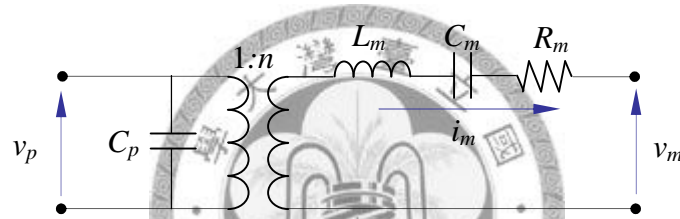


Figure 2-4. The single mode equivalent circuit of piezoelectric layer

Table 2-4. The first mode equivalent circuit of different vibration type piezoelectric layer

types	ω_o	L_m	C_m	R_m	C_p	n
31	$\frac{4\pi N_l}{L}$	$\frac{\rho_m LWT}{8}$	$\frac{1}{L_m \omega_o^2}$	$\frac{1}{Q_m} \sqrt{\frac{L_m}{C_m}}$	$\frac{\epsilon_{33}^S WL}{T}$	$\frac{Wd_{31}}{s_{11}^E}$
33	$\frac{4\pi N_l}{L}$	$\frac{\rho_m LWT}{8}$	$\frac{1}{L_m \omega_o^2}$	$\frac{1}{Q_m} \sqrt{\frac{L_m}{C_m}}$	$\frac{WL \epsilon_{33}^S}{2T}$	$\frac{Wd_{31}}{s_{11}^E}$
radial	$\frac{\pi N_p}{T}$	$\frac{\rho_m \pi R^2 T}{1.4}$	$\frac{1}{L_m \omega_o^2}$	$\frac{1}{Q_m} \sqrt{\frac{L_m}{C_m}}$	$\frac{\pi R^2 \epsilon_{33}^S}{T}$	$\frac{2\pi R d_{31}}{s_{11}^E (1-\nu^2)}$

The equivalent circuit of the piezoelectric layer can be further simplified. When the piezoelectric structure operates near a specific resonant frequency in steady state, the mechanical current is sinusoidal. At this time, mechanical current can be viewed as a

sinusoidal current source or sink at steady state, which is shown in Figure 2-5.

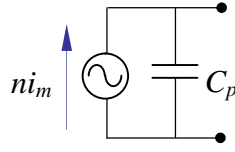


Figure 2-5. The equivalent circuit of the piezoelectric layer with mechanical current source

2.5 Piezoelectric Materials with External Shunt Circuits

Figure 2-4 shows a piezoelectric structure connected to an external electrical shunt circuit. The connected shunt circuit changes the electrical boundary conditions of the piezoelectric structure. Therefore, the connected shunt circuit can modify the mechanical characteristics of the piezoelectric structure, since the piezoelectric material couples the mechanical field and the electrical field. According to Figure 2-4, equation (2-20) and Kirchhoff's Law, the piezoelectric voltage, v_p , and the current flow out of piezoelectric layer, $-i_p$, the piezoelectric voltage can be expressed in the steady state, such as [17]:

$$v_p = -Z_{SH} i_p = -sZ_{SH} [n\eta + C_p v_p] \quad (2-26)$$

where s is the Laplace parameter. Arranging equation (2-26) leads to:

$$v_p(s) = \frac{-sZ_{SH}n}{1 + sC_p Z_{SH}} \eta(s) \quad (2-27)$$

Equation (2-27) describes the transfer function between the displacement and the piezoelectric voltage. Substituting equation (2-27) into equation (2-19), and add the external forcing term f_{ext} , we can obtain that:

$$\left[Ms^2 + \left(D + \frac{n^2 Z_{SH}}{1 + sC_p Z_{SH}} \right) s + K \right] \eta(s) = f_{ext} \quad (2-28)$$

According to equation (2-28), it can be known that the impedance of the shunt circuit can modify the dynamic characteristics of the structure. More specifically, the shunt circuit can change easily the modal damping and the modal stiffness in equation (2-28). This is the reason why the piezoelectric layer with a shunt circuit can be applied as a damper. For the damper, it is expected that the vibration energy can be dissipated in the shunt circuit. The performance of the damping is based on the dissipated energy. However, in application as sensor, it cannot influence the structure dynamics. Specifically, a good sensor needs two sufficient conditions:

1. A good sensor must not influence the vibration of the structure. However, the shunt circuit may change the mechanical behavior of the structure.
2. The piezoelectric layer may only generate small signal. The sensor interface circuit should have pre-amplified function.

Therefore, a piezoelectric sensor needs an interface circuit. The sensor interface circuit should have the zero input impedance or infinite impedance characteristics to avoid influencing the structure dynamics.

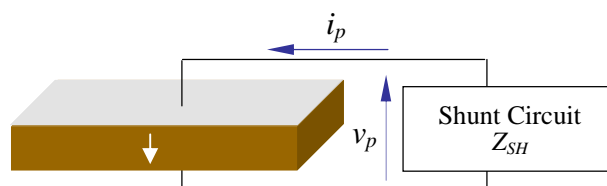


Figure 2-6. Piezoelectric layer with a shunt circuit

To understand the contribution of the shunt circuit, equation (2-28) is arranged as:

$$\left[\frac{M}{K} s^2 + \frac{D}{K} s + k^2 \frac{s C_p Z_{SH}}{1 + s C_p Z_{SH}} + 1 \right] \eta = \frac{f_{ext}}{K} = \eta^{ST} \quad (2-29)$$

where k is electromechanical coupling factor, defined as:

$$k^2 = \frac{n^2}{C_p K} \quad (2-30)$$

Equation (2-29) can be further derived to the transfer function:

$$\frac{\eta}{\eta^{ST}} = \frac{1}{\frac{M}{K} s^2 + \frac{D}{K} s + 1 + k^2 \frac{s C_p Z_{SH}}{1 + s C_p Z_{SH}}} \quad (2-31)$$

Equation (2-31) can be plotted as a block diagram in Figure 2-7. Obviously, the piezoelectric layer with a shunt circuit can be viewed as a feedback controller for the structure. This virtual feedback controller is related to the three parameters, which are electromechanical coupling factor k , piezoelectric inherent capacitor C_p and the shunt impedance Z_{SH} .

To understand the contribution of the internally virtual controller, Figure 2-7 can be further decomposed to Figure 2-8. In Figure 2-8, the feedback loop pass through the electromechanical coupling factor k first. The electromechanical coupling factor k give a direct control gain of the feedback controller, which implies that the larger k value leads to better performance of the shunt circuit. In addition, the piezoelectric inherent

capacitor C_p and the shunt impedance Z_{SH} have another feedback loop. It represents the charge/discharge behavior of the piezoelectric capacitor, which implies that the charging period of the piezoelectric capacitor also influences the structure dynamics. Since the shunt circuit would influence the structure dynamics, the connected circuit has to be analyzed first before to design the piezoelectric layer, especially in the case that the mechanical/electrical is highly coupling (high k value).

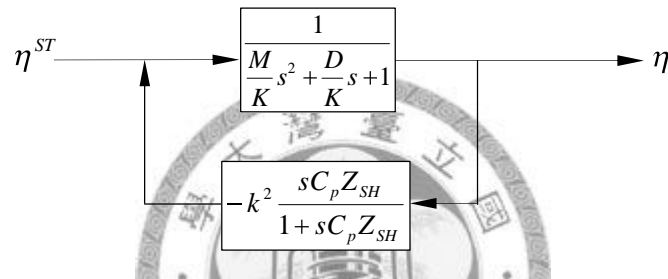


Figure 2-7. The internal feedback system of the shunt circuit

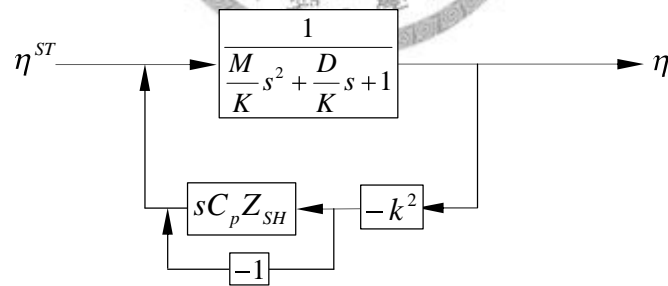


Figure 2-8. The internal feedback system of the shunt circuit with capacitor charging

2.6 Summary

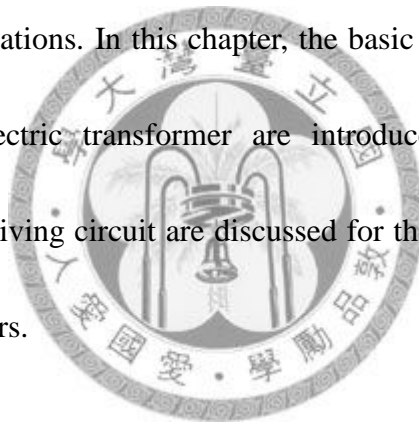
In this chapter, the basic vibration types of the piezoelectric layer were introduced. The most-often used 31-type vibration was analyzed theoretically. Although the piezoelectric structure has the infinite vibration modes, but only the specific resonant

mode will be adopted or considered in general use. All types of the vibration can be concluded to the equivalent circuit to aid the design in the following chapter. Therefore, the equivalent circuit was derived based on the electro-mechanical coupled equations. A piezoelectric layer with a shunt circuit, and the virtual feedback controller was introduced to express the contribution of the shunt circuit. The equivalent circuit and the electro-mechanical coupled equations are two useful concepts for the designer of the piezoelectric device. These two concepts will be repeated to use in our design in the following chapters.



Chapter 3. Piezoelectric Transformers

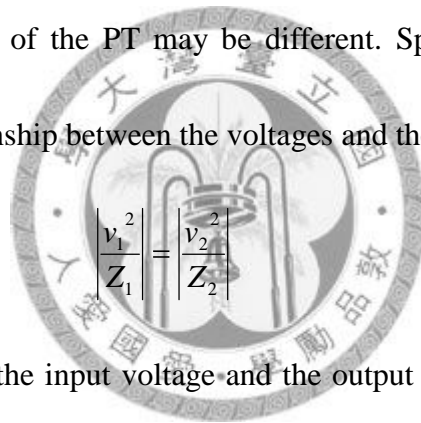
Piezoelectric transformers are devices that transfer electrical energy from one circuit to another one through the mechanical vibration of its structure. The voltage amplitude is varied throughout the energy transformations. Compared with the typical electromagnetic transformer, there are several advantages of the piezoelectric transformers, such as no EMI radiation, thin profile, high power density and easier manufacturing process. Therefore, it is possible to replace the electromagnetic transformer in some applications. In this chapter, the basic configurations and physical limitation of the piezoelectric transformer are introduced first. Then, the output characteristics and input driving circuit are discussed for the design of the piezoelectric transformer based converters.



3.1 The configurations of the piezoelectric transformers

Piezoelectric transformers (PT) are devices that transfer electrical energy from one circuit to another through the vibration its structure. Generally speaking, a PT can at least be divided into two sections which are the input section and the output section or said the primary side and the secondary side. Figure 3-1 shows the input section and the output section of the PT. A voltage source is connected to the input section to excite the mechanical vibration of the whole PT structure. The output section of the PT receives

the mechanical energy of the vibration and transforms into electric energy again. An output interfacing circuit is then connected to the output section of the PT to collect the electrical energy and to deliver it to the load. In other words, the input section of the PT works like a piezoelectric actuator which transforms the electrical energy to the mechanical energy. The output section of the PT works like a piezoelectric harvester which converts the electrical energy transformed from the mechanical one. In an ideal PT, there is no energy loss. The voltages vary through the PT since the input impedance and the output impedance of the PT may be different. Specifically, according to the energy balance, the relationship between the voltages and the impedances of the PT is:



$$\left| \frac{v_1}{Z_1} \right|^2 = \left| \frac{v_2}{Z_2} \right|^2 \quad (3-1)$$

where v_1 and v_2 represent the input voltage and the output voltage respectively, and Z_1 and Z_2 represent the input impedance and the output impedance of the PT respectively. The values of v_1 and v_2 are considered as sinusoidal at specific frequency. The basic types of vibration of the piezoelectric structure are listed in Table 2-1. They can be all either used for the input section or for the output section. By combining and arranging these different vibration modes, several configurations of the PT are discussed hereunder. Table 3-1 shows common used PT configurations, including the Rosen-type PT, the uni-poled longitudinal PT, the uni-poled disk-type PT and the stacked disk-type PT.

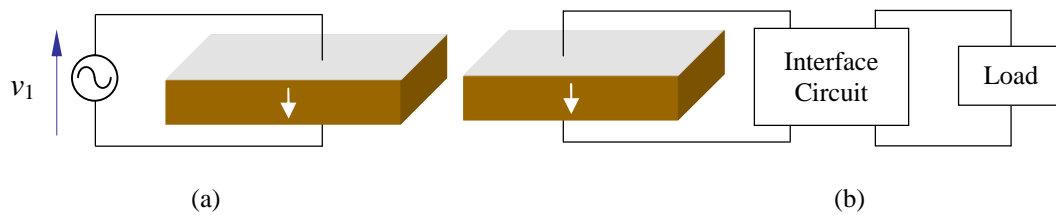
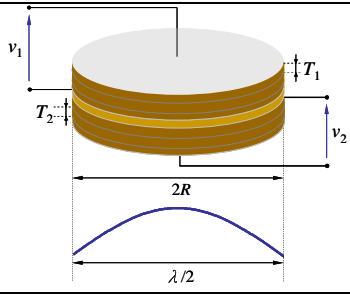


Figure 3-1. (a) input section of the PT (piezoelectric actuator) (b) output section of the PT (piezoelectric harvester)

Table 3-1. Different types of PTs

Types	The configuration of the PT	Input/Output	Typical modes
1. Rosen-type [1]		31/33	λ mode
2. Uni-poled Longitudinal-type [3]		31/31	λ mode
3. Concentric Disk-type [18]		radial/radial	$\lambda/2$ mode
4. Stacked		radial/radial	$\lambda/2$ mode

<p>Disk-type</p> <p>[19, 20]</p>			
----------------------------------	---	--	--

In this dissertation, a simple equivalent circuit is used to analyze the PT working. This equivalent circuit is well matched to analyze the working of PT based power converter.

Figure 3-2 shows the equivalent circuit of the PT by connecting two piezoelectric layers,

i.e. its input section and its output section. The equivalent circuit can be mainly

identified into three parts: the input static capacitor C_1 , the mechanical resonant branch

(series inductor-capacitor-resistor resonant branch), and the output capacitor C_2 . Two

ideal transformers link these three parts, which represents the electrical-to-mechanical

energy transformation. The mechanical branch is used to represent the mechanical

resonance. The mechanical current i_m is the current through the mechanical resonant

branch; it represents the mechanical velocity of the PT vibration. It should be noted that

this equivalent circuit is only valid when the PT is operating near its specific resonance

frequency. No matter which configuration of the PT is adopted, the equivalent circuit is

conserved. The various kinds of PT have different relationship between their dimension

factors and their electric equivalent components. These relationships are listed in Table

3-2 [3, 12, 19, 20, 21, 22].

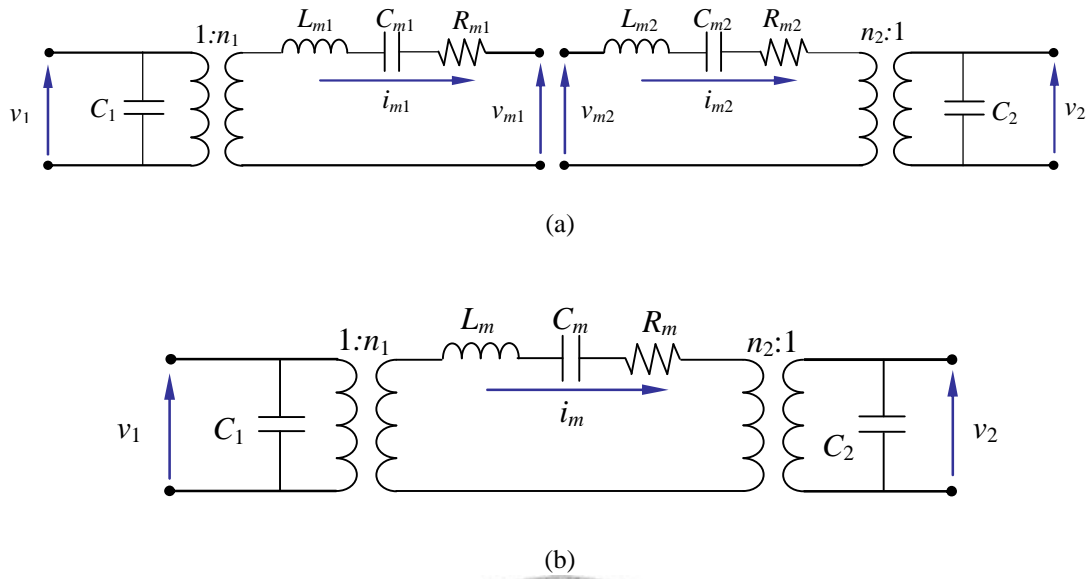


Figure 3-2. (a) Combining two piezoelectric layers (b) the single mode equivalent circuit of the PT with

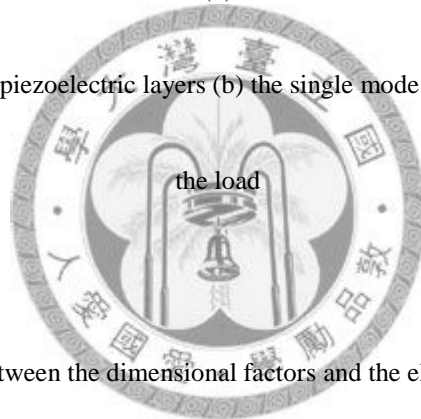


Table 3-2. The relationship between the dimensional factors and the electrical equivalent components

	ω_o	L_m	C_1	C_2	n_1	n_2
1	$\frac{4\pi N_l}{L}$	$\frac{\rho_m LWT}{8}$	$\frac{2WT\varepsilon_{33}^S}{L}$	$\frac{2WT\varepsilon_{33}^S}{L}$	$\frac{Wd_{31}}{s_{11}^E}$	$\frac{2WTd_{33}}{Ls_{33}^E}$
2	$\frac{4\pi N_l}{L}$	$\frac{\rho_m LWT}{8}$	$\frac{WL\varepsilon_{33}^S}{2T}$	$\frac{WL\varepsilon_{33}^S}{2T}$	$\frac{Wd_{31}}{s_{11}^E}$	$\frac{Wd_{31}}{s_{11}^E}$
3	$\frac{\pi N_p}{T}$	$\frac{\rho_m \pi R_3^2 T}{1.4}$	$\frac{\pi R_1^2 \varepsilon_{33}^S}{T}$	$\frac{\pi(R_3^2 - R_2^2) \varepsilon_{33}^S}{T}$	$\frac{2\pi R_1 d_{31}}{s_{11}^E(1-\nu^2)}$	$\frac{2\pi R_1 d_{31} \alpha}{s_{11}^E(1-\nu^2)}$
4	$\frac{\pi N_p}{T}$	$\frac{\rho_m \pi R_3^2 \beta}{2}$	$\frac{m_1 \pi R^2 \varepsilon_{33}^S}{t_1}$	$\frac{m_2 \pi R^2 \varepsilon_{33}^S}{t_2}$	$\frac{2\sqrt{2}\pi R d_{31} m_1}{s_{11}^E(1-\nu^2)}$	$\frac{2\sqrt{2}\pi R d_{31} m_2}{s_{11}^E(1-\nu^2)}$
$C_m = \frac{1}{L_m \omega_o^2} \quad R_m = \frac{1}{Q_m} \sqrt{\frac{L_m}{C_m}}$ <p>ω_o is the natural frequency of the PT (rad/s)</p> <p>N_l, N_p are the frequency constants in the longitudinal vibration and the plane vibration respectively(kHz• mm)</p> <p>ρ_m is the density (kg/m³)</p>						

ν is the Poisson's ratio

Q_m is the mechanical quality

ϵ_{33}^D is the permittivity at constant strain condition, i.e. constant S (F/m)

d_{31}, d_{33} are the piezoelectric constants (m/V)

e_{33} (C/ m²)

s_{11}^E, s_{33}^E are the compliance constants under the constant electric field

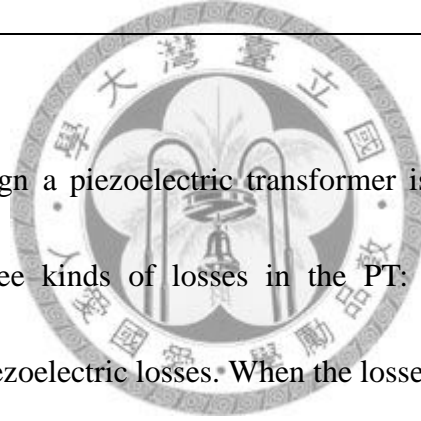
L, W and T are the dimensional factors of the rectangular PT, which represent length, width and thickness respectively

R, R_1, R_2 and R_3 are the dimensional factors of the circular PT. The definitions are shown in the Figure 1

$$\alpha = 1 - \frac{R_2 J_1(k_1 R_2)}{R_3 J_1(k_1 R_3)} \quad \text{where } J_1 \text{ is the Bessel function}$$

m_1 and m_2 are the numbers of layers of the input section and the output section respectively

$$\beta = m_1 t_1 + m_2 t_2$$



The first step to design a piezoelectric transformer is to understand its working limitations. There are three kinds of losses in the PT: the mechanical losses, the dielectric losses and the piezoelectric losses. When the losses in the PT are too large, the PT generates heat gradually. If temperature is too high, the PT can even crack. The major losses in the PT are the mechanical losses which are due to the friction of the crystalline structure when it vibrates. The larger vibration velocity (i.e. mechanical current) leads to the larger mechanical losses. In the equivalent circuit, the mechanical losses P_{loss} are equal to $i_m^2 R_m$. This fact shows that the mechanical current is one of the key factors in the PT design. When the mechanical current rises, the mechanical losses and the temperature increase as well. Furthermore, the higher temperature of the PT leads to increase the mechanical resistance. Therefore, we can have a brief summary:

the mechanical current causes the mechanical resistance to increase. This is a significant result since the mechanical losses are related to both mechanical current and to the mechanical resistance. To clearly describe the relationships between the main physical parameters, the tendency between them has been plotted in Figure 3-3. However, it should be noted that there are two different results when the mechanical resistance increases.

Firstly, when the mechanical losses increase, temperature and mechanical resistance are both increasing. Specifically, this is a positive feedback loop if i_m magnitude remains constant. If the PT works in this tendency, the heat generation of the PT would become unstable until crack.

On the other hand, when the mechanical resistance increases, the mechanical current and the mechanical losses also decrease since the input voltage and the output voltage of the PT are fixed in most applications. Therefore, this is a negative feedback loop, which can make the heat generation of the PT kept stable. Figure 3-3 demonstrates the complete internal loop of the PT mentioned above. In practice, the magnitude of the mechanical current and the law of variation of R_m with temperature (i.e. a physical parameter of the material) determine if the PT is stable or not. In other words, for a given material, it a maximum mechanical current value exists. This value is usually within 0.3~1A (i.e. 0.3m/s~1m/s). The mechanical current can be calculated by applying

the equivalent circuit model to the output short-circuit current, such as shown in Figure

3-4.

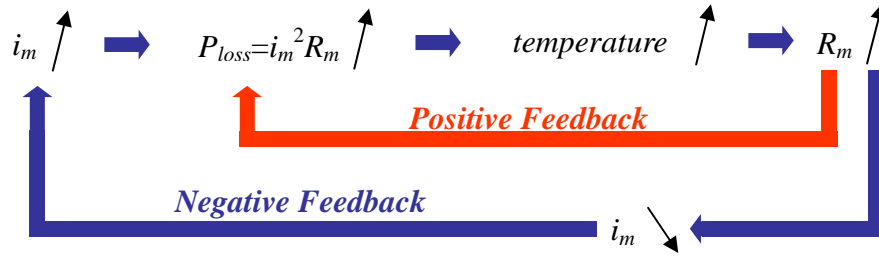


Figure 3-3. The internal loop of the PT

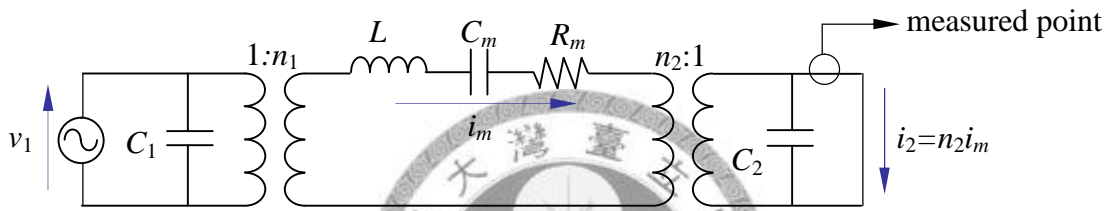


Figure 3-4. The measurement of the mechanical current

3.2 Characteristics of the PT connected with a linear load

The PT equivalent circuit connected to a load is shown in Figure 3-5, which is adopted to analyze the characteristics of the PT. The PT equivalent circuit can be divided into three parts as mentioned in the last section. Here, we use Z_{ME} to represent the impedance of the mechanical branch, Z_{HPF} to represent the high-pass filter formed by the output static capacitor C_2 and resistive load, R_L . The voltage gain of the piezoelectric transformer can then be obtained as:

$$\frac{v_2}{v_1} = \frac{n_1}{n_2} \frac{Z_{HPF}}{Z_{ME} + Z_{HPF}} \quad (3-2)$$

where

$$Z_{ME} = sL_m + \frac{1}{sC_m} + R_m \quad (3-3)$$

$$n_2^2 Z_{HPF} = \frac{R_L}{1 + sC_2 R_L} \quad (3-4)$$

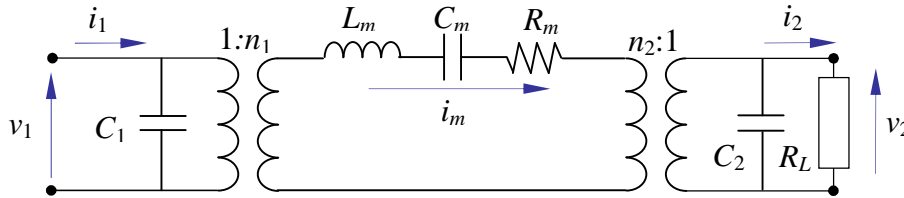


Figure 3-5. The single mode equivalent circuit of the PT with the load

Once the input voltage, the model of the piezoelectric transformer and the load impedance are decided, the output voltage can then be determined by (3-2). With Ohm's law, the output current i_2 and the load power P_L can be related as:

$$i_{out} = \frac{v_2}{R_L}, \quad P_L = \frac{1}{T} \int_0^T v_L i_2 dt \quad (3-5)$$

One of the PT studied is chosen as an example in this chapter; the values of its equivalent circuit are shown in

Table 3-3. According to equation (3-2~5), the gain and the load power characteristics of this PT are plotted in Figure 3-6 with different load values. According to Figure 3-6, we can observe that the resonant frequencies of the piezoelectric transformer are depending significantly on load values.

Table 3-3. The tested PT model

C_1	n_1	L_m	C_m	R_m	n_2	C_2
4nF	1	0.03H	100pF	10Ω	4	30nF

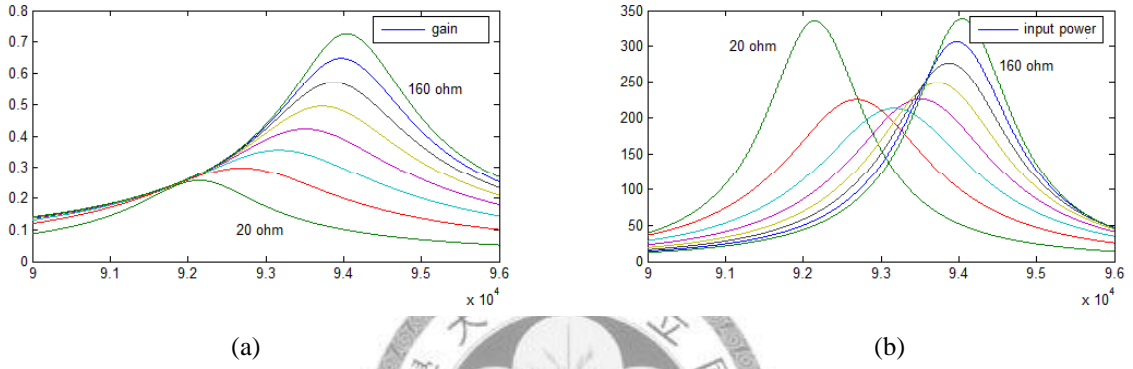


Figure 3-6. (a) The voltage gain and (b) the power characteristics of the PT with resistive load

In fact, the load-dependent resonant frequencies are due to the contribution of the PT output capacitor C_2 . To describe this phenomenon in more detail, the relationships $Z_L = R_L$ and $s = j\omega$ are substituted into equation (3-2). The PT output capacitor and the resistive load are equivalent to a series equivalent capacitance C_{eq} and a series equivalent resistor R_{eq} in Figure 3-7.

$$n_2^2 Z_{HPF} = R_{eq} + \frac{1}{j\omega C_{eq}} \quad (3-6)$$

where

$$R_{eq} = \frac{R_L}{1 + (\omega C_2 R_L)^2} \quad (3-7)$$

$$C_{eq} = C_2 \frac{1 + (\omega C_2 R_L)^2}{(\omega C_2 R_L)^2} \quad (3-8)$$

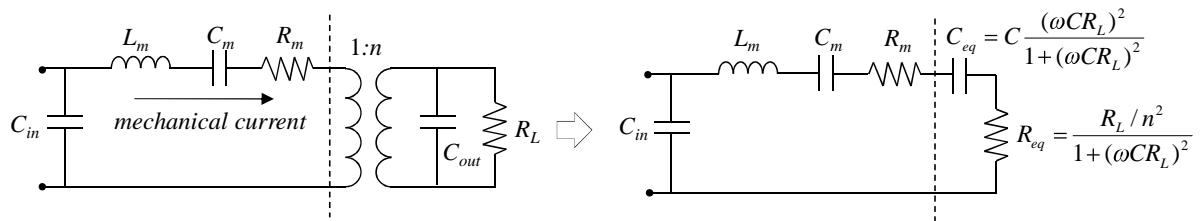


Figure 3-7. The equivalent circuit of PT with a resistive load

According to Figure 3-7, the resonance frequency of the PT is:

$$\omega_0 = \frac{1}{\sqrt{L_m \frac{C_m C_{eq}}{C_m + C_{eq}}}} \quad (3-9)$$

Obviously, the resonance frequency is changed by the equivalent series capacitor C_{eq} . Moreover, the equivalent capacitor C_{eq} varies with the load value, *i.e.* $dC_{eq}/dR_L \neq 0$. This fact leads to the conclusion that a load variation will change the resonance frequency of the PT significantly. This characteristic is interesting for some applications such as the lamp ballast. In most cases, however, the maximum power point with fixed frequency is better.

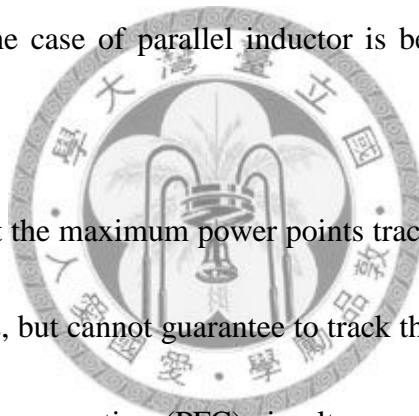
One possible way to solve the problem of maximum power point shifting is to parallel or series an inductor to compensate the contribution of the PT output capacitor. Similarly to the resistive load case, Z_{HPF} can be equivalent to a series equivalent reactive component and a series equivalent resistor. If the equivalent reactive component is independent of the load, the resonant frequencies and the maximum power points would not change with the load significantly but remain fixed at a specific value.

The results are summarized in Table 3-4. The equivalent reactive component in the cases of the parallel inductor and series inductor is independent of the load value, i.e. $dL_{eq}/dR \neq 0$ if, and only if the added inductor matches the PT output capacitor at the operating frequency. The frequency responses of cases 2 & 3 with the load variation are shown in Figure 3-8 and Figure 3-9. Obviously, the maximum power point is fixed at the specific frequency in both of these two cases. The added inductors can indeed fix the problem of the maximum power point shifting.

Another issue of the PT is the power factor problem. The power factor is caused by the phase shift between the voltage and the current. The power factor is defined as the cosine value of the phase difference. For zero phase difference between the voltage and the current, the power factor is defined to be 1, which is the best situation we want to achieve. Specifically, if voltage and the current are not in phase, power would not flow in single direction. The power will not only flow from the source to the load but also flow back from the load to the source. Three cases in last sections are also discussed here.

There are two cases able to track the maximum power points but it does not guarantee good power factor at the same time. If we would like to obtain a good power factor with no phase difference between the voltage and the current, the source should see a pure resistive load. To have a purely resistive load, the equivalent reactive

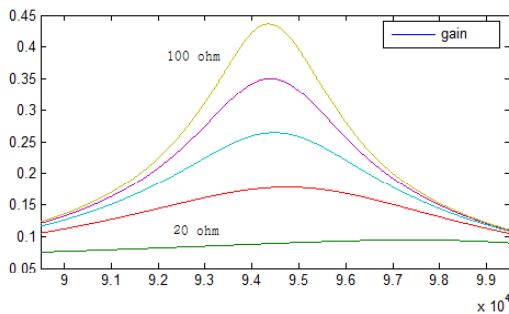
component in table 3-4 should be zero. Examining the case of paralleling the inductor, the equivalent inductor can be zero, $L_{eq}=0$, when the added inductance matches the PT output capacitance with the operating frequency, $L_{eq}=1/\omega C_{eq}$. However, the case of serial inductor is different. The equivalent inductance can be a constant when the added inductance matches the PT output capacitance with the operating frequency, $L_{eq}=1/\omega C_{eq}$, which is not zero. Thus there is always a phase difference between the voltage and the current. The power factor would not be 1. According to the viewpoint of the power factor correction, the case of parallel inductor is better than the case of series inductors.



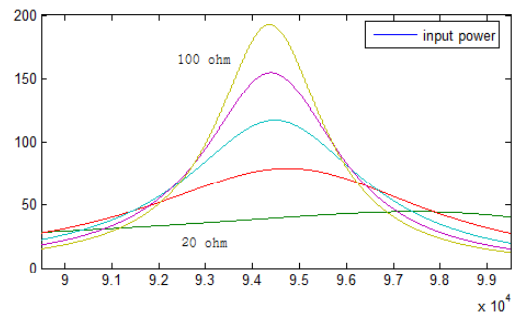
It should be noted that the maximum power points tracking (MPPT) can only track the maximum power points, but cannot guarantee to track the maximum power factor or said make the power factor correction (PFC) simultaneously. In fact, the condition of the PFC is stricter. The PFC condition means there is no equivalent reactive component, but the MPPT allows the equivalent reactive component to be independent of the load value. More specifically, PFC condition also includes the MPPT condition. This discussion implies that voltage and current waveforms at the PT output terminal influence the characteristics of the PT significantly. Therefore, the first step to design procedure a PT in different applications is to understand the output waveforms and the load characteristics at the PT output terminal.

Table 3-4. The equivalent circuit of the PT output capacitor with different loads

	without inductor (case1)	series inductor (case2)	parallel inductor (case3)
original circuits			
equivalent circuits			
	$C_{eq} = C \frac{(\omega C_2 R_L)^2}{1 + (\omega C_2 R_L)^2}$	$L_{eq} = \frac{1}{\omega C_2} \frac{\omega^2 C_2 L_s (1 - \omega^2 C_2 L_s) - (\omega C_2 R_L)^2}{(1 - \omega^2 C_2 L_s)^2 + (\omega C_2 R_L)^2}$	$L_{eq} = \frac{(1 - \omega^2 C_2 L_p)}{(1 - \omega^2 C_2 L_p)^2 + (\omega L_p / R_L)^2}$
	$R_{eq} = \frac{R_L}{1 + (\omega C_2 R_L)^2}$	$R_{eq} = \frac{R_L}{(1 - \omega^2 C_2 L_s)^2 + (\omega C_2 R_L)^2}$	$R_{eq} = \frac{(\omega L_p / R_L)^2}{(1 - \omega^2 C_2 L_p)^2 + (\omega L_p / R_L)^2}$
MPPT condition	No	$L_s = \frac{1}{\omega^2 C_2}$	$L_p = \frac{1}{\omega^2 C_2}$
PFC condition	No	No	$L_p = \frac{1}{\omega^2 C_2}$
efficiency	$\eta = \frac{R_L}{[1 + (\omega C_2 R_L)^2] R_m + R_L}$	$\eta = \frac{R_L}{(\omega C_2 R_L)^2 R_m + R_L}$	$\eta = \frac{R_L}{R_m + R_L}$
optimal loading condition	$R_L = \frac{1}{\omega C_2}$	$R_L \rightarrow 0$	$R_L \rightarrow \infty$
<ol style="list-style-type: none"> 1. Maximum power point tracking (MPPT) condition: $dC_{eq}/dR_L = dL_{eq}/dR_L = 0$ 2. Power factor correction (PFC) condition: $C_{eq} = L_{eq} = 0$, which include the MPPT condition. 3. Optimal loading condition: $d\eta / dR_L = 0$ 			



(a)



(b)

Figure 3-8. (a) The voltage gain and (b) the power characteristics of the PT with series inductor and

resistive load

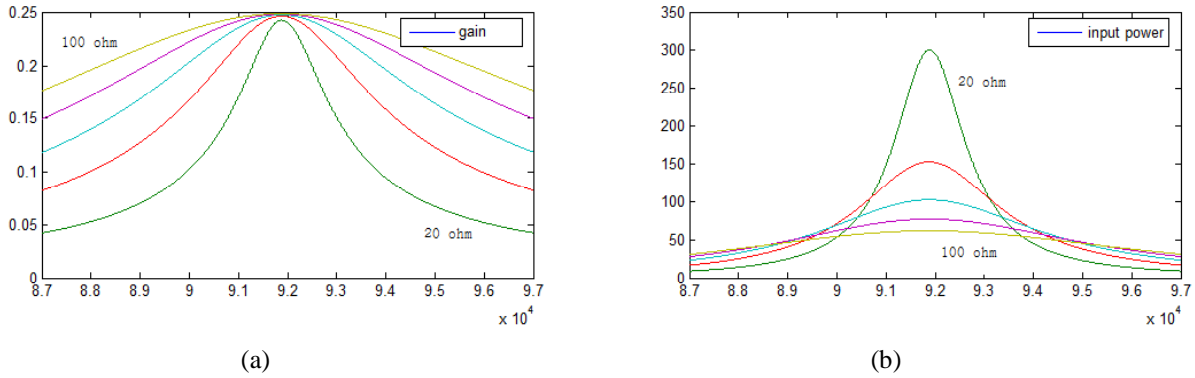


Figure 3-9. (a) The voltage gain and (b) the power characteristics of the PT with parallel inductor and resistive load

3.3 The input driving circuits of PTs

There are two popular types of driving circuit for the PT: the half-bridge driving circuit and the half push-pull driving circuit. Table 3-5 makes a simple comparison between these two topologies. The half push-pull driving circuit has fewer components and generates easily a sinusoidal-like voltage to supply the PT. Therefore, the half push-pull driving circuit was widely used before. However, the operation of the half push-pull circuit is similar to a quasi-resonant circuit, which implies that the variation of the duty cycle may cause the half push-pull circuit to operate incorrectly. Moreover, the operation of half push-pull driving circuit is also sensitive to the loading condition. According to these two limitations, the half push-pull circuit is only suitable in the application with constant load, such as lamp inverter and ballast.

The half-bridge circuit does not have these limitations, although it has two switching components. Therefore, in this dissertation, the half-bridge circuit was only discussed in

detail due to its wide range of applications.

Table 3-5. The comparison of the practical input driving circuits

	Half-bridge	Half Push-pull
topologies		
waveforms		
component	Two switches and one inductor	One switch and one inductor
control methods	1. PWM control with duty cycle 0-50% 2. PFM control	PFM control
ZVS condition	easy to achieve in the wide load variation	sensitive to the load

The basic topology and the operation of the half-bridge circuit are presented in Figure 3-10 and

Table 3-6 respectively. The high-side switch Q_1 and low-side switch Q_2 are turned ON and turned OFF alternatively to generate a square voltage. In practice, it exists a delay time at the switching instant. This delay time may conduct the two switches to be turned “ON” in a short period, leading voltage V_{DC} to be shorted to the ground.

Therefore, the two switches have to be turned OFF in a short period to ensure the circuit to operate correctly. This short period is called “dead time” because there is no

energy flow from the DC source to the PT. The function of the input inductor L_1 is to achieve a resonance with the PT input capacitor C_1 . This resonant tank can filter out high harmonic currents and increase the range of the ZVS (zero voltage switching) condition [19, 24]. The more detail operation will be shown in the following paragraphs.

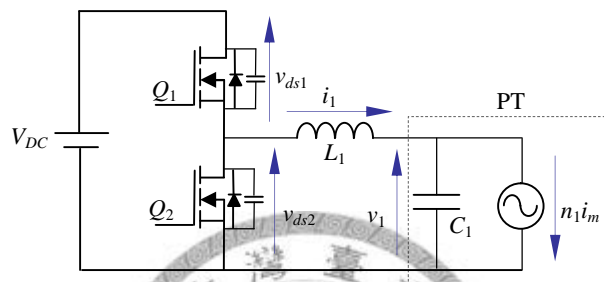


Figure 3-10. The half-bridge driving circuits with a piezoelectric transformer

Table 3-6. The basic operation of the half-bridge circuit

States	Switch Q_1	Switch Q_2	The key to achieve ZVS conditions
High	ON	OFF	To generate the positive voltage
Dead time	OFF	OFF	To ensure input DC voltage do not in short circuit
Low	OFF	ON	To generate the zero voltage

In practice, one important requirement of the switching driving circuit is the ZVS condition. In switching power circuits, MOSFETs are usually used as switching components. MOSFETs have a drain to source parasitic capacitance C_{ds} . When the switch is at the “OFF” state, the parasitic capacitor is charged. At the instant of switching from “OFF” state to “ON” state, the voltage on the parasitic capacitor v_{ds}

varies rapidly and thus a spike current i_{spike} is generated, *i.e.* $i_{spike}=C_{ds}(dv_{ds}/dt)$. The spike current induces switching losses and becomes a source of EMI (ElectroMagnetic Interferences).

To solve these problems, the ZVS technique was proposed. The ZVS means the switch turns “ON” after the parasitic capacitor of the switch has been already discharged to zero voltage. Since voltage on the parasitic capacitor is fully discharged to zero, there is no voltage variation ($dv_{ds}/dt =0$) during the switching instant and thus the spike current cannot be generated. The basic operation of the half-bridge circuit in

Table 3-6 does not consider the ZVS condition carefully. The detailed operation of the ZVS-mode half-bridge circuit is depicted in Figure 3-11, and the corresponding waveforms are shown in Figure 3-12. Furthermore, the operation of the ZVS-mode half-bridge circuit with a PT is detailed as follows:

Step 1. $[t_0-t_1]$

In this period, switch Q_1 is “ON” and switch Q_2 is “OFF”, thus v_{ds2} is equal to V_{DC} . This state is over until switch Q_1 is turned OFF.

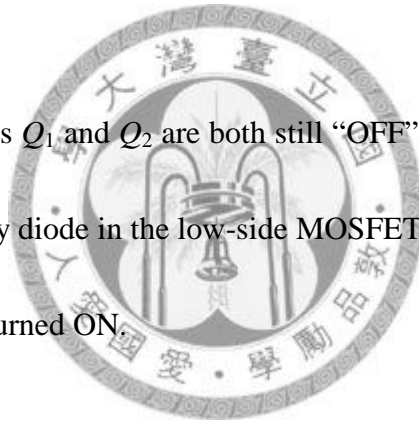
Step 2. $[t_1-t_2]$

In this period, the switches Q_1 and Q_2 are both “OFF”, so this period corresponds to “dead time”. To achieve the ZVS condition, the input current i_1 should flow in the positive direction (from the half-bridge circuit to the PT). According to the current

flowing direction, the capacitor C_{ds1} is charged and the capacitor C_{ds2} is discharged. Therefore, the voltage of the high-side MOSFET v_{ds1} increases until reaching V_{DC} , and the voltage of the low-side MOSFET v_{ds2} decreases until reaching zero voltage. This period is the key of the ZVS condition. If the dead time is not large enough, voltage v_{ds2} cannot be fully discharged to zero and the low-side switch cannot be turned “ON” at zero voltage in the following stage. Therefore, increasing the dead time or the input current can help capacitor C_{ds2} to fully discharge.

Step 3 [t_2 - t_3]

In this period, switches Q_1 and Q_2 are both still “OFF”. Since voltage v_{ds2} has been discharged to zero, the body diode in the low-side MOSFET is forward bias. This period is over when switch Q_2 is turned ON.



Step 4 [t_3 - t_4]

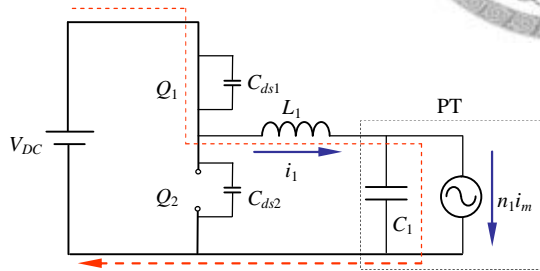
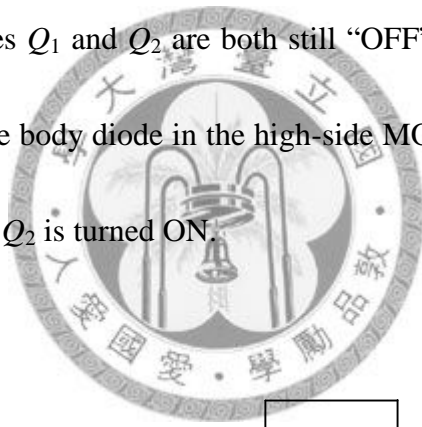
In this period, switch Q_1 is “OFF” and switch Q_2 is “ON”. Since the voltage of the low-side switch has reached zero in the last period, switch Q_2 is turned ON at the zero voltage condition, at instant t_3 . In addition, the input inductor L_1 and the PT input capacitor C_1 achieve the resonance in this period. To ensure switch Q_1 can switch at zero voltage condition in the following period, this resonance has to make the flowing direction of input current i_1 reverse at instant t_4 .

Step 5 [t_4 - t_5] :

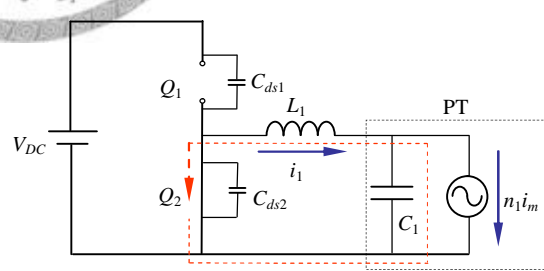
In this period, switches Q_1 and Q_2 are both “OFF”. The input current i_1 should flow in the negative direction (from PT to the half-bridge circuit) and capacitor C_{ds1} is discharged and capacitor C_{ds2} is charged. Therefore, the voltage of the high-side MOSFET v_{ds1} decreases until reaching zero, and the voltage of the low-side MOSFET v_{ds2} increases until reaching V_{DC} . Actually, this period is similar to *Step 2*, but the input current i_1 is in a different direction.

Step 6 [t_6-t_0] :

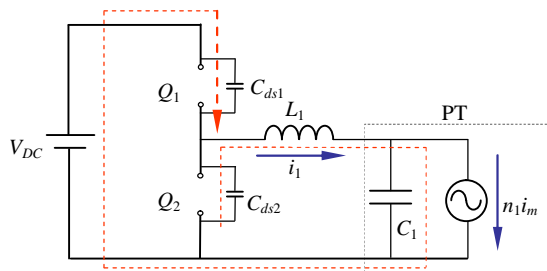
In this period, switches Q_1 and Q_2 are both still “OFF”. Since the voltage v_{ds1} has been discharged to zero, the body diode in the high-side MOSFET is forward bias. This period is over when switch Q_2 is turned ON.



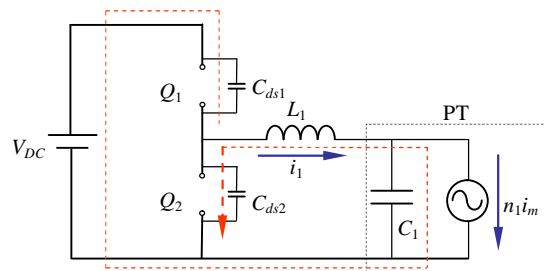
Step 1 [t_0-t_1]: voltage v_{ds2} at high state



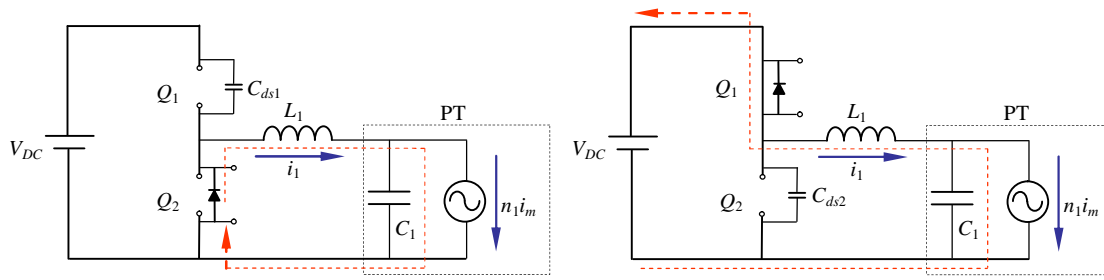
Step 4 [t_3-t_4]: voltage v_{ds2} at the low state



Step 2 [t_1-t_2]: C_{ds2} is discharged at dead time



Step 5 [t_4-t_5]: C_{ds1} is discharge at dead time



Step 3 [t_2 - t_3]: dead time

Step 6 [t_5 - t_0]: dead time

Figure 3-11. The operation of the ZVS-mode half-bridge circuit with a PT

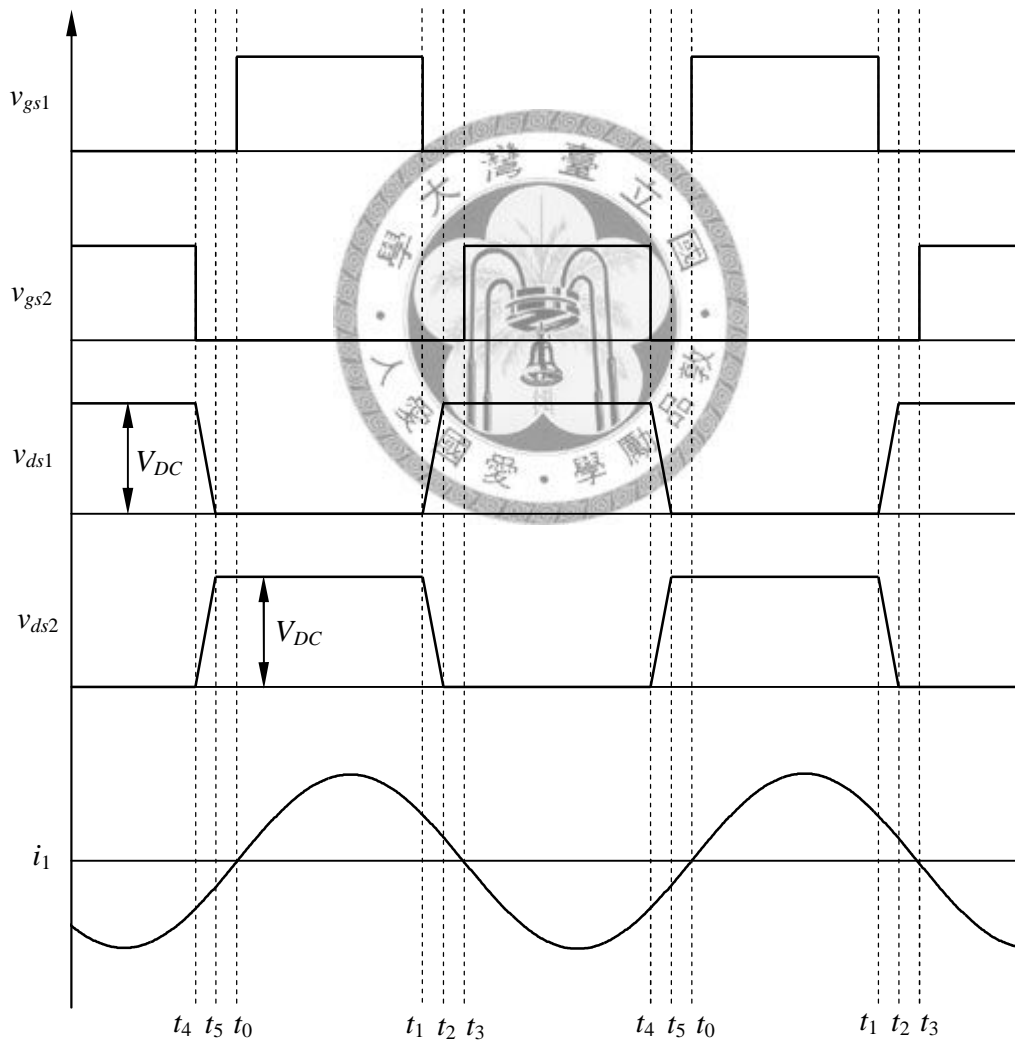
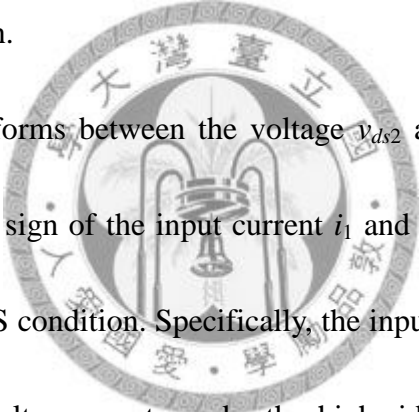


Figure 3-12. The waveforms of the ZVS-mode half-bridge circuit with a piezoelectric transformer

Table 3-7. The operation of the ZVS-mode half-bridge circuit with a PT

Steps	Switch Q_1	Switch Q_2	The key to achieve ZVS conditions
Step 1 [t_0-t_1]	ON	OFF	The LC resonance (input inductor L_1 and PT input capacitor C_1) must make the input current i_1 flow in the positive direction
Step 2 [t_1-t_2]	OFF	OFF	<ol style="list-style-type: none"> 1. Input current i_1 must flow in the positive direction. 2. The dead time and the input current i_1 have to large enough to make the capacitor C_{ds2} discharged to zero voltage.
Step 3 [t_2-t_3]	OFF	OFF	High-side switch Q_2 can be turned ON at zero voltage here.
Step 4 [t_3-t_4]	OFF	ON	The LC resonance (input inductor L_1 and PT input capacitor C_1) must make the input current flow in the negative direction.
Step 5 [t_4-t_5]	OFF	OFF	<ol style="list-style-type: none"> 1. Input current i_1 must flow in the negative direction. 2. The dead time and the input current i_1 have to large enough to make the capacitor C_{ds1} discharged to zero voltage.
Step 6 [t_5-t_6]	OFF	OFF	Low-side switch Q_1 can be turned ON at zero voltage here

Table 3-7 arranges the operations of the half-bridge circuit with a PT and the ZVS condition. It should be noted that the ZVS condition of the high-side switch Q_1 and the low-side switch Q_2 are similar but independent. Based on the discussion above, it can be noticed that the input current i_1 is obviously the key of the ZVS condition. Specifically, there are two main points of ZVS conditions: 1) the relationship between the voltage v_{ds2} and the input current i_1 and 2) the magnitude of the input current during the dead time should be large enough.



The anticipated waveforms between the voltage v_{ds2} and the input current i_1 are shown in Figure 3-13. The sign of the input current i_1 and the sign of dv_{ds2}/dt must be opposite to achieve the ZVS condition. Specifically, the input current i_1 must be negative at the rising time of the voltage v_{ds2} to make the high-side switch Q_1 achieves ZVS condition. However, this condition does not guarantee the low-side switch Q_2 can achieve ZVS condition. The input current i_1 must be also positive at the falling time of the voltage v_{ds2} to make the switch Q_2 achieve ZVS condition.

To describe this fact clearly, assume the high-side switch Q_1 is at ZVS condition and thus the input current i_1 is negative at the rising time of the voltage v_{ds2} . Table 3-8 lists three possible conditions under this assumption.

Case 1. The frequency of the input current is set near the switching frequency:

According to Table 3-8, it can be seen that both two switches can achieve ZVS condition when the frequency of the input current is set near the switching frequency. However, it should be noted that the ZVS condition may change when the duty cycle varies. The range of the duty cycle variation is marked in the figure of case 1 in Table 3-8.

Case 2. The frequency of the input current is the *higher* than the switching frequency:

In this case, the low-side switch Q_2 may achieve or not the ZVS condition. In fact, when the frequency of the input current i_1 is set near the odd harmonics of voltage v_{ds2} , the low-side switch Q_2 can achieve ZVS condition as well. Specifically, when the duty cycle is near 50%, it mainly includes the odd harmonic components. If the frequency of the input current is set near an harmonic component, the low-side switch Q_2 can achieve ZVS condition as well. It should be noted that the ZVS condition is changed when the duty cycle is varied since the harmonic frequencies are changed as well. This fact implies that there is only a small range of duty cycle variation in this case.

Case 3. The frequency of the input current is the *smaller* than the switching frequency:

In this case, two switches cannot both achieve the ZVS condition at the steady state. In the last row of Table 3-8, even if the two switches achieve the ZVS condition in certain period; they cannot keep the ZVS condition in the following period.

According to these three cases studied above, we can summary that the frequency

of the input current has to be set higher than the switching frequency. However, a too high frequency makes difficult to achieve the ZVS condition and leads to a smaller range of the duty cycle variation. Therefore, the frequency of the input current is better set a little bit higher than the switching frequency.

The input current includes two components: L_1C_1 input resonant current and the mechanical current. The frequency of the mechanical current or said the operating frequency of the PT should be set near the switching frequency to transfer the power efficiently. However, the L_1C_1 resonant frequency does not necessary fit the switching frequency, but the L_1C_1 resonant frequency should be higher than the switching frequency ω_s to ensure the possibility of the ZVS conditions, *i.e.* $\omega_s < \frac{1}{\sqrt{L_1C_1}}$.

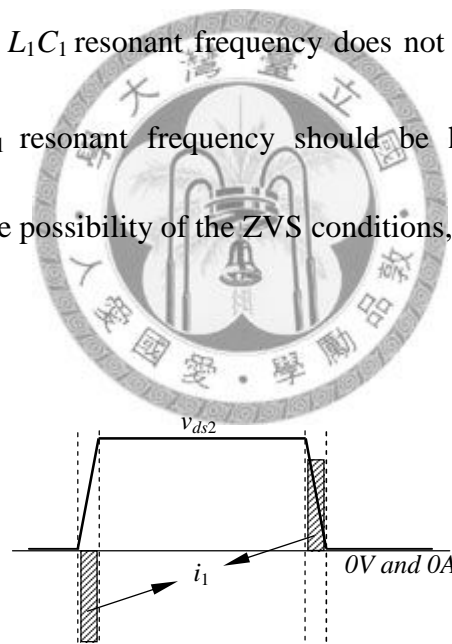
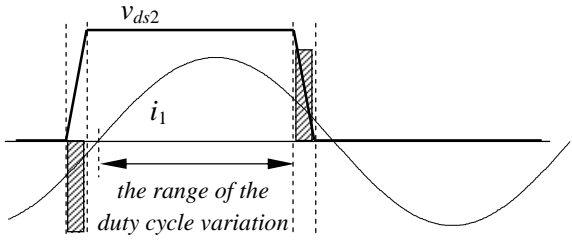
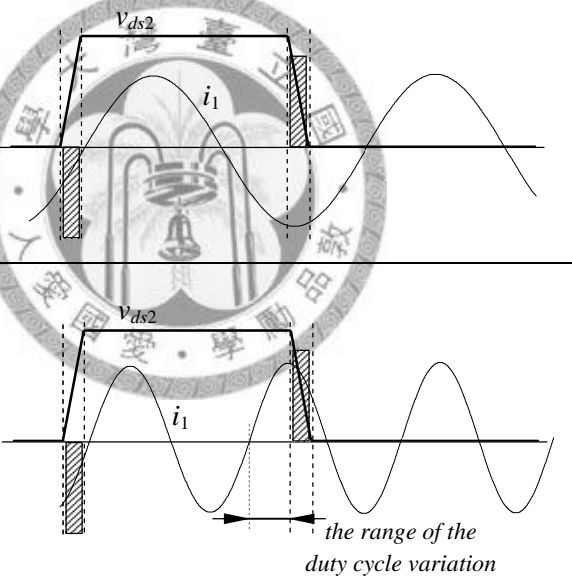
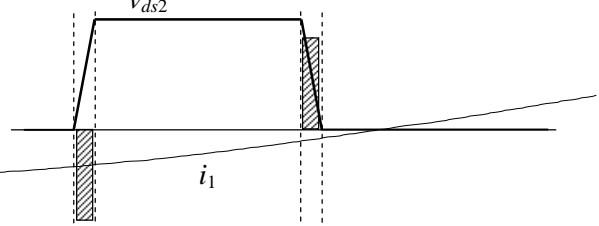
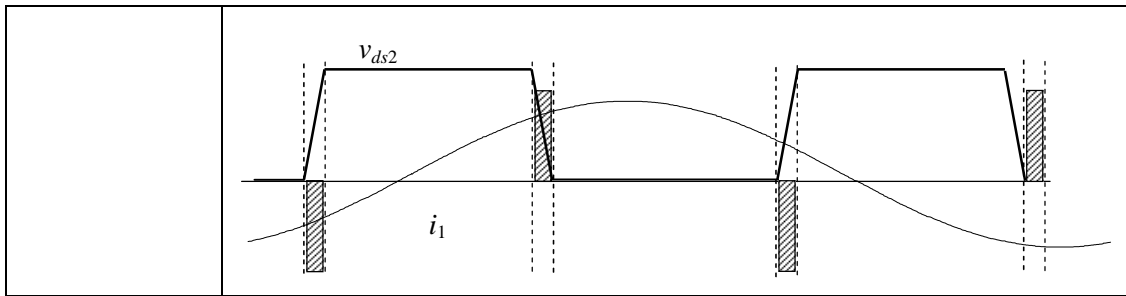


Figure 3-13. The anticipated relationship between the voltage v_{ds2} and the input current i_1

Table 3-8. The relationship between the voltage v_{ds2} and the input current i_1 in different frequencies

	Waveforms
Case 1.	<p style="text-align: center;">Near the switching frequency $\langle Q_2$ can achieve ZVS condition \rangle</p> 
Case 2.	<p style="text-align: center;">Higher than the switching frequency $\langle Q_2$ may achieve ZVS condition \rangle</p> 
Case 3	<p style="text-align: center;">Smaller than the switching frequency $\langle Q_2$ cannot achieve ZVS condition \rangle</p> 



On the other hand, at the rising time of voltage v_{ds2} , the negative current means the input current i_1 has to lag the voltage v_{ds2} . To get a lag current, the voltage v_{ds2} has to enter into an inductive input network. The input network includes the L_1C_1 resonant tank and the mechanical current sink. The L_1C_1 resonant tank here is a LC series resonance. In the LC series resonance, the impedance is capacitive below the resonant frequency and is inductive above the resonant frequency, which is shown in Figure 3-14 (a). The impedance characteristics of the mechanical current sink is based on the impedance characteristics of PT.

The equivalent circuit of PT is a LCC series-parallel resonant circuit. The LCC series-parallel resonance is only inductive in the resonant range (resonant range is the frequency range between the series resonant frequency and the parallel resonant frequency) and is capacitive in the other frequency ranges. It should be noted that the impedance characteristic of the PT is load-dependent in the resonant range. Figure 3-14 (b) shows the PT impedance with the load variation. It can be seen that the PT impedance may be capacitive or inductive in the resonant range. The input impedance

of the power stage is the superposition of the L_1C_1 series resonant tank and the PT with a load, as shown in Figure 3-15.

There are two possible inductive regions, which are the resonant range of the PT and the frequency range above the L_1C_1 resonant frequency. Since the mechanical current may be inductive, it implies the ZVS condition can be achieved without the input inductor L_1 . In such a case, however, the ZVS condition is highly load-dependent. In addition, if there is no inductive network, the PT is supplied by the square wave directly. Accordingly, the higher harmonic components of the input voltage excite the residual vibration modes more easily and thus decrease the efficiency of the PT. The detail behavior of the residual vibration will be analyzed in the following section.

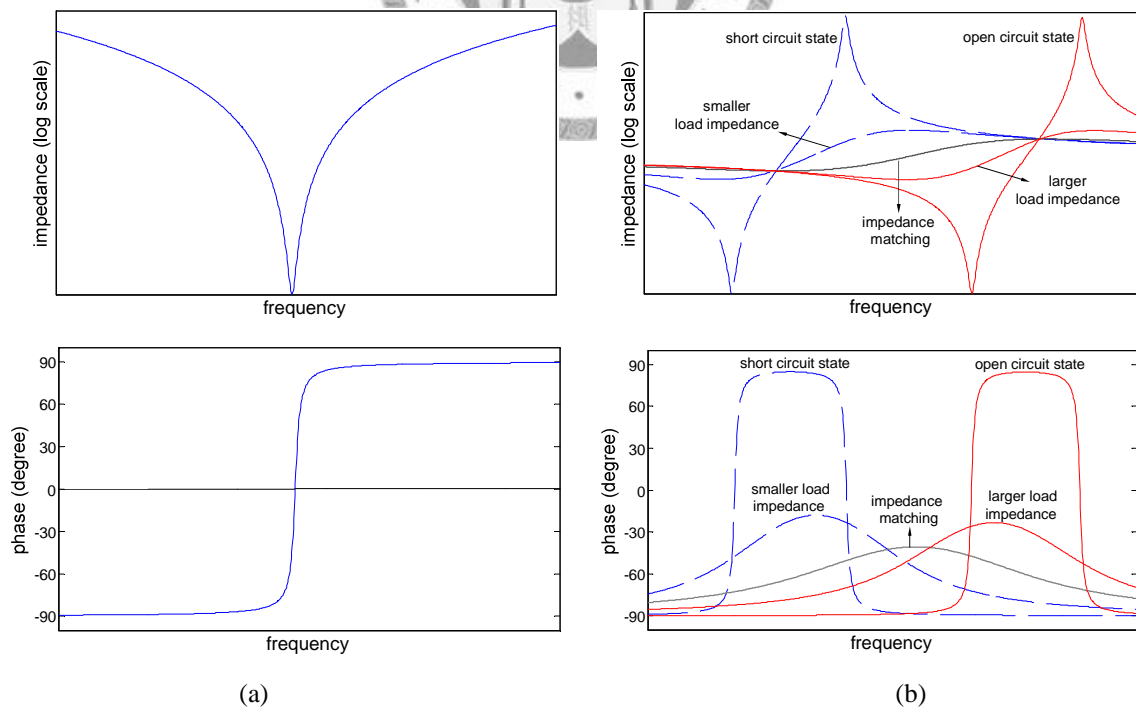


Figure 3-14. The impedance and phase of the (a) LC resonance (b) PT with the load variation

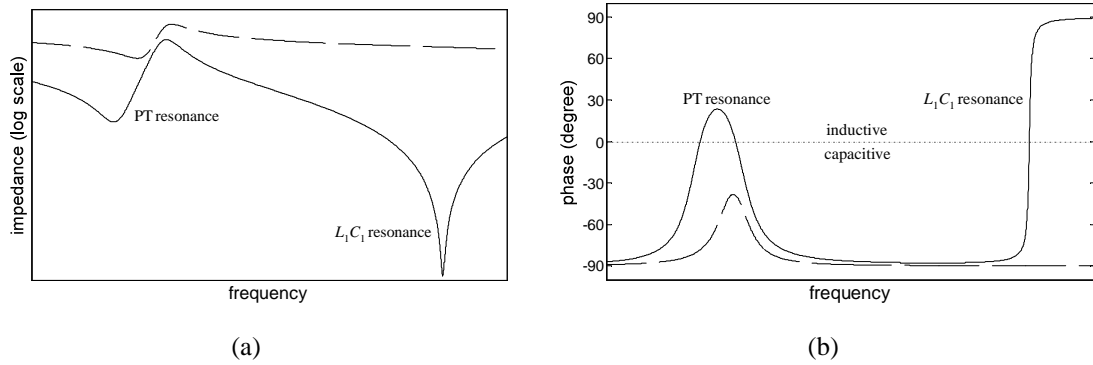


Figure 3-15. (a) The impedance magnitude and (b) impedance phase of piezoelectric transformers with a series inductor

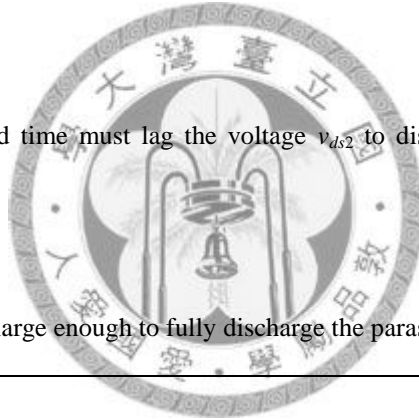
Besides the relationship between voltage v_{ds2} and input current i_1 , the magnitude of the input current must be large enough to discharge the parasitic capacitor of the MOSFETs. The capacitor discharge follows the relationship $i=C (dv/dt)$. Since the dead time t_d is short, the discharge current should be:

$$i_m + i_{LC} > C_{ds} \frac{V_{DC}}{t_d} \quad (3-10)$$

where i_{LC} is the current from L_1C_1 resonance. The discharge current is the current during the dead time, which includes the mechanical current i_m and L_1C_1 resonant current. It should be noted that when the PT can be inductive originally, current i_m lags voltage v_{ds2} . The mechanical current can help achieving the ZVS condition. However, when the PT is capacitive and the mechanical current i_m leads voltage v_{ds2} during the dead time, the mechanical current cancels the L_1C_1 resonant current. The ZVS condition is thus more difficult to achieve. Table 3-9 resumes constraints for ZVS conditions.

Table 3-9. The constraints for ZVS conditions

	The discharge current source	Constraints of the ZVS condition
Without inductive network	Mechanical current i_m	<ol style="list-style-type: none"> 1. Sensitive to the load variations 2. lower efficiency
With inductive network	Input L_1C_1 resonant current and inductive mechanical current i_m	<ol style="list-style-type: none"> 1. L_1C_1 resonant frequency has to be larger than the switching frequency 2. ZVS condition is related the duty cycle variation
ZVS conditions: <ol style="list-style-type: none"> 1. The current during the dead time must lag the voltage v_{ds2} to discharge the parasitic capacitor of MOSFETs. 2. The discharge current must large enough to fully discharge the parasitic capacitor of MOSFETs. 		



3.4 Summary

This chapter demonstrated the basic properties of the piezoelectric transformers. The output characteristics of the piezoelectric transformer were detailed. The piezoelectric transformers are the highly load-dependent components since the resonant frequencies of the piezoelectric transformers are dependent to the load impedance. The load-dependent characteristic is due to the phase difference of the mechanical current and the piezoelectric output voltage. The inductive compensation was also demonstrated

to fix the resonant frequencies. As to the input section of the piezoelectric transformer, the ZVS-mode half-bridge input driving circuit was introduced. The detail operations and the ZVS conditions of the half-bridge input driving circuit were demonstrated. The ZVS condition is the basic requirement of the piezoelectric transformers based converters in the following chapters to achieve the highly efficient converter.





Chapter 4. Rosen-type Piezoelectric Transformers based CCFL

Inverters

A simple Rosen-type piezoelectric transformer based backlight inverter and its design rules are fully developed in this chapter. Even though piezoelectric inverters are more efficient than the electro-magnetic inverters in this type of application that converts low voltage to high voltage, variable control methods were usually adopted typically to fully realize this advantage. The complexity of the control method makes piezoelectric transformer (PT) difficult to use in large systems such as LCD-TV. In this section, we start from the CCFL (cold cathode fluorescent lamp) characteristics to understand the requirements and then we examine the mechanical current, the power curve and the loading condition of the Rosen-type piezoelectric transformer. The result implemented in a commercial 32" LCDTV proves the efficiency of our design.

4.1 The characteristics of the CCFL (cold cathode fluorescent lamp)

There are several characteristics of the fluorescent lamp have to be mentioned first before designing the CCFL inverter:

1. *Steady state impedance:* [\[25, 26\]](#)

Even though CCFL is a very complex load, the CCFLs (Cold Cathode Fluorescent Lamps) can be emulated as a resistor in the steady state since the voltage and the current

on the CCFL are in phase. The CCFL impedance is the ratio of the lamp voltage and the lamp current in the root mean square values. Furthermore, the steady-state resistance of the CCFL is current-dependent, which can be shown to be:

$$R_{Lamp} = \frac{V_s}{i_{Lamp}} - r, \quad (4-1)$$

where R_{Lamp} and i_{Lamp} are the resistance and the current of the CCFL respectively, V_s and r are constants derived from the characteristics of CCFL. In this dissertation, CCFLs of effective length 656mm currently used commercially is used as the experimental load, and linear curve-fit the testing data is shown in Figure 4-1 leads to:

$$V_s = 1426, \quad r = 49545 \quad (4-2)$$

According to equation (4-2) and ohm's law, the relationships between the power and the load impedance of the CCFL can be obtained, they are shown in equation (4-3) and

Figure 4-1(b).

$$P_{lamp} = V_s^2 \frac{R_{lamp}}{(R_{lamp} + r)^2} \quad (4-3)$$

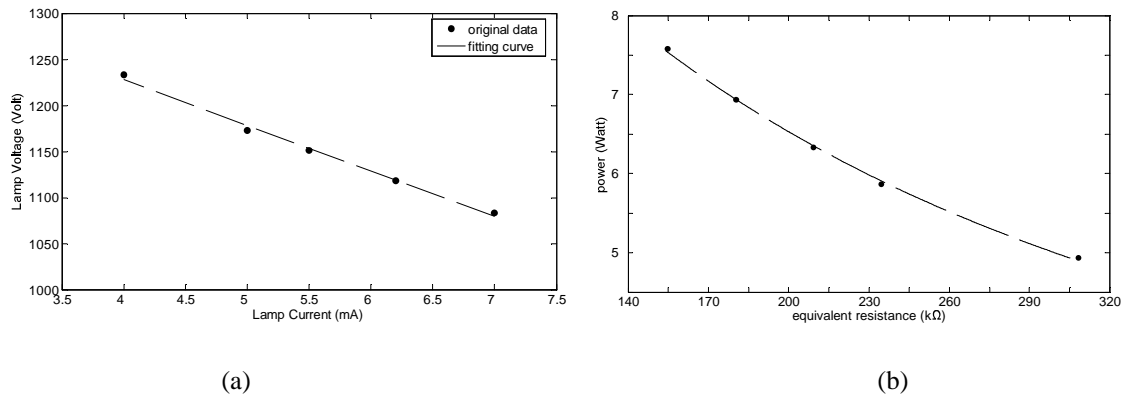
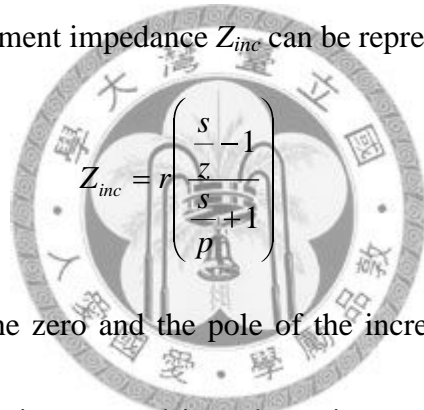


Figure 4-1 (a) The voltage-current curve and (b) The power-resistance curve of the lighting CCFL

2. *Negative incremental impedance* [25, 26, 27, 28]:

Incremental impedance is the ratio of the small-signal perturbation in lamp voltage over the lamp current. The perturbation with different frequencies causes different impedance. For example, when the lamp current is varied fast, the lamp current follows line A in Figure 4-2. In the case of a slow-varying lamp current, the lamp current follows line B in Figure 4-2. Therefore, the lamp incremental impedance is negative when frequency is slow varying but positive for high frequency varying. According to this phenomenon, the incremental impedance Z_{inc} can be represented as:



$$Z_{inc} = r \left(\frac{\frac{s}{z} - 1}{\frac{s}{p} + 1} \right) \quad (4-4)$$

where z and p represent the zero and the pole of the incremental impedance. At zero frequency, the value of the incremental impedance is equal to the slope of the steady state impedance r . Therefore, the order of the numerator and the denominator are equal and there is a RHP (right half plane) zero in the incremental impedance. If the CCFL is driven by the voltage source directly, the generated current owns a RHP pole, i.e. $i_{lamp} = v_{lamp}/Z_{inc}$. The RHP pole causes the system to become unstable. Therefore, a network with high incremental impedance is required to connect between the switching power stage and the lamp to stabilize the lamp current. The circuit of the power switching stage and the connected network is also called electrical ballast.

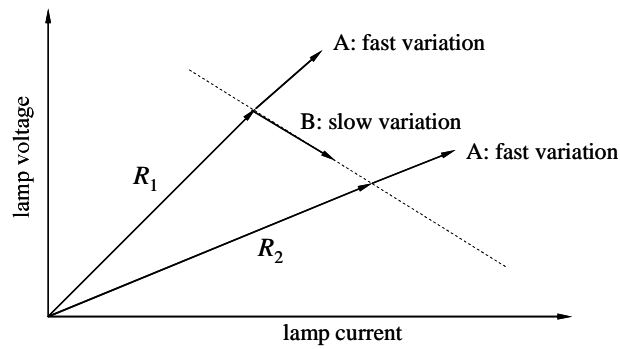


Figure 4-2. The small-signal perturbation of the fluorescent lamp operating at high frequency

3. Lamp current crest factor: [27]

The current crest factor is defined as the peak current of the waveform divided by the RMS value of the current. The life of the CCFL is sensitive to the lamp current crest factor. Specifically, smaller crest factor leads to a longer life of the CCFL. The perfect square, triangle and sinusoidal waveforms have crest factors 2, 1.7 and 1.4 respectively. That is, pure sinusoidal waveform is most suitable to drive the CCFL. Therefore, the resonant network is usually set between the switching stage and the CCFL to transfer the switching waveform to the sinusoidal waveform on the CCFL. There are three commonly-used resonant networks, which are LC series resonant, LC parallel resonant and LCC series-parallel resonant networks. The LC parallel and the LCC series-parallel resonant networks can have high impedance at their parallel resonant frequencies. However, even if the impedance of the resonant network is not high enough, we also can use the feedback loop to stabilize the lamp.

4. *High strike voltage:*

Before the CCFL is lighted, the CCFL is almost an open circuit. The CCFL needs a high strike voltage to start up. After it has started up, the impedance of the CCFL decreases, the required lamp voltage and the lamp impedance at steady state are also decreased. The strike voltage is roughly 1.5 times of the steady state lamp voltage in most cases. The voltage conversion gain of the LCC resonant converters is highly dependent on the load impedance. LCC resonant converter can easily produce very high voltage gain at high load impedance condition and have a lower gain at small load impedance condition, which just fit the lamp characteristics. Therefore, LCC resonant converter is well suited to drive CCFL due to all the characteristics mentioned above.

The impedance of piezoelectric transformers includes the mechanical resonance and a parallel capacitor which forms the LCC resonance. Piezoelectric transformer can provide a perfect sinusoidal voltage to the CCFL and obtain good crest factor. However, it should be noted that connecting the LCC resonance network/piezoelectric transformer between the voltage source and the lamp do not guarantee the stability of the lamp. It is difficult to achieve stability at series resonance/structural resonance. However, stability can be achieved by using the external feedback loop. In addition, the Rosen-type piezoelectric transformer can easily have the high voltage conversion gain in the open circuit state since the input impedance and the output impedance of the Rosen-type PT

is much different due to the different poling directions of input section and the output section. Consequently, the Rosen-type PT can easily start up the lamp and both have the good crest factor.

4.2 Physical limitations of the PT and the CCFL

As the CCFL can be emulated as a resistor in steady state, the equivalent circuit of the Rosen-type PT based CCFL inverter can be represented in Figure 4-3. There are two assumptions in this equivalent circuit.

1. The mechanical current is purely sinusoidal in steady state,
2. The lamp current i_L is controlled as a constant RMS value at specific frequency to maintain the constant brightness of the lamp,

Based on these two assumptions, the mechanical current can be viewed as a current source. The equivalent circuit in Figure 4-3 can be further reduced as Figure 4-4.

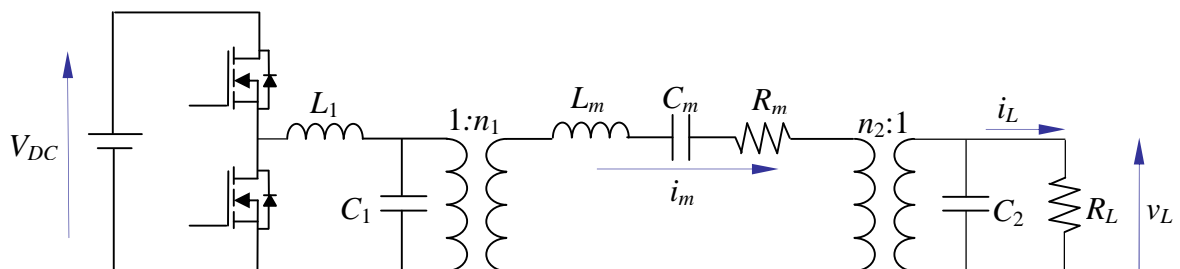


Figure 4-3. Equivalent circuit of half-bridge PT based CCFL inverter

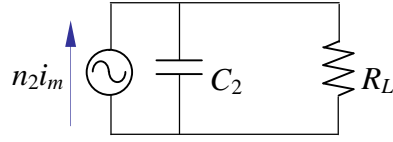


Figure 4-4. PT fed by resistive load

According to Kirchoff's current law, the load current can be derived as:

$$i_L = \frac{n_2 i_m}{1 + s C_2 R_L} \quad (4-5)$$

The required mechanical current in the converter is determined by the load current.

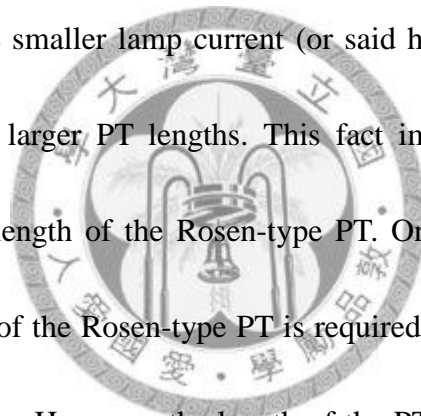
$$i_m = \frac{i_L}{n_2} \sqrt{1 + (\omega C_2 R_L)^2} < i_{m,\max} \quad (4-6)$$

The mechanical current of the PT has the maximum value since the larger mechanical current leads to larger mechanical losses, *i.e.* $i_m^2 R_m$. To have the smaller mechanical current, the transformation ratio n_2 should be as large as possible. However, we can only design the dimensional parameters of the PT in practical applications. To understand the relationship between the mechanical current and the dimensional parameters clearly, substitute the equivalent circuit components in Table 3-2 into equation (4-6) Leads to

$$i_m = i_L \frac{s_{33}^E}{d_{33}} \sqrt{\left[\left(\frac{L}{2WT}\right)^2 + \left(\frac{2\pi N_1 \epsilon_{33}^S R_L}{L}\right)^2\right]}. \quad (4-7)$$

According to equation (4-7), it is obvious that the width W and the thickness T of the PT should be large to decrease the mechanical current under the constant lamp current condition, but the tendency of the length L is not clear. In this dissertation, we have adopted the PZT material provided from ELECERAM TECHNOLOGY Co. LTD, and

the material properties are listed in Table 4-2. First, substituting the material properties into equation (4-7) and setting $W=10\text{mm}$, $T=2\text{mm}$ to observe the practical tendency between the PT length and the mechanical current. Then, we have fixed the lamp current at 5mA making varying the product $W*T$ for different kind of PT . Figure 4-5 shows the resulting mechanical currents versus different lengths with different lamp currents. There are 5 curves in Figure 4-5(a), which represent the different lamp currents from 4 to 9mA with 1mA step variation. It seems that there is a minimum mechanical current in each curve. The smaller lamp current (or said higher lamp impedance), the minimum points occur at larger PT lengths. This fact implies that the higher lamp impedance require larger length of the Rosen-type PT. Once the length of the CCFL increase, the larger length of the Rosen-type PT is required to have smaller mechanical current and better efficiency. However, the length of the PT is limited by the operating frequency in practice. In general, the CCFL have an optimal operating frequency range. In such a range, the brightness efficiency and the life of the lamp are optimal. The CCFL adopted in this dissertation should be set in the frequency range 40-70kHz, which corresponds to the PT length from 45.7mm to 80mm. It can be seen that the PT length cannot be too large, or the mechanical current will be too high. In this design example, the operating frequency of the CCFL is set near 60kHz and the corresponding Rosen-type PT length is 53mm. Furthermore, the mechanical current is set below 0.45A



and the load current is set at 7mA, the product of the PT width and the PT thickness should be set below 18mm² based on equation (4-7).

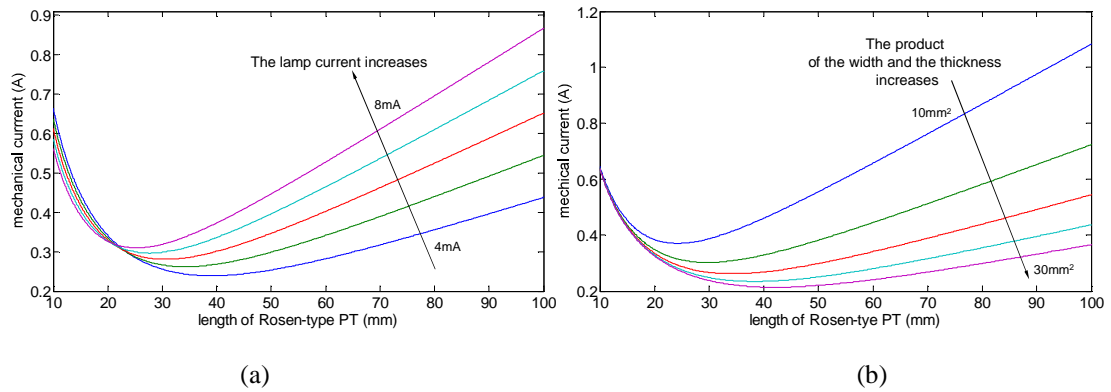


Figure 4-5. The mechanical currents versus lengths of the Rosen-type PT with (a) different lamp currents

(b) different products of the PT width and the PT thickness

Table 4-1. The equivalent circuit of the Rosen-type piezoelectric transformer

ω_o	L_m	C_m	R_m	C_1	C_2	n_1	n_2
$\frac{4\pi N_l}{L}$	$\frac{\rho_m LWT}{8}$	$\frac{1}{L_m \omega_o^2}$	$\frac{1}{Q_m} \sqrt{\frac{L_m}{C_m}}$	$\frac{WL \epsilon_{33}^S}{2T}$	$\frac{2WT \epsilon_{33}^S}{L}$	$\frac{Wd_{31}}{s_{11}^E}$	$\frac{2WTd_{33}}{Ls_{33}^E}$

Table 4-2. The Material properties of the Rosen-type PT

<p><u>Material properties (PZT-QA, ELECERAM TECHNOLOGY Co., LTD.):</u></p> <p>$N_p = 1600$ is the frequency constants of the longitudinal vibration (kHz•mm)</p> <p>$\rho_m = 7950$ is the density (kg/m³)</p> <p>$\nu = 0.16$ is the Poisson's ratio</p>

$Q_m = 1800$ is the mechanical quality factor

$\varepsilon_{33}^S = 1450 * 8.854 * 10^{-12}$ is the permittivity at constant strain condition, i.e. constant S (F/m)

$d_{33} = 340 * 10^{-12}$ are the piezoelectric constants (m/V)

$s_{33}^E = 1.47 * 10^{-11}$ is the compliance constant under the constant electric field, i.e. constant E

4.3 Design of the Rosen-type PT based CCFL inverter

Both the PT mechanical current and the operating frequency of the CCFL are the physical limitations. In addition, it is important to design a piezoelectric transformer to fit lamp voltage and lamp current at the same time for supplying the CCFL efficiently. So the step-up ratio and the output current of the piezoelectric transformer should be examined. As CCFL can be emulated as a resistive load in steady state, these relationships are mentioned in equations (3-2~5). Applying equations (3-2~5), the output power of the piezoelectric transformer can be obtained:

$$P_{out}(\omega, R_L) = \frac{R_L (nv_{in})^2}{[(1 + n^2 \omega C_2 X)^2 + (n^2 \omega C_2 R_m)^2] R_L^2 + (2n^2 R_m) R_L + n^4 (R_m^2 + X^2)}, \quad (4-8)$$

where:

$$X = -\text{Im}[Z_{ME}] = \frac{1 - \omega^2 C_m L_m}{\omega C_m}. \quad (4-9)$$

The output power of the piezoelectric transformer shown in equation (4-8) and the required power of the CCFL shown in equation (4-3) have similar expressions and similar exponent orders with load impedance R_L . When piezoelectric transformer is

connected to CCFL, i.e. $R_L = R_{Lamp}$, it seems that the conditions of tracking the power of the CCFL could be obtained by identifying the coefficients of equation (4-3) and equation (4-8). However, these conditions are not useful in practice. The underlying reason is that the power variations of the piezoelectric transformer and the CCFL are not identical and there are too many conditions to match simultaneously. In addition, although the external load impedance may vary with the environment, such as the temperature, its change can generally be controlled within a pre-specified range per specifications. Therefore, the power curve of the piezoelectric transformer and the CCFL only need to be identified within specific load range.

Table 4-3. A piezoelectric transformer testing model

V_{in}	C_1	R_m/n_1^2	L_m/n_1^2	$n_1^2 C_m$	n_1/n_2	C_2
200V _{rms}	1.36nF	13.78Ω	67.10mH	92.59pF	5.27	9.35pF

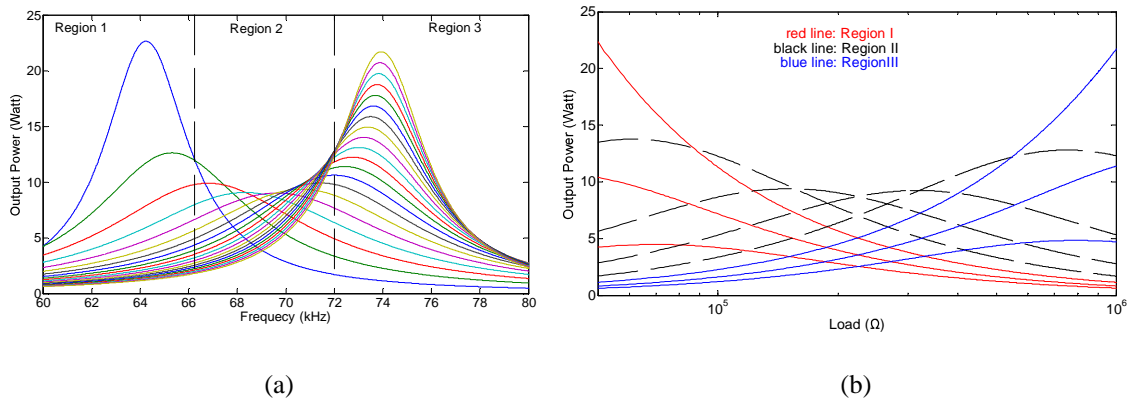


Figure 4-6. Output power of the piezoelectric transformer (a) versus frequencies (b) versus loads

To observe the output power of the piezoelectric transformer, a Rosen-type PT model in Table 4-3 is adopted as an example. In this case, the load varies from 50kΩ to 1000kΩ (Figure 4-6). Figure 4-6(a) can be roughly divided into three regions. In region I, the power decreases when the load impedance increases. This is similar to the relationship between the power and the load impedance of CCFL shown in Figure 4-1. In region II, the power and the load impedance do not have clear trend. In region III, the power increases when the load impedance decreases. This is in conflict with the power characteristics of CCFL. Figure 4-6(b) shows the curve of regions I, II and III in more detail. This simple observation implies that it may be possible to track the power of the CCFL in region I, but difficult in region II and impossible in region III. Region I is thus called the region of negative-slope in this dissertation. In the negative-slope region, the power changed with the load negatively, i.e.

$$\frac{dP_{out}(\omega, R_L)}{dR_L} < 0 \quad (4-10)$$

When the piezoelectric transformer and the input voltage of the piezoelectric transformer are chosen, the output power of the piezoelectric transformer can be viewed as the function of the operating frequency and the load impedance. Apply equations (4-8-10), the discriminant of the region of the negative impedance can be obtained:

$$n^4(R_m^2 + X^2) - [(1 + n^2\omega C_{out}X)^2 + (n^2\omega C_{out}R_m)^2]R_L^2 < 0 \quad (4-11)$$

On the other hand, it is known that piezoelectric transformer is efficient in the resonant region, i.e., the region between the resonant frequency and the anti-resonant frequency. More specifically, the piezoelectric transformer should be both set in the resonant region and the negative-slope region at the same time to track the power of negative impedance with good efficiency.

According to the equivalent circuit in Figure 3, the resonant frequency of the piezoelectric transformer is:

$$\omega > \omega_r = \sqrt{\frac{1}{L_m \frac{C_m C_{eq}}{C_m + C_{eq}}}}, \quad (4-12)$$

where ω_r is the resonant frequency of the piezoelectric transformer and where:

$$C_{eq} = -\frac{1}{\omega \operatorname{Im}[Z_{HPF}]} = n^2 C_2 \frac{1 + (\omega C_2 R_L)^2}{(\omega C_2 R_L)^2}. \quad (4-13)$$

According to equations (4-10~13), the condition on the load range for driving a CCFL is obtained as follows:

$$R_{\inf} < R_L < R_{\sup}, \quad (4-14)$$

where:

$$R_{\sup} = \sqrt{\frac{-n^2 X}{\omega^2 C_2^2 (1 + n^2 \omega C_2 X)}}, \quad (4-15)$$

$$R_{\inf} = \sqrt{\frac{n^4 (R_m^2 + X^2)}{(1 + n^2 \omega C_2 X)^2 + (n^2 \omega C_2 R_m)^2}}, \quad (4-16)$$

and R_{sup} and R_{inf} are the upper bound and lower bound of the range of the load impedance. It should be noted that equations (4-14~16) are only valid in the specific frequency range. More specifically, each piezoelectric transformer can only drive the CCFL in specific frequency and load range. On the other hand, equation (4-14~16) does not consider the efficiency completely. Tracking the negative-slope power curve, it can only ensure that the CCFL can be regulated by the piezoelectric transformer itself and thus the efficiency of the piezoelectric transformer would not change significantly. Operating in resonant range can only ensure piezoelectric transformer obtain good efficiency. Both conditions do not guarantee piezoelectric transformer operate in the highest efficiency condition.



In fact, the efficiency of the piezoelectric transformer relates only to the real part of the impedance as only the real part of the impedance dissipates the power. Therefore, according the equivalent circuit shown in Figure 3-7, the efficiency of the piezoelectric transformer becomes:

$$\eta = \frac{\text{Re}[Z_{HPF}]}{\text{Re}[Z_{ME}] + \text{Re}[Z_{HPF}]} \quad (4-17)$$

Once the piezoelectric transformer is chosen, equation (4-17) determines the load impedance. It can easily be found that maximum efficiency is achieved when:

$$R_L^* = \frac{1}{\omega C_2} \quad (4-18)$$

where the superscript (*) represents the condition of the highest efficiency.

However, it should be noted that when condition shown in equation (4-18) is achieved, the real part of Z_{HPF} is maximum and the piezoelectric transformer output power is minimum at the optimal loading condition. Using the optimal loading condition shown in equation (4-18) and the equality condition in equation (4-12), the resonant frequency in the optimal loading condition becomes:

$$\omega_r^* = \sqrt{\frac{C_m + (2n_2^2 C_2)}{L_m C_m (2n_2^2 C_2)}} \quad (4-19)$$

Considering the relationship between the optimal load and the region of power tracking is a case of interest. By substituting equations (4-18) and (4-19) into the upper and lower bounds of the load impedance shown in equations (4-15) and (4-16) yields that:

$$R_{\text{inf}}^* = R_L^* = R_{\text{sup}}^* \quad (4-20)$$

In addition, we can see that if the operating frequency is higher than the resonant frequency under the optimal loading condition, i.e. $\omega > \omega_r^*$, equation (4-14) will never be satisfied. In other words, the operating frequency must be smaller than the resonant frequency under the optimal loading condition in order to drive a negative-slope power, *i.e.*

$$\omega < \omega_r^* \quad (4-21)$$

Equations (4-20) and (4-21) show that optimal loading condition is just the boundary of the negative-slope region. However, if the operating frequency is set at resonant

frequency with optimal load or if the connecting load matches the optimal loading condition, the load remains constant such that the piezoelectric transformer fails to track the power of negative-impedance load. In fact, if the operating frequency is close to the resonant frequency with optimal load, the piezoelectric transformer has the best efficiency but less ability to deal with load variation. In comparison, if the operating frequency is smaller than the resonant frequency for optimal load, the piezoelectric transformer is less efficient but has better ability to deal with load variations. In other words, there is a trade-off between load variations and efficiency.

This understanding also implies that the piezoelectric transformer cannot handle wide load variations automatically. For different lamps or even same lamp with different load ranges, the piezoelectric transformer should be re-designed accordingly. According to equations (4-18) and (4-21) and the discussion above, the loading condition for negative impedance becomes:

$$R_L < \frac{1}{\omega C_2} \quad (4-22)$$

which implies that the output static capacitor should not match the load perfectly, but must be set to a value higher than the one of the load.

Table 4-4 shows the design constraints of the PT based CCFL inverter. For a single layer Rosen-type piezoelectric transformer, there are at least four parameters to fit the design constraints: i.e., the operating frequency, the length, the width, and the thickness.

Furthermore, the input and output electrodes can also be design parameters even though they are not significant parameters to shape the power curve of the load.

On the other hand, although input voltage of the piezoelectric transformer is a significant and easily implemented design parameter for the output power. The input voltage is typically set by the system requirement. For example, the notebook computer is typically powered by battery, which sets the voltage range available. In LCDTV system, however, more choices are available for the supply voltage. As the piezoelectric loss depends on the mechanical current flow through the piezoelectric transformer, higher input voltage should be set to obtain higher efficiency.

In this section, the input voltage was chosen to be 120 Volt and 400 Volt.

Table 4-4. The design constraints of the Rosen-type PT

Constraints	Purposes	Corresponding PT dimensional factors	Values in the design example
Operating frequency	Matching the lamp characteristics	Length	$L=53\text{mm}$ (operated near 60kHz)
Small Mechanical current	Higher efficiency	Larger width/thickness, smaller mechanical current	$WT>18\text{mm}^2$
Negative slope of	Load variation/stability	$WT > \frac{\epsilon_{33}^s L}{\omega} R_L$	$WT>13.2\text{mm}^2$

power curve			
Sufficient power/current	Matching the lamp voltage/current	All	$P_{lamp}=7.7\text{Watt}/i_{lamp}$ $=7\text{mA}$
ZVS Conditions	Reducing switching loss	Non	Set proper series inductor

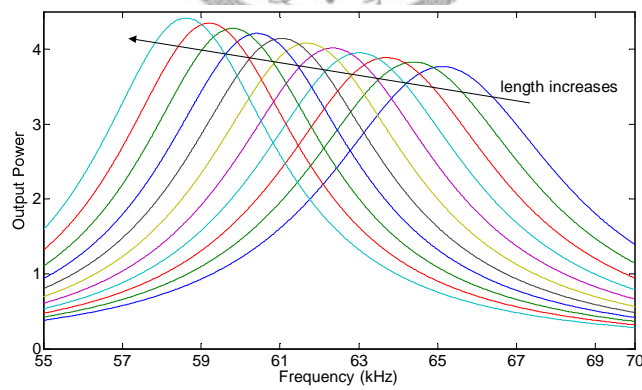
It is not easy to find the analytical solution of the output power with the dimensional parameters, *i.e.* length, width, and thickness. Three cases shown in Table 4-5 are used in the numerical simulations to see the relationship between the power curve and the dimensional parameters. In Figure 4-7, it is shown that length variations change the resonant frequency and the width and the thickness influences the output power value significantly. Each CCFL has its suitable operating frequency to obtain the largest lamp life.

As operating frequency is mainly decided by the length of the PT, it is better to chose the length first in order to ensure the operating frequency of the piezoelectric transformer stays in the suitable frequency range of CCFL. Width and thickness can be used to shape the power curve to make sure the output power provided by the piezoelectric transformer is enough to light the lamp while being able to handle the load variations.

In brief conclusion, three design parameters, i.e. length, width, and thickness, are used to match the three frequency operating requirements, i.e., the frequency of the lamp, sufficient power, and the various trend of the power curve.

Table 4-5. The testing size of the Rosen-type PT

	<i>Length L</i>	<i>Width W</i>	<i>Thickness T</i>
<i>case1</i>	48~53mm	fixed at 7.5mm	fixed at 2mm
<i>case2</i>	Fixed at 53mm	7.5~15mm	fixed at 2mm
<i>case3</i>	fixed at 53mm	fixed at 7.5mm	1.3~3mm
<i>conditions</i>	$V_{in}=120V_{rms}$ and $R_L=200k\Omega$		



(a)

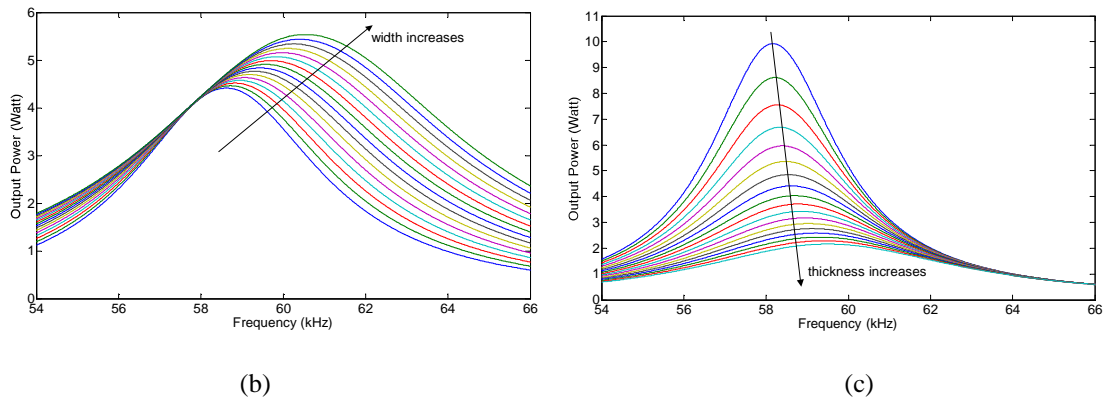


Figure 4-7. The dimensional variation of the Rosen-type piezoelectric transformers: (a) length (a) width (c)

thickness

Before choosing the optimal width and thickness of the piezoelectric transformer, it should be noted that it was known that the larger width or larger thickness of the Rosen-type PT can endure higher transfer of power. However, in Figure 4-7(c), the smaller thickness admits higher power transformation. This is because smaller thickness leads to larger electro-mechanical transformation ratio n_1 and thus leads to smaller input impedance. More specifically, the smaller thickness allows higher power transfer, but it does not guarantee the piezoelectric transformer can endure higher power transfer.

The simplest way to solve this problem is to set a lower bound on the thickness. This thickness lower bound ensures the piezoelectric transformer itself can endure enough power while setting the preferred thickness. Although it was known that the width and the thickness can shape the power curve, the relationships between the width and thickness are not clear now. In fact, the loading condition in equation (4-22) can provide this relationship. Substituting the equivalent circuit model shown in Table 4-1

into the equation (4-22) yields that:

$$WT > \frac{\varepsilon_{33}^S L}{\omega} R_L \quad (4-23)$$

Equation (4-23) can ensure the piezoelectric transformer to operate in the negative-slope region. It is mentioned that the most efficient loading condition is the boundary condition of equation (4-22). To obtain higher efficiency and enough load variations, one can use equation (4-23) and start from smaller value of the width-thickness product to fit the power curve, i.e. $P_{out} = P_{lamp}$ up to the thickness lower bound. The full proposed optimization method is shown in Figure 4-8.

The targeted specification of LCD-TV is shown in Table 4-6. The length of piezoelectric transformers was chosen at 53mm to operate in suitable frequency range of CCFL. In addition, there are two conditions that should be satisfied at the same time, i.e. the load power and the load variation, which are shown in equations (4-8) and (4-10) respectively. It should be noted that the analytic model in this paper do not consider the other resonant mode of piezoelectric transformer. However, load current also includes harmonic components, especially the third harmonic of the fundamental frequency. The third harmonic current is roughly the 0.095 of the total current by experiment. On the other hand, load voltage waveform is sinusoidal as the piezoelectric transformer is a good band-pass filter. This fact implies the third harmonic load current may influence the value of load impedance, but load power would not be significantly influenced.

Owing to harmonic current also contributes to the brightness of CCFL, the load power should be corrected with the factor 0.095. It is important to make the model correction here because piezoelectric transformers are sensitive to the load characteristics.

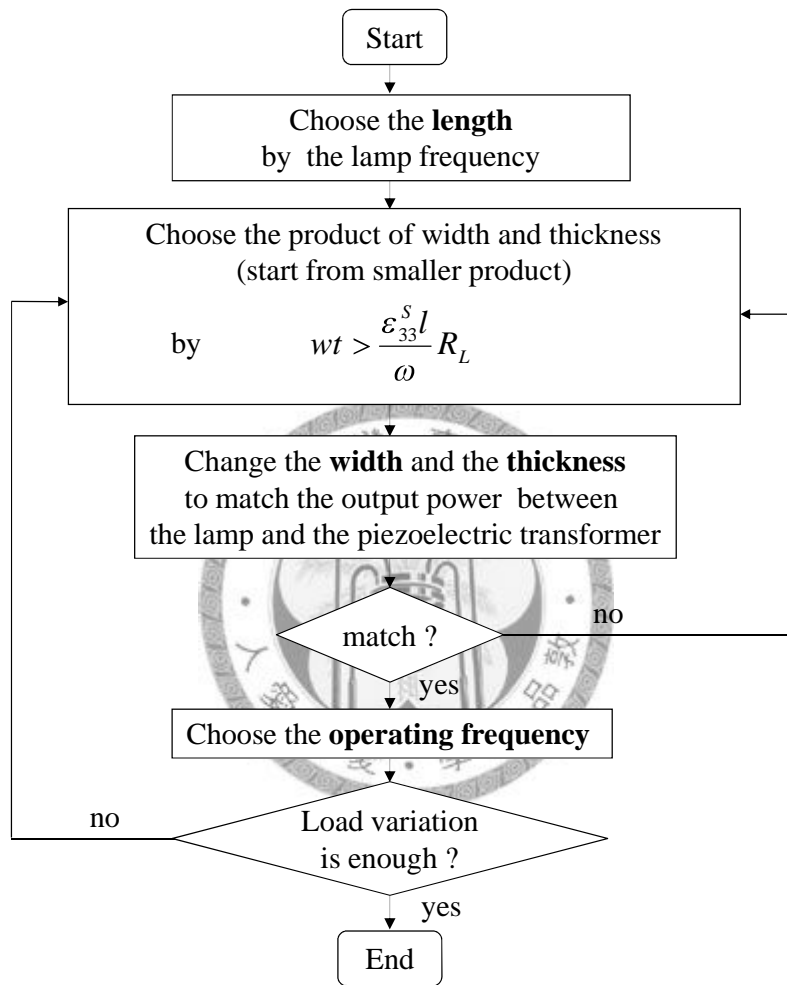


Figure 4-8. the fully optimal procedure of the single-layer Rosen-type piezoelectric transformer

Table 4-6. the specification of CCFL in LCDTV

input voltage (DC)	400Volt
driving circuit	half-bridge
operating frequency (kHz)	40k~70kHz

lamp current (V)	7 mA _{rms}
------------------	---------------------

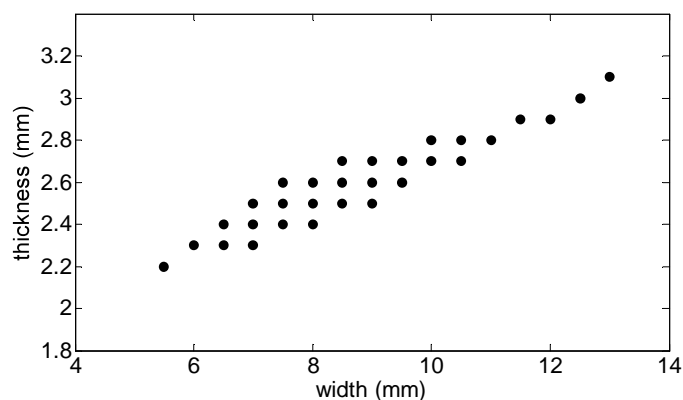
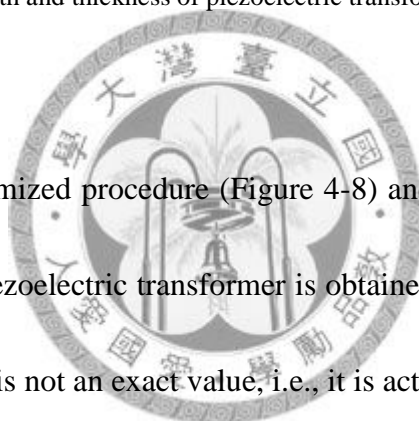


Figure 4-9. optimal width and thickness of piezoelectric transformers with length 53mm



According to the optimized procedure (Figure 4-8) and the specification of CCFL (Table 4-6), the optimal piezoelectric transformer is obtained in Figure 4-9. It should be noted that the optimal size is not an exact value, i.e., it is actually located within a range.

The larger size causes large losses due to the larger mechanical resistance.

To examine the correction of the optimal size, therefore, width 7.5mm with four different thicknesses: 2mm, 2.4mm, 2.6 mm were manufactured (see Figure 4-10), the corresponding temperature rise are shown in Table 4-7. Consider both the size and the temperature rise; the size 53*7.5*2.4 mm would be better one, which agrees well with the result shown in Figure 4-9 and mechanical current. The half-bridge circuit is used to drive two piezoelectric transformers at the same time with a 3mH series inductor (Figure 4-11). This series inductor is used to achieve the zero voltage switching

condition and does not change the curve of output power significantly. The load voltage and the load current are shown in Table 4-8. This piezoelectric transformer based inverter works with only 3°C temperature rise. It can also see that load impedances of both two testing CCFLs are located in the theoretical load range well. Figure 4-12 shows the test results of a commercially available LCDTV backlight lighted by using piezoelectric transformer based inverter with only 5°C temperature rise under room temperature at 25 °C.

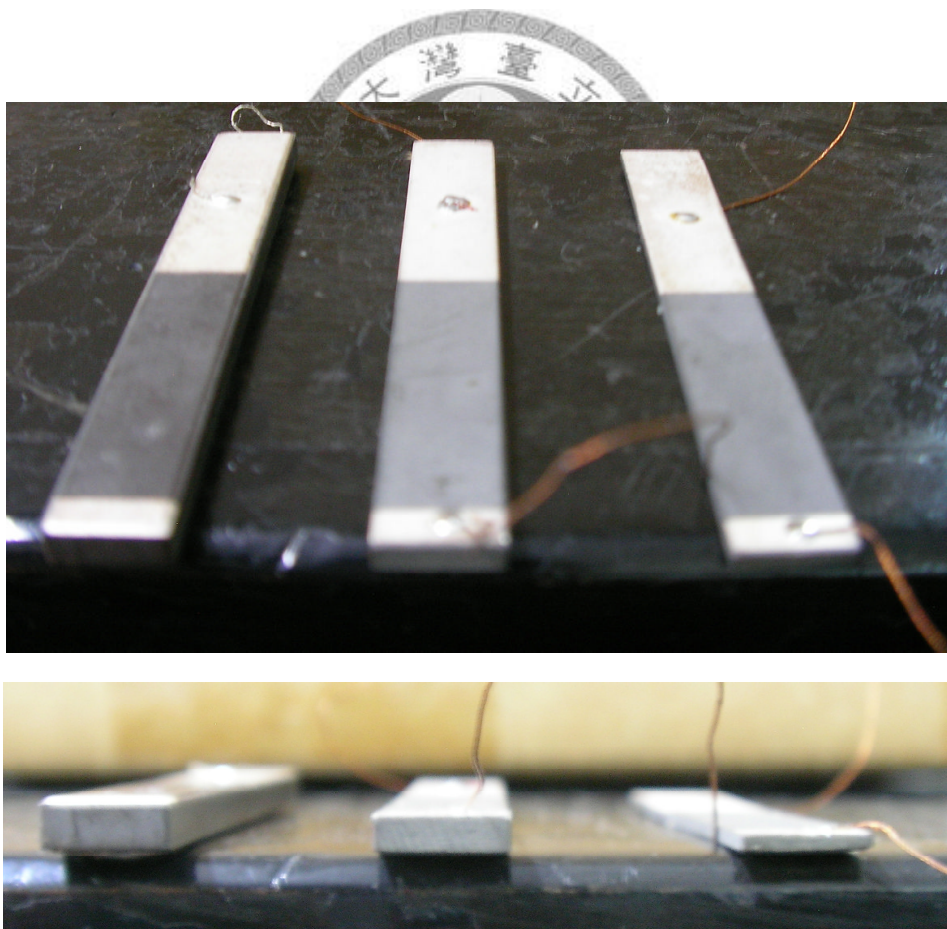


Figure 4-10. The specimens of the Rosen-type piezoelectric transformers

(from left to right are 2.6mm, 2.4mm and 2mm respectively)

Table 4-7. Specimens of Rosen-type piezoelectric transformers

Size of the piezoelectric transformer	Temperature rises
53*7.5*2mm	Unstable
53*7.5*2.4mm	Within 10 °C
53*7.5*2.6mm	Within 7 °C

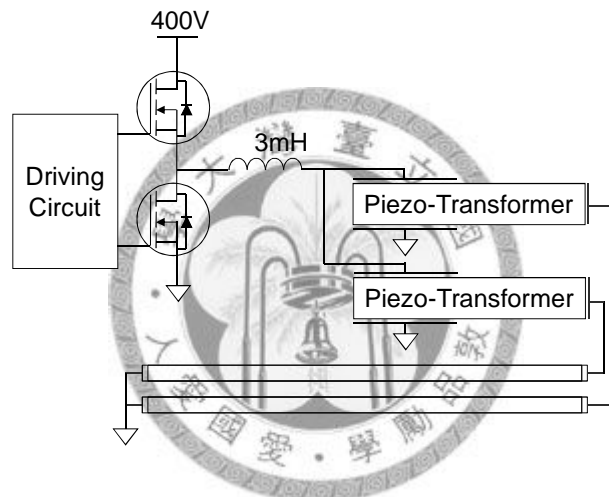


Figure 4-11. The piezoelectric transformer based inverter for two CCFLs

Table 4-8. The testing of optimal piezoelectric transformer based inverter

size of the piezoelectric transformer	53*7.5*2.4mm
operating frequency	60.3kHz
input power	18.8W
load voltage	1.23kV _{rms} and 1.20kV _{rms}
load current	6.98mA _{rms} and 7.16mA _{rms}

output power	17.04W
efficiency	90.6%
load impedance	176.22k Ω and 167.6k Ω
possible load variation by calculation	81.37k Ω ~ 196.09k Ω



Figure 4-12. The piezoelectric transformer based inverter for commercial 32'' LCDTV backlight

4.4 Summary

Piezoelectric transformer can efficiently drive CCFL at fixed frequency condition as long as the power curve between piezoelectric transformer and CCFL were considered carefully. The trend of these two power curves should be the same, and the concept of negative-slope range is thus derived in this chapter. In negative-slope region, the piezoelectric transformer has little ability to regulate the power. Consequently, the traditional impedance matching condition should be changed, which implies piezoelectric transformer should sacrifice its efficiency slightly to achieve

fixed-frequency operation. Combining two conditions of load power and load power variation leads to the design of a piezoelectric transformer of optimal size at specific frequency. In summary, the results shown in this chapter verify that the proposed design rule is suitable to design a piezoelectric transformer based inverter with fixed-frequency operation.





Chapter 5. Piezoelectric Transformer based DC/DC

Converter

The design of the piezoelectric transformer is more complex than the CCFL inverter due to the nonlinearity of the rectifier. In addition, the practical use of the DC/DC converter is to supply a low voltage but high current load, which is opposite the characteristic of piezoelectric transformers. Lin and Lee first proposed a design flow of a PT in the use of the DC/DC converter [11, 12]. In his paper, Lin states that the rectifier is equivalent to a pure resistor because the characteristics of the PT are well-known in this case. This method developed by Lin has been widely used to simplify PT design procedures, especially for resonant converters. However, this method is only correct when the input voltage and the input current of the rectifier are in phase at the operating frequency. If a phase difference exists between the voltage and the current, the equivalent impedance requires involving a reactive component. In most cases, it usually exists a phase difference between the input voltage and input current of the PT fed rectifier [13, 14]. The underlying reason lies in the output capacitor of the PT, which needs to be charged and discharged at each period. Moreover, the phase difference varies with the operating frequency and the load values. In other words, the phase difference cannot be neglected. Therefore, it is important to examine the output voltage/current waveforms of the PT directly and then incorporate it into the PT design

procedure. In this dissertation, the relationship between the vibration velocity and the waveforms of the PT fed rectifier is analyzed in detail to develop the general design procedure of the piezoelectric transformers under the constant load voltage condition. Then, the conducted electromagnetic interference (EMI) was then modeled and measured to prove the proposed converter have lower EMI than the electromagnetic converter.

5.1 Analysis of Piezoelectric Transformer fed Voltage-Mode Rectifiers

5.1.1 Topologies of the PT fed rectifiers

Based on the previous discussion, it was known that the PT needs an input driving circuit to excite PT vibrations and also an output interfacing circuit or network is required to condition the output signal in desired form. As the loads of PTs, there are basically two kinds of loads, they are AC loads and DC loads. AC loads and DC loads have AC voltage/current and the DC voltage/current across it respectively. The output signals from the PT are always AC signals due to PT transfer the energy efficiently by the vibration but not the deformation. Specifically, the PT is only transfer power efficiently near the resonance, so its operating frequency is near the resonant frequency of the PT. In the application of DC/DC or AC/DC converters, which is also the major interest of this dissertation, a DC load is connected to the PT [29, 30]. Therefore, a

rectifier has to be inserted in between the PT output terminal and the DC load. The complete block diagram of the PT based converter is shown in Figure 5-1. There are several different kinds of the rectifiers. It should be noted that there is no “best” choice of the rectifiers for PT basically, but only the “proper” choices. The selection is mainly based on the application and the targeted specification, but there are some basic criterions to choose a proper rectifier.

1. *fewer components:*

In practice, all components have internal loss. Fewer components normally induce less loss. Therefore, the simpler topologies of the rectifiers are preferred. At the same time, the simpler topologies also mean lower cost.

2. *higher power density of the PT:*

It prefers designing a PT which can transfer power as high as possible in the same volume, or say as high as the power density. Besides the improvement of the material, the interfacing circuit of the piezoelectric layer also influences the power density. For example, if there is a phase difference between the voltage and the current, the power at the PT output terminal flows in both directions of the piezoelectric layers.

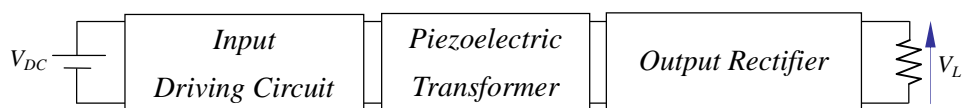


Figure 5-1. The block diagram of the PT based DC/DC converter

The high-bridge PT based DC/DC converter with voltage mode rectifier is shown in Figure 5-2. It should be noted that the PT transfers the energy at the switching frequency, but the load receives the energy in DC form. For simplicity of analysis, the converter can be divided into the fast system (AC switching frequency) and the slow system (DC load) based on two different operating frequencies. In our theoretical analysis, there are two basic assumptions:

1. The mechanical current i_m is pure sinusoidal wave in the steady state.
2. The filtering capacitance C_f is larger enough than the output capacitor C_2 of the PT, *i.e.* $C_2/C_f = 0$, so the load voltage V_L can be viewed as a perfect DC voltage sink.
3. The diode voltage drops is set 0.

According the principle of fewer components, two simple diode rectifiers are discussed which are voltage-mode full-wave rectifier and the half-wave rectifier. Based on the first assumption, the mechanical current can be equivalent to a sinusoidal source of the PT output capacitor and the rectifier (Figure 5-3).

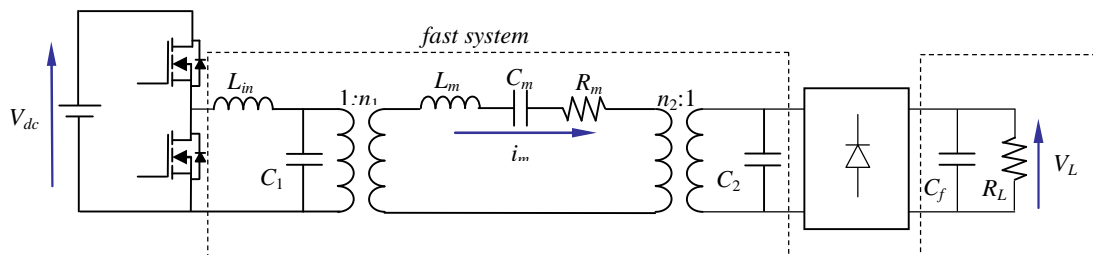


Figure 5-2. High-bridge PT based DC/DC converter with voltage mode rectifier

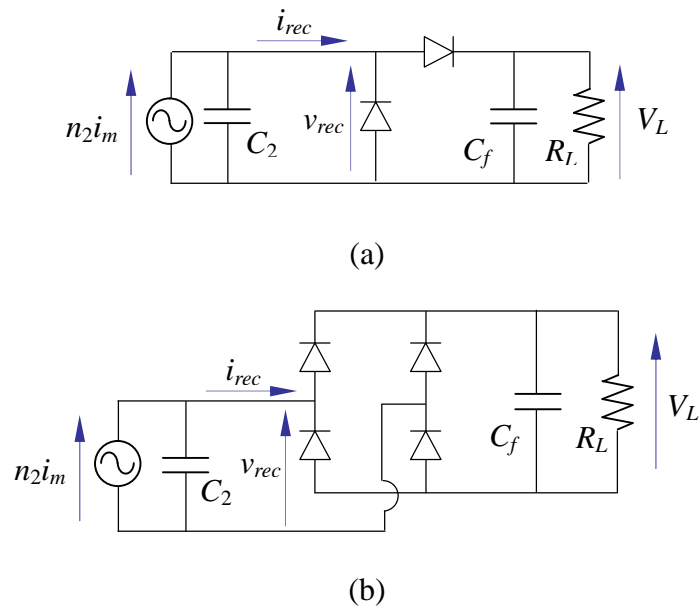


Figure 5-3. The PT fed (a) half wave and (b) full-wave voltage-mode rectifier

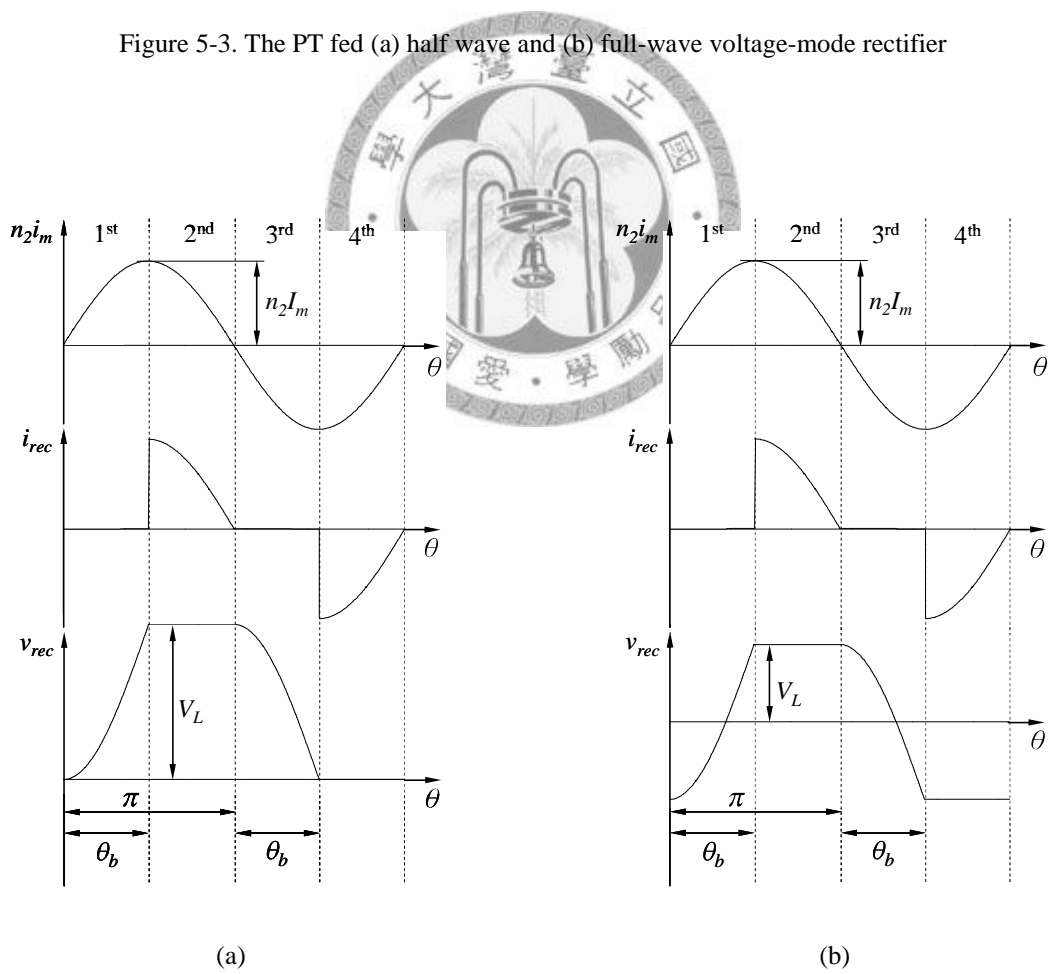
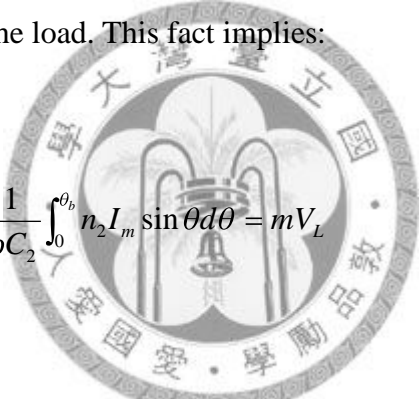


Figure 5-4. The voltage and current waveform in the input side of (a) the half wave and (b) the full-wave

voltage-mode rectifier

5.1.2 State equation of the slow system

According to the equivalent circuits in Figure 5-3, the current i_{rec} and voltage v_{rec} waveforms at the input of the rectifiers are shown in Figure 5-4. The waveform can be divided into four periods. In the first and third period, the diode is blocked, and the PT output capacitor is charging or discharging. When the voltage of the output capacitor is fully charged to the load voltage or discharge to zero voltage, the diodes start to conduct and the current flowing to the load. This fact implies:



$$\frac{1}{\omega C_2} \int_0^{\theta_b} n_2 I_m \sin \theta d\theta = m V_L \quad (5-1)$$

where θ is the phase angle, i.e. $\theta = \omega t$ and θ_b represents the phase angle when diode is blocked or called diode block angle. m is the parameter related to the charging voltage level. $m = 1$ in the half-wave rectifier but $m = 2$ in the full-wave rectifier. Charging voltage level is the fundamental difference between half-wave rectifier and the full-wave rectifier, hence the parameter m is adopted to distinguish the half-wave rectifier and the full-wave rectifier. Equation (5-1) can be derived to find the diode block angle:

$$\theta_b = \cos^{-1}\left(1 - \frac{m\omega C_2 V_L}{n_2 I_m}\right) \quad (5-2)$$

On the other hand, according to the equivalent circuits in Figure 5-3, the waveforms in Figure 5-4 and Kirchhoff's law, the state equations of the slow system can be obtained:

1st and 3rd period:

$$C_f \frac{dV_L}{dt} = -\frac{V_L}{R_L} \quad (5-3)$$

2nd period and 4th period of the full-wave rectifier:

$$(C_2 + C_f) \frac{dV_L}{dt} = -\frac{V_L}{R_L} + n_2 I_m \sin \omega t \quad (5-4)$$

4th period of the half-wave rectifier:

$$C_f \frac{dV_L}{dt} = -\frac{V_L}{R_L} \quad (5-5)$$

Since the frequency at the load is much smaller than the switching frequency, the average method can be adopted to find the linear state equations. Equations (5-3~5) can be combined by multiplying their period respectively. It should be noted that the 4th period of the full-wave rectifier and the half wave rectifier are not the same due to the waveform of the half-wave rectifier is not symmetric as the full-wave rectifier. After the average the waveform by each period, the average state equation of the slow system can be obtained as follows:

$$\dot{V}_L = -\frac{2\pi + m^2\omega C_2 R_L}{2\pi(C_L + C_2)R_L} V_L + \frac{2}{\pi(C_L + C_2)} n_2 I_m \quad (5-6)$$

When the system reaches the steady state, the derivative of load voltage is equal to zero,

i.e. $\dot{V}_L = 0$. Therefore, the load voltage can be expressed as:

$$V_L = \frac{2R_L}{2\pi + m^2\omega C_2 R_L} n_2 I_m \quad (5-7)$$

The diode block angle is re-arranged by substituting equation (5-7) into equation (5-2):

$$\theta_b = \cos^{-1}\left(\frac{2\pi - m^2\omega C_2 R_L}{2\pi + m^2\omega C_2 R_L}\right) \quad (5-8)$$

Equation (5-8) shows clearly the diode block angle is decided by the $\omega C_2 R_L$. In fact, $\omega C_2 R_L$ is a significant factor. This factor is related to the efficiency. It implies diode block angle is also related to efficiency. The efficiency of the PT can be written as:

$$\eta = \frac{\frac{V_L^2}{R_L}}{\frac{1}{2} I_m^2 R_m + \frac{V_L^2}{R_L}} \quad (5-9)$$

The optimal loading condition is occurred at $d\eta/dR_L = 0$. Therefore, the optimal loading condition of the PT with the voltage-mode rectifier can be derived as

$$R_L^* = \frac{2\pi}{m^2\omega C_2} \quad (5-10)$$

where the superscript ()^{*} represents the optimal efficient value. It should be noted that this optimal loading condition is larger than the well-known optimal loading condition.

The diode block angle becomes:

$$\theta_b^* = \frac{\pi}{2} \quad (5-11)$$

No matter full-wave or half-wave rectifier, the block angles are half period under at optimal loading condition. This is one of invariant characteristics under the optimal loading condition. After obtaining the characteristics of the slow system in steady state, another issue of interest is its small signal model. Adding the small perturbation into the

each signal and linearizing the state equation of the slow system at specific operating point. The small signal state equation of the slow system can be obtained:

$$\dot{\hat{V}}_L = -\frac{2\pi + m^2\omega C_2 R_L}{2\pi(C_L + C_2)R_L} \hat{V}_L + \frac{2}{\pi(C_L + C_2)} n_2 \hat{I}_m \quad (5-12)$$

where the cap superscript “^” represent the small perturbation. The output of interest is the load voltage, equation (5-12) yields the transfer function:

$$\frac{\hat{V}_L}{\hat{I}_m} = \frac{\frac{2n_2}{\pi(C_L + C_2)}}{s + \frac{2\pi + m^2\omega C_2 R_L}{2\pi(C_L + C_2)R_L}} \quad (5-13)$$

Both the dominate pole and the gain of the small signal model of the slow system are clear in equation (5-13). So far, the analytical model of the slow system is fully obtained. Some important characteristics of the slow sub-system in this section are arranged in Table 5-1.



Table 5-1. The characteristics of PT fed voltage mode rectifier

	Full-wave Rectifier	Half-wave Rectifier
load voltages	$V_L = \frac{2n_2 R_L}{2\omega C_2 R_L + \pi} I_m$	$V_L = \frac{2n_2 R_L}{\omega C_2 R_L + 2\pi} I_m$
load powers	$P_L = \left(\frac{2n_2}{2\omega C_2 R_L + \pi}\right)^2 I_m^2 R_L$	$P_L = \left(\frac{2n_2}{\omega C_2 R_L + 2\pi}\right)^2 I_m^2 R_L$
diodes block angles	$\theta_b = \cos^{-1}\left(\frac{\pi - 2\omega C_2 R_L}{\pi + 2\omega C_2 R_L}\right)$	$\theta_b = \cos^{-1}\left(\frac{2\pi - \omega C_2 R_L}{2\pi + \omega C_2 R_L}\right)$
optimal loading conditions	$R_L^* = \frac{\pi}{2\omega C_2}$	$R_L^* = \frac{2\pi}{\omega C_2}$

conduction angle at optimal conditions	$\theta_b^* = \frac{\pi}{2}$	$\theta_b^* = \frac{\pi}{2}$
small signal transfer functionss	$\frac{\frac{2n_2}{\pi(C_L + C_2)}}{s + \frac{2\pi + 4\omega C_2 R_L}{2\pi(C_L + C_2)R_L}}$	$\frac{\frac{2n_2}{\pi(C_L + C_2)}}{s + \frac{2\pi + \omega C_2 R_L}{2\pi(C_L + C_2)R_L}}$

5.1.3. State equation of the PT output capacitor

The average state equation of the slow system describes the dynamic/static characteristics of the filtering capacitor and the load voltage, but it cannot describe the behavior of the PT output capacitor. The underlying reason is that the load voltage is slow compared to the mechanical current source, but the operating frequency of PT is same as the switching frequency. In other words, the average state equation is only suitable for the slow system. As to the fast system, we focus on the fundamental harmonic component of each waveform because the energy is mainly transmitted by the resonance near the switching frequency. Since the average state equation cannot be used, the state equations of each period should be considered directly. Specifically, the state variable of interest is the PT output capacitor voltage, and the target is to know the fundamental harmonic component of the PT capacitor voltage v_{rec} . The PT capacitor voltage in the second period and fourth period are trivial in Figure 5-4 and the first

period and the third period have the symmetrical characteristic. Therefore, the state equation of the first period is only examined.

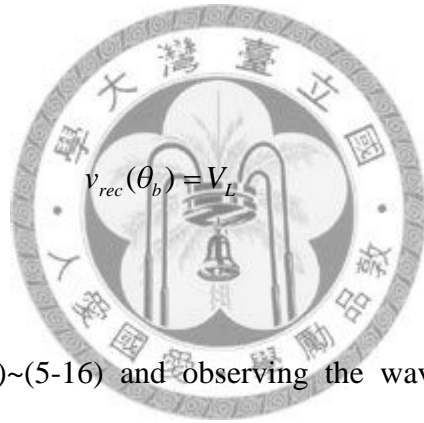
State equation of the 1st period:

$$\omega C_2 \frac{dv_{rec}(\theta)}{d\theta} = I_m \sin \theta \quad (5-14)$$

with initial condition

$$v_{rec}(0) = \begin{cases} 0 & \text{half wave rectifier} \\ -V_L & \text{full wave rectifier} \end{cases} \quad (5-15)$$

with final condition

$$v_{rec}(\theta_b) = V_L \quad (5-16)$$


Applying equations (5-14)~(5-16) and observing the waveforms in Figure 5-4, the analytical expression of the PT output capacitor voltage waveform can be obtained:

I. half wave rectifier:

$$\begin{aligned} v_{rec} = & \left(\frac{n_2 I_m}{\omega C_2} (1 - \cos \theta) \right) [H(\theta - \theta_b) - H(\theta)] + V_L [H(\theta - \pi) - H(\theta - \theta_b)] \\ & + \left(V_L - \frac{n_2 I_m}{\omega C_2} (1 - \cos \theta) \right) [H(\theta - (\pi + \theta_b)) - H(\theta - \pi)] \end{aligned} \quad (5-17)$$

II. *full wave rectifier:*

$$\begin{aligned}
v_{rec} = & \left(\frac{n_2 I_m}{\omega C_{out}} (1 - \cos \theta) - V_{Load} \right) [H(\theta - \theta_b) - H(\theta)] \\
& + V_L [H(\theta - \pi) - H(\theta - \theta_b)] \\
& + \left(\frac{-n_2 I_m}{\omega C_{out}} (1 + \cos \theta) + V_{Load} \right) [H(\theta - (\pi + \theta_b)) - H(\theta - \pi)] \\
& - V_L [H(\theta - 2\pi) - H(\theta - (\pi + \theta_b))]
\end{aligned} \tag{5-18}$$

Next, apply the Fourier analysis to both waveforms in equations (5-17) and (5-18) to find the first harmonic component:

$$v_{rec}^{fh} = I_m \kappa^s \sin \omega t + I_m \kappa^c \cos \omega t \tag{5-19}$$

where

$$\kappa^s = \frac{2n_2 R_L (1 + \cos \theta_b)}{\pi (\omega C_2 R_L + m\pi)} \tag{5-20}$$

$$\kappa^c = \frac{n_2 R_L \sin 2\theta_b - 2\theta_b}{\pi (\omega C_2 R_L + m\pi) (1 - \cos \theta_b)} \tag{5-21}$$

and where the superscript “*fh*” denotes the first harmonic component. It should be mentioned that the PT output capacitor voltage can be in terms of the mechanical current or load voltage, but in terms of the mechanical current is easier to describe the fast system in the following analysis. This fact implies the PT output capacitor is the key to connect the fast sub-system and the slow sub-system together.

5.1.4 State Equations of the Fast System

The equivalent circuit of the fast system is shown in the Figure 5-5 and the state equations can be written as follows:

$$\frac{di_1}{dt} = \frac{1}{L_1}(v_{in} - v_1) \quad (5-22)$$

$$\frac{dv_1}{dt} = \frac{1}{C_1}(i_1 - n_1 i_m) \quad (5-23)$$

$$\frac{dv_{C_m}}{dt} = \frac{i_m}{C_m} \quad (5-24)$$

$$\frac{di_m}{dt} = \frac{1}{L_m}(n_1 v_1 - n_2 v_{rec}^{fh} - i_m R_m - v_{C_m}) \quad (5-25)$$

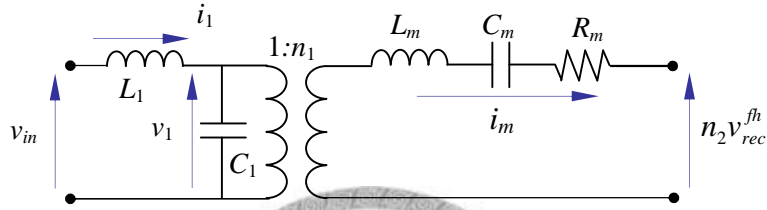


Figure 5-5. The equivalent circuit of the fast system

The method of harmonic balance is adopted. All the state variables are approximated as the single harmonic wave:

$$v_{in} = V_{in}^s \sin \omega t \quad (5-26)$$

$$i_1 = I_1^c \cos \omega t + I_1^s \sin \omega t \quad (5-27)$$

$$v_1 = V_1^c \cos \omega t + V_1^s \sin \omega t \quad (5-28)$$

$$i_m = I_m \sin(\omega t + \theta) = I_m^c \cos \omega t + I_m^s \sin \omega t \quad (5-29)$$

$$v_{C_m} = V_{C_m}^c \cos \omega t + V_{C_m}^s \sin \omega t \quad (5-30)$$

$$v_{rec}^{fh} = I_m \kappa^c \cos(\omega t + \theta) + I_m \kappa^s \sin(\omega t + \theta) \quad (5-31)$$

It should be noted that the phase angle θ of the mechanical current is introduced to show the phase difference between the input signal of the converter and the mechanical current. Thus, the first harmonic of the PT output capacitor voltage also has the phase

angle. Compared with the equation (5-29) and equation (5-31), the first harmonic of the

PT output capacitor voltage can be written without the phase angle θ :

$$v_{rec}^{th} = (I_m^c \kappa^s + I_m^s \kappa^c) \cos \omega t + (-I_m^c \kappa^c + I_m^s \kappa^s) \sin \omega t \quad (5-32)$$

To find the dynamics, the state variables in equations (5-26)~(5-30) are differentiated:

$$\frac{di_1}{dt} = \left(\frac{dI_1^c}{dt} + \omega I_1^s \right) \cos \omega t + \left(\frac{dI_1^s}{dt} - \omega I_1^c \right) \sin \omega t \quad (5-33)$$

$$\frac{dv_1}{dt} = \left(\frac{dV_1^c}{dt} + \omega V_1^s \right) \cos \omega t + \left(\frac{dV_1^s}{dt} - \omega V_1^c \right) \sin \omega t \quad (5-34)$$

$$\frac{di_m}{dt} = \left(\frac{dI_m^c}{dt} + \omega I_m^s \right) \cos \omega t + \left(\frac{dI_m^s}{dt} - \omega I_m^c \right) \sin \omega t \quad (5-35)$$

$$\frac{dv_{C_m}}{dt} = \left(\frac{dV_{C_m}^c}{dt} + \omega V_{C_m}^s \right) \cos \omega t + \left(\frac{dV_{C_m}^s}{dt} - \omega V_{C_m}^c \right) \sin \omega t \quad (5-36)$$

For half bridge input circuit,

$$V_m^s = \frac{2}{\pi} \sin(\pi d) \quad (5-37)$$

According to the concept of the harmonic balance, compared with equations

(5-22)~(5-25) and equations (5-32)~(5-37), the dynamic state equations can be

obtained:

$$\dot{\mathbf{x}} = \mathbf{A}\mathbf{x} + \mathbf{B}V_{dc} \quad (5-38)$$

where

$$\mathbf{x} = \left[I_{L_n}^c \quad I_{L_n}^s \quad V_{C_1}^c \quad V_{C_1}^s \quad I_m^c \quad I_m^s \quad V_{C_m}^c \quad V_{C_m}^s \right]^T \quad (5-39)$$

$$\mathbf{A} = \begin{bmatrix} 0 & -\omega & -\frac{1}{L_1} & 0 & 0 & 0 & 0 & 0 \\ \omega & 0 & 0 & -\frac{1}{L_1} & 0 & 0 & 0 & 0 \\ \frac{1}{C_1} & 0 & 0 & -\omega & -\frac{n_1}{C_1} & 0 & 0 & 0 \\ 0 & \frac{1}{C_1} & \omega & 0 & 0 & -\frac{n_1}{C_1} & 0 & 0 \\ 0 & 0 & \frac{n_1}{L_m} & 0 & \frac{-n_2\kappa^s - R_m}{L_m} & -\omega - \frac{n_2\kappa^c}{L_m} & -\frac{1}{L_m} & 0 \\ 0 & 0 & 0 & \frac{n_1}{L_m} & \omega + \frac{n_2\kappa^c}{L_m} & \frac{-n_2\kappa^s - R_m}{L_m} & 0 & -\frac{1}{L_m} \\ 0 & 0 & 0 & 0 & \frac{1}{C_m} & 0 & 0 & -\omega \\ 0 & 0 & 0 & 0 & 0 & \frac{1}{C_m} & \omega & 0 \end{bmatrix} \quad (5-40)$$

$$\mathbf{B} = \left[\frac{2}{\pi} \sin(\pi d) \quad 0 \right]^T \quad (5-41)$$

Under the steady state, the state variables do not change with time, i.e. $\dot{\mathbf{x}} = 0$. The state variable can be obtained by:

$$\mathbf{x} = -\mathbf{A}^{-1} \mathbf{B} V_{DC} \quad (5-42)$$

The mechanical current is:

$$I_m = \sqrt{I_m^c{}^2 + I_m^s{}^2} \quad (5-43)$$

Once the mechanical current is acquired, the characteristics of the slow system in the steady state condition can be known by Table 5-1. Add the small perturbation on equations (5-33)~(5-38) and linearized the equations. The small signal state equation of the fast system is derived:

$$\dot{\hat{\mathbf{x}}} = \mathbf{A} \hat{\mathbf{x}} + \mathbf{B} \hat{V}_{dc} + \mathbf{E} \hat{d} \quad (5-44)$$

And the output equation from equation (5-43) becomes:

$$\hat{I}_m = \mathbf{C}\hat{\mathbf{x}} \quad (5-45)$$

where

$$\mathbf{C} = \begin{bmatrix} 0 & 0 & 0 & 0 & \frac{I_m^c}{I_m} & \frac{I_m^s}{I_m} & 0 & 0 \end{bmatrix} \quad (5-46)$$

So far, both steady state model and the small signal model were fully obtained. The completed block diagrams of the models are shown in Figure 5-6.

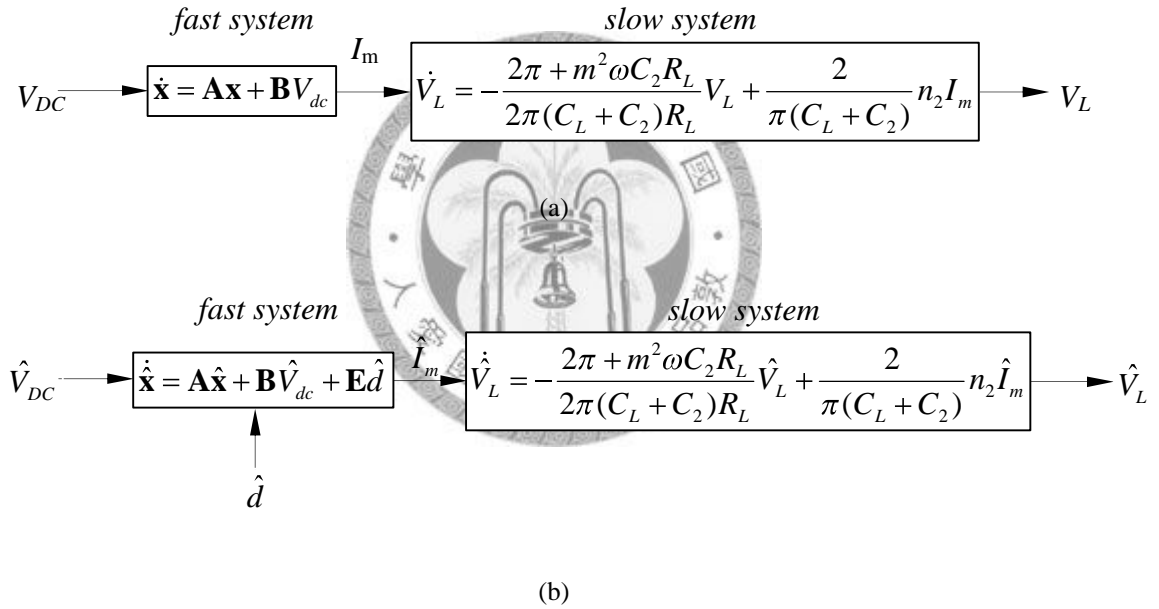
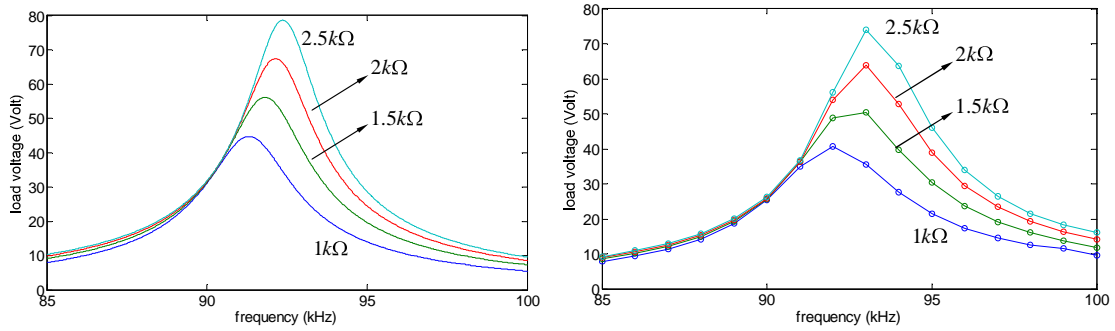


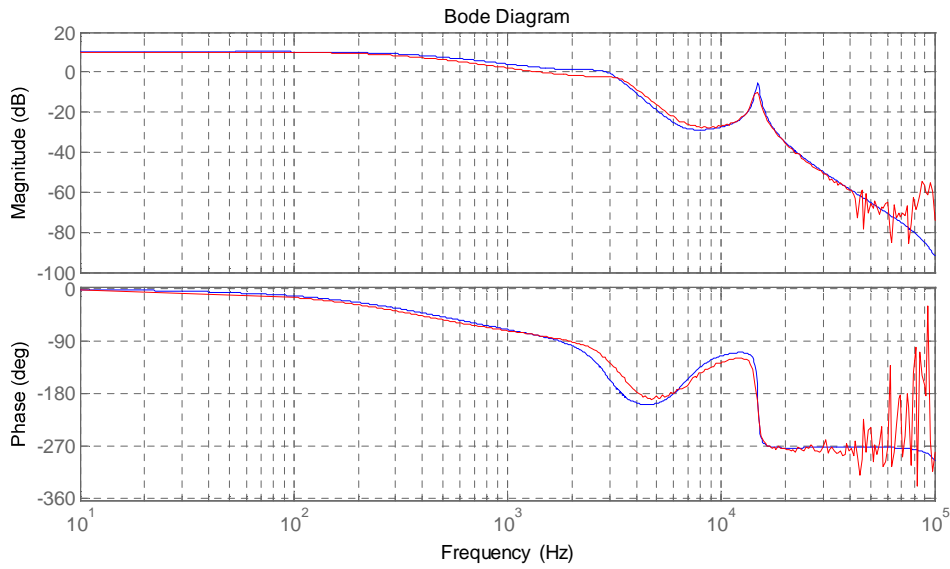
Figure 5-6. The block diagram of the converter (a) large signal dynamic model (b) small signal dynamic model

The simulation software PSIM was used to verify the theoretical model. All components are set as the example where $[L_1 C_1 n_1 L_m C_m R_m n_2 C_2 C_f] = [600\mu\text{H} 4\text{nF} 1 30\text{mH} 100\text{pF} 10\Omega 4 30\text{nF} 10\mu\text{F}]$. In addition input voltage, duty ratio, operating frequency and load resistor are set at 20Volt, 0.4, 50Ω respectively. Both the steady state

model and the small signal model of PT based DC/DC converter (with full bridge rectifier) are shown in Figure 5-7.



(a)



(b)

Figure 5-7. The block diagram of the converter

(a) large signal dynamic model including theoretical prediction (left figure) and experimental prediction

(right figure) (b) small signal dynamic model including simulation (red line) and theoretical prediction

(blue line)

5.1.5 Selection of the PT fed rectifiers

So far, two PT fed rectifier has already analyzed. It is interesting to know which rectifier better is better. First, consider the case that two equal PTs with equal mechanical currents are connected to the full-wave and the half-wave rectifiers respectively. Equal mechanical currents and PTs implies the mechanical losses, i.e. $(1/2)I_m^2 R_m$, in the PTs are equal. According to Table 5-1, the relationship between the load voltage and the mechanical current are:

$$V_L^f = \frac{2n_2 R_L^f}{2\omega C_2 R_L^h + \pi} I_m \quad (\text{full-wave rectifier}) \quad (5-47)$$

$$V_L^h = \frac{2n_2 R_L}{\omega C_2 R_L + 2\pi} I_m \quad (\text{half-wave rectifier}) \quad (5-48)$$

where the superscripts “*f*” and “*h*” here represent the full-wave rectifier and the half-wave rectifier respectively. The required load resistance can be derived as follows:

$$R_L^f = \frac{\pi V_L^f}{2n_2 I_m - 2\omega C_2 V_L^f} I_m \quad (\text{full-wave rectifier}) \quad (5-49)$$

$$R_L^h = \frac{2\pi V_L^h}{2n_2 I_m - \omega C_2 V_L^h} I_m \quad (\text{half-wave rectifier}) \quad (5-50)$$

When the load voltage and the mechanical current are equal, the load resistance of the half-wave rectifier is smaller than the load value of the full-wave rectifier. Accordingly, the received load power (V_L^2/R_L) of the full-wave rectifier is larger than the load power of the half-wave rectifier in this case. Since the main losses are equal, the full-wave rectifier can obtain better efficiency than the half-wave rectifier. In fact, the underlying reason is that the full-wave rectifier transfers power to the load in both 2nd period and

4th period, but the half-wave rectifier only transfers the power to the load in 2nd period.

Secondly, consider the case that the load voltage and the load current are both equal. Specifically, we fixed the load specifications but connecting different rectifiers to the PT. Since the rectified current of the half-wave rectifier only flow to the load in the 2nd period, the rectified current i_{rec} in the half-wave rectifier should be larger than it in the full-wave rectifier to get enough load current. To get larger load current, the mechanical current should be larger or the mechanical-electrical ratio n_2 should be larger. However, larger mechanical current leads the larger loss, and the larger n_2 value leads larger size of the PT. In this discussion, the full-wave rectifier is still the better choice. It should be mentioned that it seems that the full-wave rectifier have double diode voltage drops, but there is roughly half rectified current in the full-wave rectifier which cancels the effect of the voltage drops. Specifically, the losses in the two rectifiers are similar.

In brief summary, the half-wave rectifier only has half amount of the diodes, but the connected half-wave rectifier leads the larger size of the PT or smaller delivered power. The discussion shows that the topology of the power stage can influence the size of PT. More specifically, the full-wave rectifier decreases the size of PT but do not sacrifice the efficiency of the converter. Therefore, we adopted the full-wave rectifier to make a DC/DC converter in the following section.

5.2 Design of Piezoelectric Transformer based DC/DC converter

5.2.1 The relationship between the PT fed rectifier and the mechanical current

In previous section, we neglected the effect of the diode drops. However, to understand the losses in the PT fed rectifier more clearly, the voltage drop V_D is considered in this section. Figure 5-8 redraw the waveforms of the PT fed full-wave rectifier with the voltage drops.

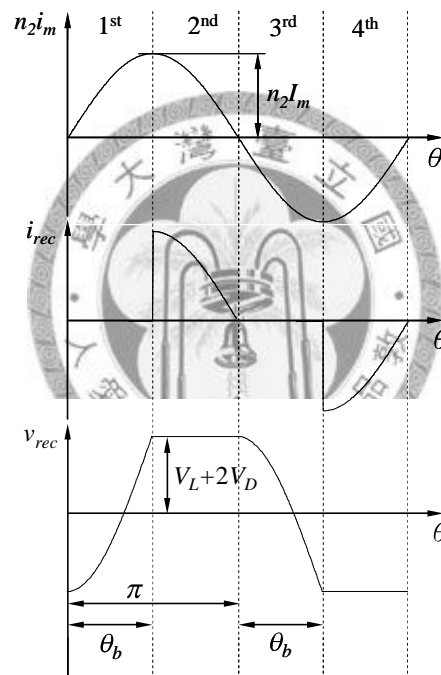


Figure 5-8. Voltage and current waveforms of the PT fed full-wave rectifier

The analysis of this waveform is similar as mentioned above. In the first period $\theta \in [0, \theta_b]$ and third period $\theta \in [\pi, \pi + \theta_b]$, the diode was blocked and thus there was no current flowing to the load. The PT output capacitor was being charged and discharged in the first and third period respectively. Therefore,

$$\frac{1}{\omega C_2} \int_0^{\theta_b} n_2 I_m \sin \theta d\theta = 2(V_L + 2V_D) \quad (5-51)$$

In the second period $\theta \in [\theta_b, \pi]$ and fourth period $\theta \in [\pi + \theta_b, 2\pi]$, diodes are conducted and the rectifier voltage equals to the sum of the load voltage and the diode voltage drops. In addition, the load current I_o is the average current of the rectifier current. Therefore, the load current can be derived:

$$\frac{V_L}{R_L} = I_o = \frac{1}{\pi} \int_{\theta_b}^{\pi} n_2 I_m \sin \theta d\theta \quad (5-52)$$

Combining Eqs. (5-51) and (5-52), the relationship between load voltage and the mechanical current can be seen as follows:

$$V_L = \frac{2R_L}{\pi + 2\omega C_2 R_L} (n_2 I_m - 2\omega C_2 V_D) \quad (5-53)$$

Furthermore, the efficiency of the converter is:

$$\eta = \frac{P_L}{P_{PTloss} + P_D + P_L} \quad (5-54)$$

where P_{PTloss} and P_D represent the loss in the piezoelectric transformer and in the rectifier respectively, and P_L represents the load power.

$$P_{PTloss} = \frac{1}{2} I_m^2 R_m \quad (5-55)$$

$$P_D = 2V_D \frac{V_L}{R_L} \quad (5-56)$$

$$P_L = \frac{V_L^2}{R_L} \quad (5-57)$$

In equations (5-54)~(5-57), the efficiency varied with the load impedance, which implies that an optimally efficient loading condition exists. The optimal loading

condition occurred at $d\eta/dR_L = 0$, which was mentioned in equation (5-8). The optimal loading condition is repeated as follows:

$$R_L^* = \frac{\pi}{2\omega C_2} \quad (5-58)$$

In actuality, equation (5-58) is the condition when the load voltage varies with the load impedance but does not get regulated since the voltage is not constant. However, in practice, a DC/DC converter requires voltage regulation. In our paper, our objective was to obtain the case where there is a constant load voltage. Assuming that the load voltage is constant and applying the condition $d\eta/dR_L = 0$ to equations (5-54)~(5-57), the optimal loading condition can then be changed as follows:

$$\frac{1}{2} I_m^2 R_m = 0 \quad (5-59)$$

Equation (9) is a trivial equation as it only occurs at the condition where there is no current passing through the piezoelectric transformer or when the piezoelectric transformer is at an ideal condition without any presence of resistive loss (damping).

In fact, the left hand side of equation (5-59) represents the loss in the piezoelectric transformer. More specifically, since equation (5-59) shows no loss from the piezoelectric transformer, therefore we can assume maximum efficiency has taken place.

Since mechanical resistance is mainly a factor of the material properties, the magnitude of the mechanical current is the key to efficiency but not to the optimal loading condition in equation (5-58). This result is simple but significant as most previous

research has only mentioned that the optimal loading variable is the key design factor of a piezoelectric transformer. The above analysis clearly states that this is not correct in cases when voltage regulation needs to be taken into account.

It was known the mechanical current of the piezoelectric transformer is an important design factor. However, it does not correlate well with the optimal loading condition in the previous section and with previous research works. Considering the case where the load power is the same, a smaller mechanical current leads to better efficiency. Furthermore, some previous research works have stated that vibration velocity is the physical limitation of piezoelectric materials experimentally but they do not mention it at all when looking at PT designs. If the PT vibration velocity is too large, piezoelectric transformers will generate heat gradually which can lead to an eventual piezoelectric transformer breakdown. The piezoelectric transformer of equal size can only dissipate limited, fixed power (i.e. $P_{PTloss} = const.$) and where the power loss in the piezoelectric transformer is strongly dependent on the vibration velocity and the material property. In fact, the vibration velocity is analogous to the mechanical current, and the power loss in the piezoelectric transformer follows the square of the mechanical current in equation (5-55). More specifically, the vibration velocity is in fact the most important physical quantity for the piezoelectric transformer in steady

state applications. The analysis of the mechanical current also implies that vibration velocity should be taken into consideration when looking at a PT design.

In general, the required mechanical current in the converter is determined by the load characteristics. According to the relationship between mechanical current and load voltage in equation (5-3), the mechanical current can be represented as:

$$I_m = \frac{\pi + 2\omega C_2 R_L}{2n_2 R_L} V_L + \frac{2\omega C_2}{n_2} V_D < I_{m,\max} \quad (5-60)$$

In practice, the load impedance is always varied and undetermined. Therefore, it is not easy to analyze the mechanical current systematically in equation (5-60). However, the optimal loading condition in equation (5-58) can provide a good reference for load values. Considering the case where the optimal loading condition is set to match α times of the minimum load value $R_{L,\min}$ (heaviest loading condition) of the specification, we can obtain

$$\alpha R_{L,\min} = \frac{\pi}{2\omega C_2} \quad (5-61)$$

Substituting equation (5-61) into equation (5-60) and applying Ohm's Law yields:

$$I_m = \frac{\pi}{2n_2} \left(\frac{1}{R_L} + \frac{1}{\alpha R_{L,\min}} \right) V_L + \frac{\pi}{n_2 \alpha R_{L,\min}} V_D \quad (5-62)$$

Equation (5-62) shows that the load voltage and diode voltage drop both contribute to the mechanical current. When we consider that the load voltage is fixed and the diode voltage drop is zero, we have the following:

$$I_m = \frac{\pi}{2n_2} \left(\frac{1}{R_L} + \frac{1}{\alpha R_{L,\min}} \right) V_L \quad (5-63)$$

Here, we fixed the coupling ratio n_2 to discuss the α values. Assuming $n_2 = 5$ and the load voltage and load value follow the targeted specifications of this paper (i.e. $V_L = 15\text{ V}$ and $R_{L,\min} = 22.5\Omega$), the mechanical current and efficiency can be plotted as a function of the load value in Figure 5-9 using equations (5-54) and (5-63). Figure 5-9 shows the case when at constant load voltage, three different lines which not only indicate different α values but also implies three different impedance values of the piezoelectric transformer output capacitors (i.e., $1/\omega C_2$). More specifically, three different lines represent three different piezoelectric transformers which meet the same load specifications. Clearly, a larger α value leads to better efficiency and a smaller mechanical current at the same load value. It should be noted that the circular points in Figure 5-9(b) represent the location of the typical optimal loading condition. Results show that approaching the optimal loading condition does not lead to better efficiency, however, each typical optimal loading condition represents the local maximum efficiency for each line with respect to the same piezoelectric transformer. In fact, the most efficient condition is at $\alpha \rightarrow \infty$ since it leads to a minimum mechanical current in equation (5-63). This condition, i.e., $\alpha \rightarrow \infty$, is far from the typical optimal loading condition.

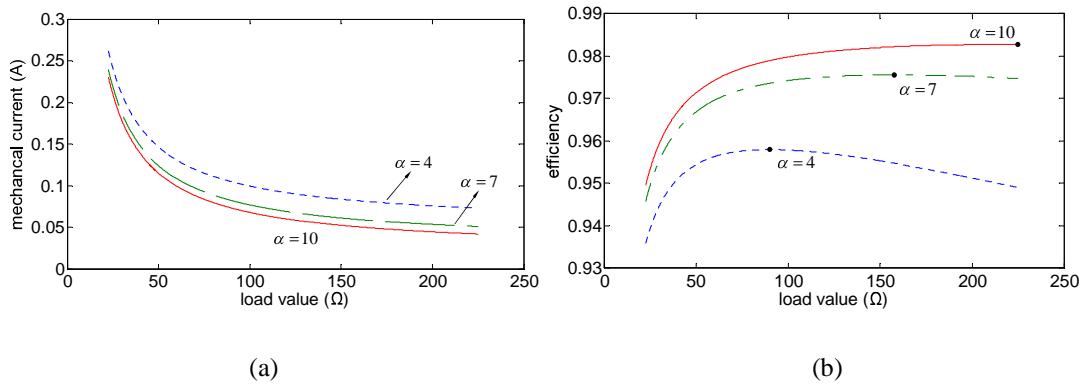


Figure 5-9. (a) Mechanical current and (b) efficiency with load variations when the diode voltage drop is neglected.

We next considered the case where the mechanical current is the result of the diode voltage drops but which neglects the contribution from a load voltage. Therefore, equation (5-62) can be rewritten as:

$$I_m = \frac{\pi}{n_2 \alpha R_{L,\min}} V_D \quad (5-64)$$

Assuming $V_D = 0.3\text{ V}$ and applying equations (5-54) and (5-63) the mechanical current and the efficiency can be plotted. (see Figure 5-10)

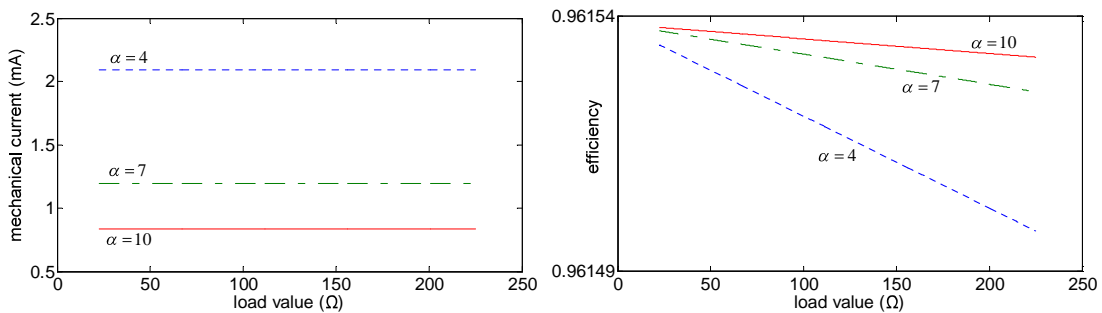


Figure 5-10. (a) Mechanical current and (b) efficiency with load variations when the contribution of the load voltage is neglected.

It should be noted that Figure 5-9 and Figure 5-10 show the same trend, that is, a larger α value leads to better efficiency and a smaller mechanical current. Compared with a contribution from the load voltage and from the diode voltage drops in Figure 5-9 and Figure 5-10 respectively, the mechanical current from the diode voltage drops can be neglected but the efficiency cannot be neglected. This implies that the diode voltage drops can be neglected in the analysis of the mechanical current but cannot be neglected in the analysis of efficiency. On the other hand, efficiency of the rectifier from the diode voltage drops in Figure 5-10 (b) is almost a constant value. In other words, the diode voltage drops can be viewed as a contribution of the constant efficiency and is not significantly related to the PT design.

In fact, increasing the n_2 value is the most effective way to increase the efficiency since the required mechanical current would decrease significantly (see equation (5-62)). Furthermore, changing the α value changes the location of the local maximum efficiency as it relates to the typical optimal loading condition. Different from the α value, increasing n_2 value does not change the location of the local maximum efficiency. Figure 5-11 shows the curve of efficiency with different n_2 values. Although α value and n_2 value should both be optimally set to be as large as possible, these two values cannot be infinite and the limitation is that it is difficult to

have them both increase at the same time. This is due to the constraint of the PT configuration, which is detailed in the following section.

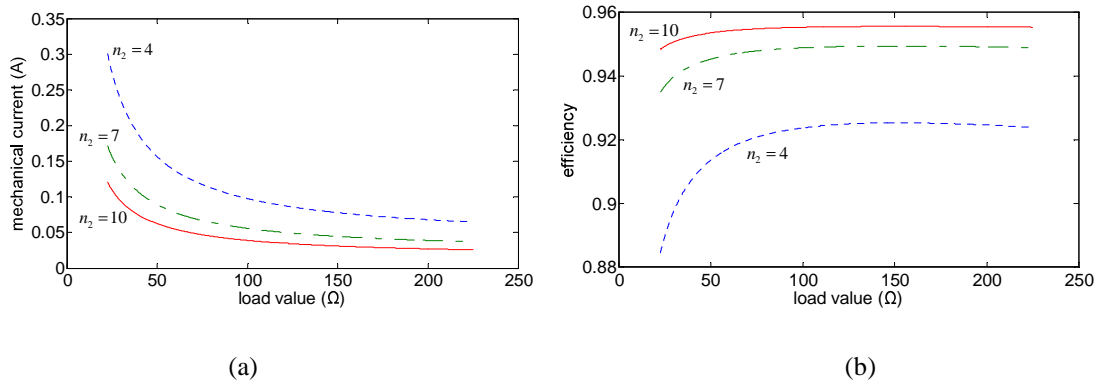
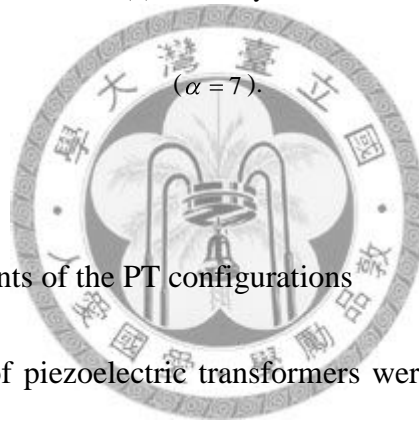


Figure 5-11. (a) Mechanical current and (b) efficiency with load variations when α value is fixed



5.2.2 Dimensional constraints of the PT configurations

Many different types of piezoelectric transformers were modeled by an equivalent circuit method. However, the relationship between an equivalent circuit and the dimensional parameters of a piezoelectric transformer is not a one to one mapping [30, 31, 32]. Different equivalent electrical components may be combined to share a single dimensional parameter, which prevent the electrical equivalent components from being designed independently. For example, the capacitance of the piezoelectric transformer is related to both the effective electrode area and the thickness. Considering the uniformly-poled longitudinal PT in Figure 5-12(a), the input capacitance and output capacitance are both determined by the thickness of the piezoelectric transformer. On

the other hand, the parameters of the PT configuration have their own manufacturing constraints. For example, the number of the layers should be an integer. In addition, all physical quantities cannot be arbitrary large and in most cases need to be prescribed at a specific value. In summary, the value of an equivalent electric component cannot be designed without looking into the dimensional parameters. If we design the electric components first, there may not be a corresponding piezoelectric transformer. In our research, we propose that designing the dimensional parameters directly is the better approach.

There are three basic piezoelectric transformer configurations which can be used to explain the dimensional constraints of PT configurations: uniformly-poled longitudinal PT, uniformly-poled disk-type PT, and stacked disk-type PT (see Figure 5-12). A comparison of these different types PTs shows that an uniformly-poled longitudinal PT is the worst possible choice. A uniformly-poled longitudinal PT works on a longitudinal vibration mode. Since only one of the two possible vibrational directions is used and the piezoelectric transformer structure is not as symmetric as that of the disk-type PT, the uniformly-poled longitudinal PT has a poorer electromechanical coupling and more spurious vibration modes than the disk-type piezoelectric transformer. In addition, the input portion and the output portion of an uniformly-poled longitudinal PT shares the same thickness and even the same width.



When the thickness of the piezoelectric transformer changes, the input portion and the output portion also change together. For the uniformly-poled disk-type PT, the input portion and the output portion also share the same thickness. In addition, in practice, the number of input layers and the number of output layers are difficult to separate although it is technically possible [33]. These problems do not occur in the stacked disk-type PT as the input portion is separated from the output portion. In addition, the stacked disk-type PT possesses high electromechanical coupling and is symmetric vibration with respect to the radial direction. The stacked disk-type PT can thus be an appropriate choice for a variety of applications. For this reason, we adopted a stacked disk-type PT configuration in this paper.

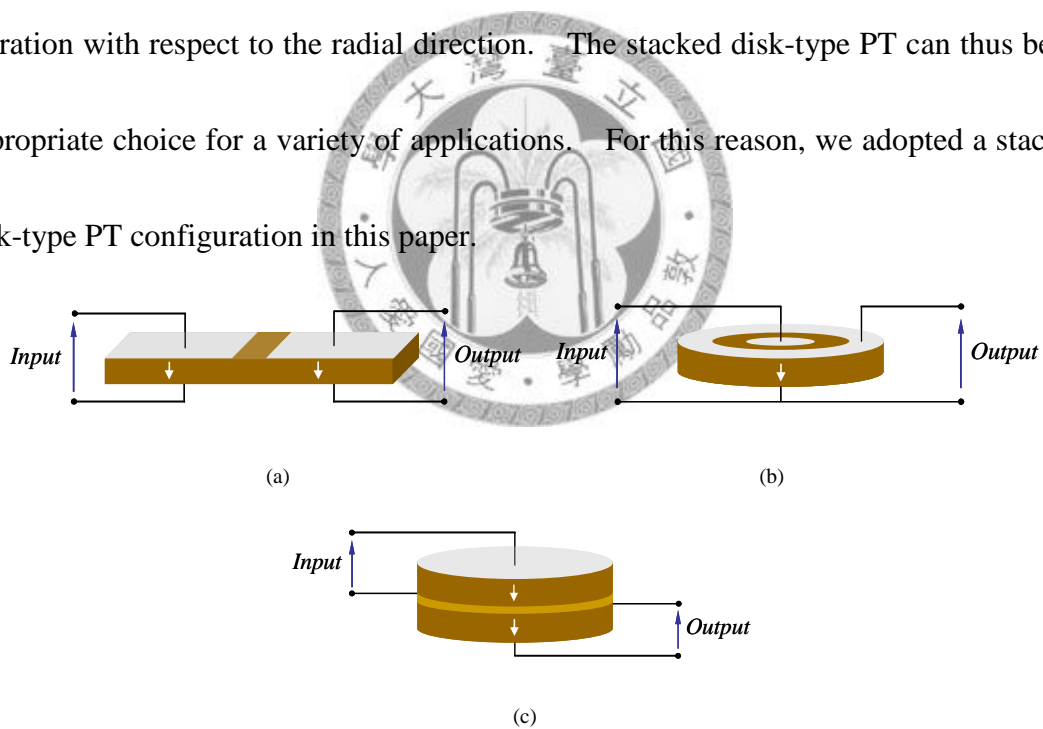


Figure 5-12. (a) uniformly-poled longitudinal PT, (b) uniformly-poled disk-type PT, (c) stacked disk-type PT

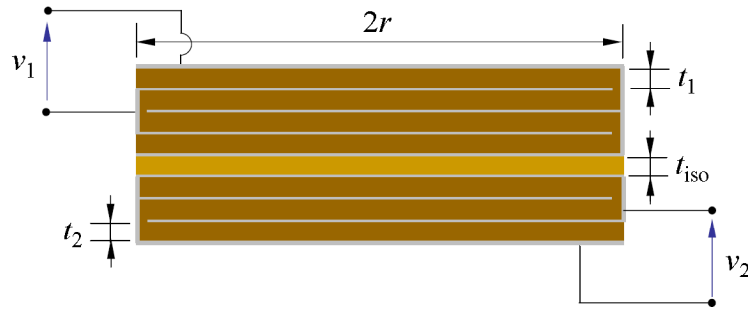


Figure 5-13. side view of the stacked disk-type PT

The detail side view and dimensional parameters of the stacked disk-type PT are shown in Figure 5-13, where r is the radius and t_1 , t_2 , t_{iso} are the thickness of each input layer, output layer and isolation layer respectively; m_1 , m_2 and m_{iso} are the number of input layers, the number of output layers and the number of isolation layers respectively. In Figure 5-13, for example, m_1 , m_2 and m_{iso} are equal to 4, 3 and 1 respectively. Table 5-2 shows the relationship between a stacked disk-type PT and an equivalent circuit. Applying equation (5-61) and Table 5-2, the α value and n_2 values can be obtained by the following:

$$\alpha = \frac{t_2}{m_2 r^2} \frac{1}{2\omega_r \epsilon_{33}^S R_{L,\min}} \quad (5-65)$$

$$n_2 = m_2 r \frac{2\sqrt{2}\pi d_{31}}{s_{11}^E (1-\nu^2)} \quad (5-66)$$

Furthermore, substituting equations (5-65) and (5-66) into equation (5-63) and neglecting the diode voltage drops, the mechanical current can be obtained as:

$$I_{m,\max}(m_2) = \frac{A_m}{m_2} + \frac{A_t}{t_2} \quad (5-67)$$

where

$$A_m = \frac{s_{11}^E(1-\nu^2)V_L}{4\sqrt{2}d_{31}rR_L} \quad (5-68)$$

$$A_t = \frac{s_{11}^E \varepsilon_{33}^S(1-\nu^2)\omega_r r V_L}{2\sqrt{2}d_{31}} \quad (5-69)$$

Equation (5-67) is the governing equation of the PT output section. It should be noted that the radius usually determined by the operating frequency of the converter. The thickness and the number of layers are the parameters of interest. Equation (5-67) is interesting as it implies that the number of layers and the thickness influence the magnitude of the mechanical current independently. If the number of layers and the thickness are larger, the mechanical current would be smaller, and the PT becomes more efficient. In such a case, however, the size of PT may be too large. Therefore, it is interesting to find the PT of smaller size in the same mechanical current condition. It should be noted that the dimensional parameters of equation (5-67) only describe the output section. However, the real size of the PT includes not only the output section but also the input section. Therefore, the input section will be discussed in the following section.

Table 5-2. The relationship between the dimensional parameter and the equivalent circuit of the stacked

disk-type PT

ω_r	L_m	C_m	R_m	C_1	C_2	n_1	n_2
$\frac{\pi N_p}{r}$	$\frac{\rho_m \pi r^2 \beta}{2}$	$\frac{1}{L_m \omega_r^2}$	$\frac{1}{Q_m} \sqrt{\frac{L_m}{C_m}}$	$\frac{m_1 \pi r^2 \epsilon_{33}^S}{t_1}$	$\frac{m_2 \pi r^2 \epsilon_{33}^S}{t_2}$	$\frac{2\sqrt{2}\pi r d_{31} m_1}{s_{11}^E (1-\nu^2)}$	$\frac{2\sqrt{2}\pi r d_{31} m_2}{s_{11}^E (1-\nu^2)}$
<p><u>PT parameters:</u></p> <p>ω_r is the natural frequency of the PT (rad/s)</p> <p>r is the radius of the PT</p> <p>m_1 and m_2 are the number of input layers and the number of output layers respectively</p> <p>β is the total thickness of the PT, where $\beta = m_1 t_1 + m_2 t_2 + m_{iso} t_{iso}$</p>							
<p><u>Material properties (PZT-QA, ELECERAM TECHNOLOGY Co., LTD.):</u></p> <p>$N_p = 2200$ is the frequency constants of the plane vibration (kHz•mm)</p> <p>$\rho_m = 7950$ is the density (kg/m³)</p> <p>$\nu = 0.16$ is the Poisson's ratio</p> <p>$Q_m = 1313$ is the mechanical quality factor</p> <p>$\epsilon_{33}^S = 1420 * 8.854 * 10^{-12}$ is the permittivity at constant strain condition, i.e. constant S (F/m)</p> <p>$d_{31} = 232 * 10^{-12}$ are the piezoelectric constants (m/V)</p> <p>$s_{11}^E = 1.14 * 10^{-11}$ is the compliance constant under the constant electric field, i.e. constant E</p>							

5.2.3 Energy Balance

It should be noted that the input section must transfer enough power to the output section of the piezoelectric transformer. For simplicity, the concept of a harmonic balance which has widely used in the modeling of the resonant power converter was adopted here. The fundamental harmonics of the input voltage and the rectifier voltage are only of interest as the mechanical current can be viewed as a pure sinusoidal. To examine the energy balance, therefore, the input voltage of the piezoelectric transformer has been assumed to be a sinusoidal source, that is:

$$v_1 = V_1^s \sin \omega t + V_1^c \cos \omega t \quad (5-70)$$

where

$$V_1^s = V_1 \cos \theta_{in} \quad (5-71)$$

$$V_1^c = V_1 \sin \theta_{in} \quad (5-72)$$

and θ_{in} is the phase angle between input voltage and the mechanical current.

Moreover, the input power should be larger than the sum of the power dissipation and the load power, so:

$$\frac{1}{2} n_1 V_1 I_m \cos \theta_{in} \geq \frac{1}{2} I_m^2 R_m + \frac{2V_D V_L}{R_L} + P_L \quad (5-73)$$

However, equation (5-73) cannot be solved as the coupling factor n_1 and the phase angle θ_{in} are both unknown variables here. More relationship is required to solve

equation (5-73). In addition to energy balance, the mechanical current is an important

parameter to connect input terminal and output terminal. Moreover, the mechanical current is determined from the input voltage and the output voltage of the piezoelectric transformer. The input voltage of the PT is shown in equation (5-70) and output voltage waveform of the PT is shown in Figure 5-8. Due to the fact that the mechanical current is a pure sinusoidal $i_m = I_m \sin \theta$, only the fundamental harmonic of the waveform is of primary interest. The first harmonic component of the output voltage of the piezoelectric transformer v_{rec} in Figure 5-8 can be identified by Fourier analysis:

$$v_{rec} = V_{rec}^s \sin \theta + V_{rec}^c \cos \theta \quad (5-74)$$

where

$$V_{rec}^s = \frac{2(1 + \cos \theta_b)}{\pi} V_L \quad (5-75)$$

$$V_{rec}^c = \frac{\sin \theta_b - 2\theta_b}{\pi(1 - \cos \theta_b)} V_L \quad (5-76)$$

where θ_b is the diode blocked angle mentioned in equation (5-51). Combining equations (5-51) & (5-53) and neglecting diode voltage drops, the closed form of the diode blocked angle can be written as:

$$\theta_b = \cos^{-1} \left(\frac{\pi - 2\omega C_2 R_L}{\pi + 2\omega C_2 R_L} \right) \quad (5-77)$$

Furthermore, the impedance phase θ_m of the mechanical branch can introduce another relationship between the input terminal and output terminal, such as:

$$\frac{n_1 V_1^c - n_2 V_{rec}^c}{n_1 V_1^s - n_2 V_{rec}^s} = \tan \theta_m = Q \left(\frac{\omega^2}{\omega_r^2} - 1 \right) \quad (5-78)$$

To obtain the solution easily, the relationship which equates input real power to the real output power is used, such as:

$$n_1 V_1^s I_m = \frac{1}{2} I_m^2 R_m + n_2 V_2^s I_m \quad (5-79)$$

Combining equations (5-71)~(5-79), the energy balance relationship can be rewritten as follows:

$$(n_1 V_1)^2 \geq \left(\frac{1}{2} I_m R_m \tan \theta_m + n_2 V_{rec}^c \right)^2 + \left(I_m R_m + \frac{4V_D V_L}{I_m R_L} + \frac{2P_L}{I_m} \right)^2 \quad (5-80)$$

Equation (5-80) is the governing equation of the PT input section. However, equation (5-80) is too complex to be used to examine the design constraints and the physical meaning of the dimensional parameters intuitively. To simplify equation (5-80), the piezoelectric transformer is assumed to be very efficient such that all the loss can be neglected. Moreover, applying the dimensional parameter in Table 5-2, equation (5-80) can be rewritten as:

$$(m_1 V_1)^2 \geq (m_2 V_{rec}^c)^2 - \left(\frac{s_{11}^E (1 - \nu^2)}{2\sqrt{2}\pi r d_{31}} P_L \right)^2 \quad (5-81)$$

There are several relationships which exist between the dimensional parameters. First, the minimum number of input layers increases with the number of output layers. This implies that the input section and the output section cannot be designed separately if a small size piezoelectric transformer is preferred. Secondly, the thickness of the

piezoelectric transformer input section as introduced in equation (5-81) means that it is not a significant parameter for the specifications.

5.2.4 Experimental Model Correction

According to our analysis in the last section, we now have enough information to design the piezoelectric transformer. However, the model should make the correction experimentally. The reason is that the large number of layers may cause the quality factor (Q_m value) of the piezoelectric transformer to decrease especially when the layers are manufactured using a glue process. The allowable passing current through the mechanical R_m - L_m - C_m branch thus becomes smaller. More specifically, the maximum mechanical current and the quality factor of the PT are a function of the total number of layers, where

$$Q_m = Q_0(m) \quad (5-82)$$

$$I_{m,\max} = I_{0,\max}(m) \quad (5-83)$$

where Q_0 and $I_{0,\max}$ represent the quality factor and the maximum mechanical current in the single piezoelectric layer respectively, and m is the total number of the layers. The total number of the layers includes three parts: the input layers, the output layers and the isolation layers, i.e.

$$m = m_1 + m_2 + m_{iso} \quad (5-84)$$

The relationship between the numbers of the layers should be obtained experimentally. Several piezoelectric layers (radius=12.5mm, thickness=0.69mm) were glued together by high heat-resistant epoxy resin to serve as the specimen to obtain the experimental model. First, the equivalent circuit and the quality factor of each piezoelectric transformer were measured by an impedance analyzer (Agilent 4294A). The maximum output short current, $n_2 i_m$, (see Figure 5-14) was measured by increasing the input voltage of the piezoelectric transformer. The maximum output short current can be defined by the operating point where the piezoelectric transformer begins to generate heat unstably. The starting point of the unstable heat generation occurs approximately when the temperature rises by 35~45°C (room temperature is 25°C). Finally, the mechanical currents can be calculated by applying the equivalent circuit model to the output short current.

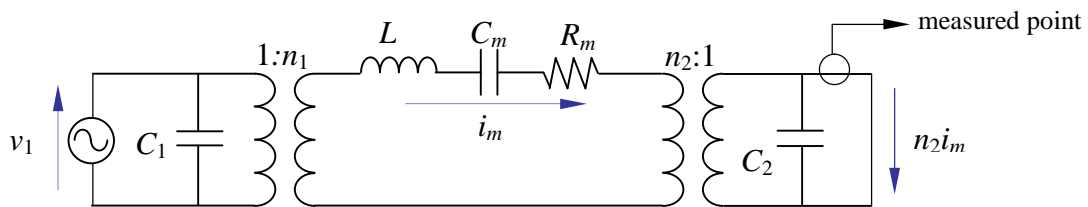


Figure 5-14. Measurement of the mechanical current

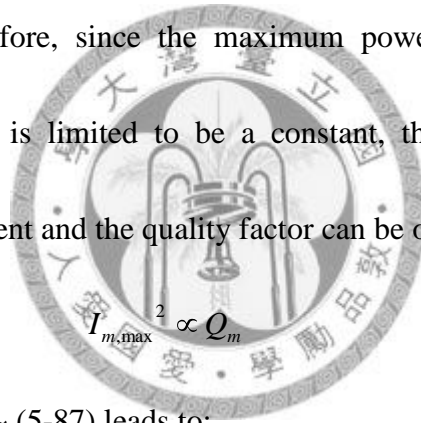
The measured quality factors and the mechanical currents are shown in Figure 5-15(a) and Figure 5-15(b) respectively. Both the quality factors and the mechanical currents

can be described as the exponential function of the number of layers by a curve fitting method:

$$Q_m = Q_0 e^{-a(m-1)} \quad (5-85)$$

$$I_{m,\max} = I_{0,\max} e^{-b(m-1)} \quad (5-86)$$

where a and b represent the exponential decay rate of the quality factor and the maximum mechanical current respectively, which are decided by the manufacturing process, the gluing material and gluing thickness. In our specimens, $a = 0.141$ and $b = 0.063$. As mentioned before, since the maximum power loss in the piezoelectric transformer of equal size is limited to be a constant, the relationship between the maximum mechanical current and the quality factor can be obtained:



$$I_{m,\max}^2 \propto Q_m \quad (5-87)$$

Applying equations (5-85)~ (5-87) leads to:

$$a = 2b \quad (5-88)$$

The experimental result ($a/b = 2.2$) follows equation (5-88) roughly, which verified the concept of the constant power loss capability of the piezoelectric transformer. This also implies that we can use the exponential decay rate of quality factor to estimate that of the mechanical current. This is useful information since the quality factor is much easier to measure than the maximum mechanical current. On the other hand, the relationship between the mechanical current actually is related to the number of the

gluing interfaces (i.e. $m-1$) but not the number of layers. Thus, the interface of the glue is the key factor towards decreasing the maximum mechanical current.

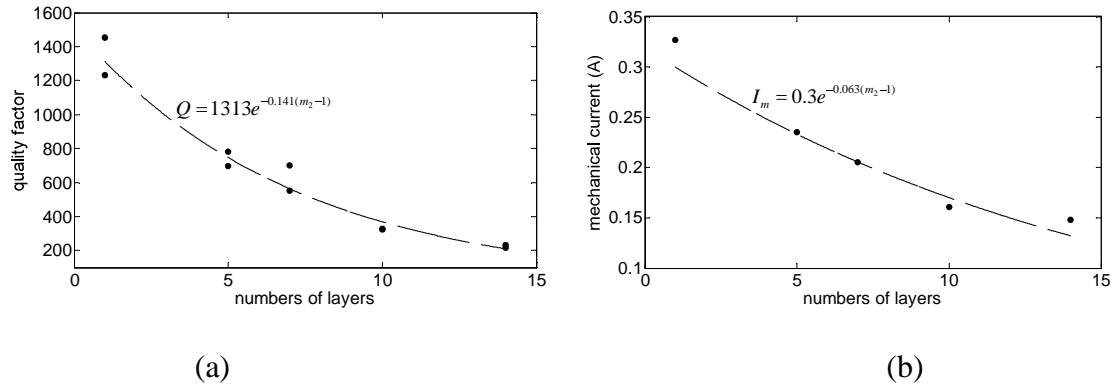
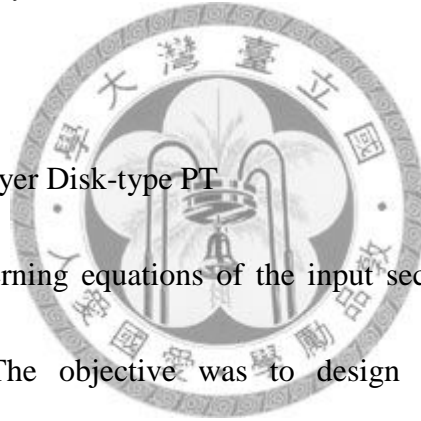


Figure 5-15. (a) quality factor and (b) mechanical current versus numbers of layers



5.2.5 Design of the Multilayer Disk-type PT

So far, both the governing equations of the input section and the output section have been disclosed. The objective was to design a small size piezoelectric transformer with high efficiency and enough regulation ability. The volume of the piezoelectric transformer equals:

$$Vol = \pi r^2 (m_1 t_1 + m_2 t_2 + m_{iso} t_{iso}) \quad (5-89)$$

However, the minimum value of equation (5-89) is difficult to solve with governing equations equations (5-67) and(5-80). In equation (5-89), the radius and the isolation layers are not the parameters of interest since radius is related to the operating frequency and the isolation layers do not influence the power transformation significantly. In addition, the thickness of the input layers is also not important for the power

transformation as mentioned in equation (5-81). In other words, the importance to design is the output section, the input section and the isolation layers in the sequence. Therefore, to simplify the design procedure, the output section should be obtained first and then followed by obtaining the input section and the isolation layers. On the other hand, equation (5-81) provides the information that m_1 has a positive relationship with m_2 , which means that the number of input layers and the number of output layers should increase simultaneously for power conservation. This implies that the number of output layers is more important than the thickness in the output section. To describe this, the objective function T can be set to:

$$T = m_2^2 t_2 \quad (5-90)$$

Equation (5-67) is the constraint of the output section. To find the minimum value of the objective function, a Lagrange multiplier λ was introduced and the optimization was solved by the regular Lagrange multiplier method as follows:

$$X = m_2^2 t_2 - \lambda [m_2 t_2 I_{m, \max} - t_2 A_m - m_2 A_t] \quad (5-91)$$

$$\frac{\partial X}{\partial m_2} = \frac{\partial X}{\partial t_2} = \frac{\partial X}{\partial \lambda} = 0 \quad (5-92)$$

Combining equations (5-86), (5-91) and (5-92), the optimized equation of the output section can be obtained:

$$b I_{m, \max} m_2^2 e^{-b(m-1)} + 2 I_{m, \max} m_2 e^{-b(m-1)} - 3 A_m = 0 \quad (5-93)$$

Equation (5-93) appears to be still coupled with the input section and the isolation layer.

Since the minimum number of layers is a value of 1, we set the number of input layers

and the number of isolation layers to be both equal to a value of 1 initially, i.e.

$m = m_2 + 1$. We then solved equation (5-93) to obtain the number of output layers.

The thickness of the output section was then solved using equation (5-67). Then, we

substituted the number of output layers into Eq. (30) to obtain the number of input

layers and recalculated equation (5-93) to determine the solution. (see Figure 5-16)

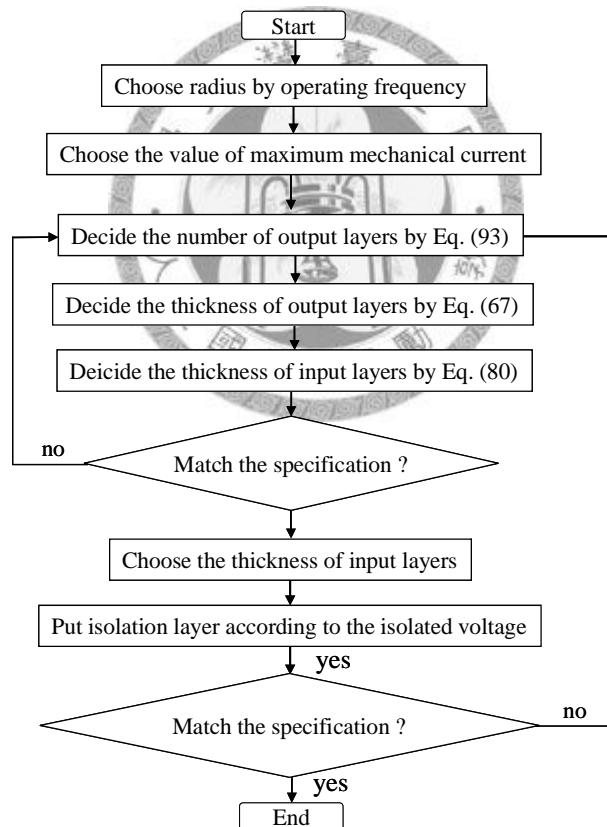


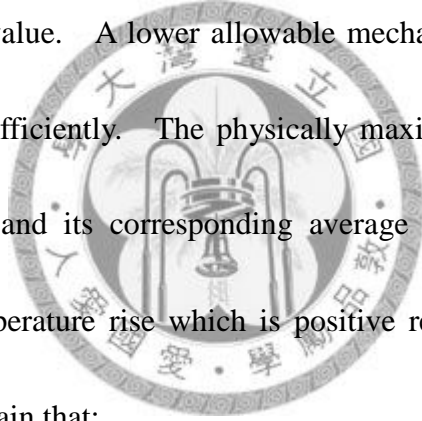
Figure 5-16. The design flow of the PT

A complete design example is demonstrated here. The given specification is that the

switching frequency be set at near 85 kHz, the DC input voltage at 30V, the load voltage

at 15V, and the load power varying from 1Watt to 10Watt. For simplicity, we neglected the voltage gain provided by input inductance and PT input capacitance since the input inductor is mainly used to achieve zero voltage switching condition but not provide a voltage gain. Therefore, the input voltage of the PT is $v_1 = 2V_{DC} / \pi = 19.1V$.

First, according to the operating frequency, we set the radius 13.5mm by the relationship of first column in Table 1. Then we determined the maximum allowable mechanical current in the case of a single layer. The experimental result was 0.3A, but it is a physical boundary value. A lower allowable mechanical current was preferred so it could operate more efficiently. The physically maximum mechanical current is shown in Figure 5-15(b) and its corresponding average temperature rise was 40°C roughly. Due to the temperature rise which is positive relative to the square of the mechanical current, we obtain that:



$$\Delta T \propto P_{PTloss} \propto I_m^2 \quad (5-94)$$

We set the temperature rise of the piezoelectric transformer at below 30°C, which means that:

$$I_{m,max} = 0.3A \sqrt{\frac{30^\circ C}{40^\circ C}} = 0.26A \quad (5-95)$$

Substituting equation (5-95) into equation (5-93), we set the number of the isolation layer and number of the input layer both to a value of 1 to solve equations (5-93), (5-67) and (5-80) in sequence. The result can be seen in the second column of Table 5-3.

However, the number of the output layers does not consider the number of input layers, so we set $m_1 = 4$ into equations (5-93), (5-67) and (5-80) again. It can be seen that only a thickness change is considered, and other parameters were converge. It should be noted that the different objective functions can still solve a minimum size by using the following design procedure. However, larger times of design loops are required. A proper objective function can save calculation time.

Table 5-3. the result of the design example

	First loop	Second loop
Number of output layers	$m_2 = 4$	$m_2 = 4$
Thickness in the output section	$t_2 = 0.3mm$	$t_2 = 0.61mm$
Number of input layers	$m_1 = 4$	$m_1 = 4$

5.2.6 Experimental Setup

Two PTs were made to verify the modeling and the prediction. First, a PT with size shown in Table 2 is made (PT-1). The thickness of the input layers are were to be the same thickness as that of the output layers, and two isolation layers were included for symmetric reasons. Moreover, another PT (PT-2) was made by adding 4 output layers to compare with PT-1. The detail information of implemented PT-1 and PT-2 are shown in Table 5-4 and Table 5-5 respectively.

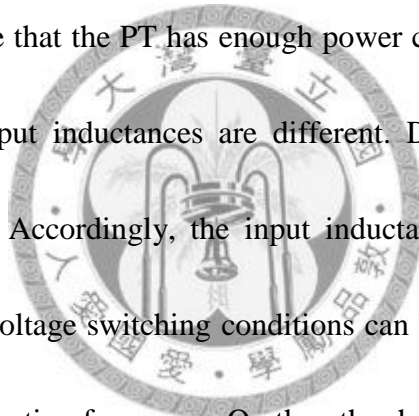
Table 5-4. The PT-1 specimen for the experiment

PT-1	input section		output section		isolation	
	number of layers	thickness	number of layers	thickness	number of layers	thickness
 	4	0.61mm	4	0.61mm	2	0.41mm
	radius $r = 13\text{mm}$ input inductance $L_{in} = 33\mu\text{H}$ operating frequency $\omega = 82.7\text{kHz}$ DC input voltage $V_{DC} = 30\text{V}$					

Table 5-5. The PT-2 specimen for the experiment

PT-2	input section		output section		isolation	
	number of layers	thickness	number of layers	thickness	number of layers	thickness
 	4	0.61mm	4	0.61mm	2	0.41mm
	radius $r = 13\text{mm}$ input inductance $L_{in} = 56\mu\text{H}$ operating frequency $\omega = 85.5\text{kHz}$ DC input voltage $V_{DC} = 50\text{V}$					

Both the specimens PT-1 and PT-2 were measured with the testing circuit shown in figure 2. The IR2104, IRF7431, MBR360 were adopted for the gate driver, the MOSFET switches and the rectifier respectively. The filtering capacitance was set to be 1000 μ F to minimize the ripple effect and the input inductances were set as 33 μ H and 56 μ H with switching frequency 82.7kHz and 85.5kHz respectively to achieve soft switching condition. In fact, we did not focus on the input inductances in this paper. We examined the conditions of the energy conservation and the maximum allowable vibration velocity to ensure that the PT has enough power capacity. However, it should be mentioned that two input inductances are different. Different PTs lead different impedance characteristics. Accordingly, the input inductance should be set different values to ensure the zero voltage switching conditions can be both achieved. The input inductances shifted the operating frequency. On the other hand, the input DC voltage of the PT-1 and PT-2 were 30V and 50V respectively. PT-2 required larger input voltage as the number of input layers did not increase with number of output layers, which was mentioned in equation (5-81). The PT-1 experimental waveforms of the input voltage v_{in} and the input current with are shown in Figure 5-17. The input current was lag to the input voltage to achieve the zero voltage switching condition. In addition, the PT-1 experimental waveforms of the rectifier voltage and rectifier current are shown in Figure 5-18 which matches the theoretical waveform (Figure 5-8) well.



To examine the efficiency with the load variations, the input voltage was modulated by the square wave at 200Hz and changes its duty cycle to fit the load specification under different load values. The waveform of input current is shown in Figure 5-19. This control strategy was called burst mode control or ON-OFF control which is widely used at fixed switching frequency controlled PT based converters. Figure 5-20 shows the total efficiency of the converter with load variations. It should be noted that equation (5-54) only introduced the losses in the rectifier and the PT itself. However, other components such as switching stage and the input inductor introduce losses as well. We set diode voltage drop was 0.3V and assumed all other undetermined losses cause the 96% of the efficiency totally. More specifically, the efficiency calculated by equation (5-54) was multiplied the value of 0.96 to correct the theoretical prediction. In Figure 5-20, the trend between the prediction and the measurement were similar and both two specimens kept the good efficiency (80% up) when the load is varied. It was mentioned that the larger size of PT has smaller mechanical current and lead better efficiency at same load power condition, but the larger number of gluing interfaces decreases its efficiency. Therefore, two specimens have similar efficiency even if the PT-2 is larger.

Furthermore, the mechanical current can be obtained by equations (5-67)~(5-69) and the temperature rise can thus be predicted by equation (5-94). A FliR InfraCAM

Thermal Imager was used to measure the temperature rise of the piezoelectric transformer. Since the heat distribution was not uniform on the piezoelectric transformer, three points on the lateral portion of the piezoelectric transformer were measured to obtain the average temperature. The experimental result and the prediction are shown in Figure 5-21. In Figure 5-20 and Figure 5-21, there are some deviations between the theoretical prediction and the experimental result when the temperature rise exceed around 20°C. These deviations are due to the quality factor of the PT decreases with the temperature rise, and thus the larger mechanical loss in the PT than the prediction. In addition, the dielectric loss may also increase with the temperature rise in PT.

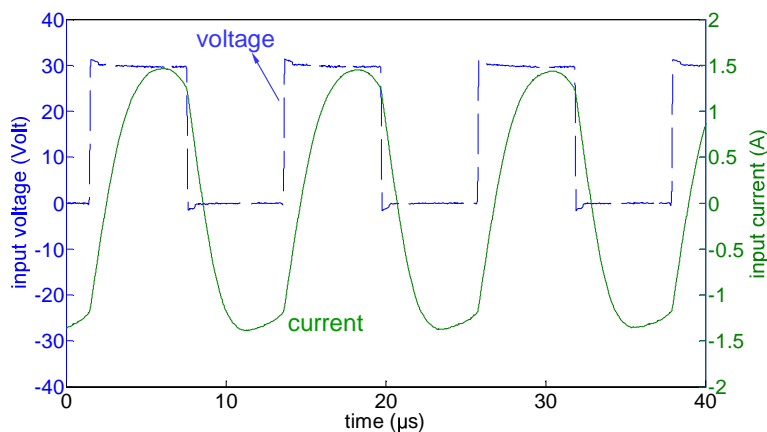


Figure 5-17. The waveform of the input voltage v_{in} (dotted line) and the input current (solid line)

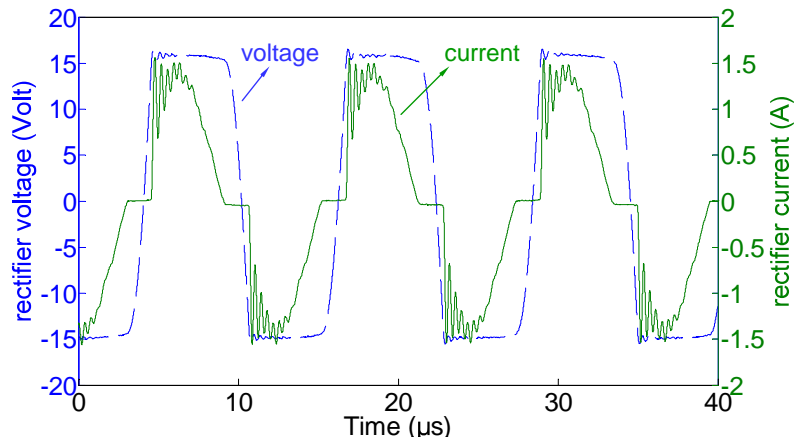


Figure 5-18. The waveform of the rectifier voltage v_{rec} (dotted line) and the rectifier current i_{rec} (solid line)

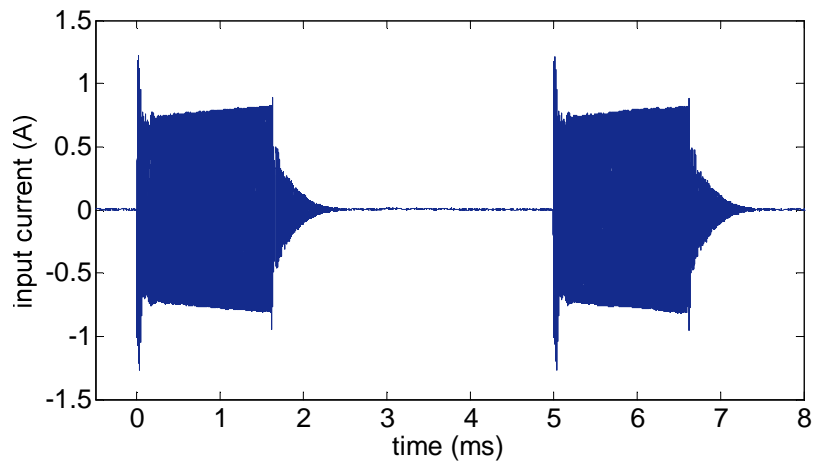
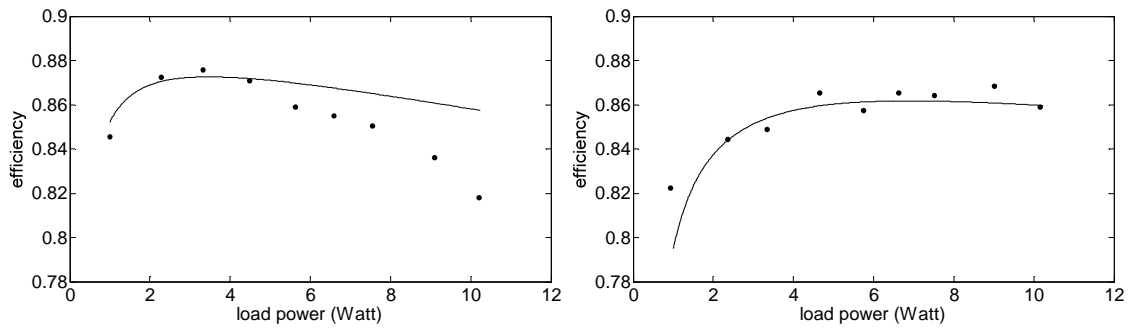


Figure 5-19. The burst-mode input current of PT-1



(a)

(b)

Figure 5-20. The total efficiency of the proposed converter: (a) PT-1 (b) PT-2 (solid line: prediction, dot: measurement)

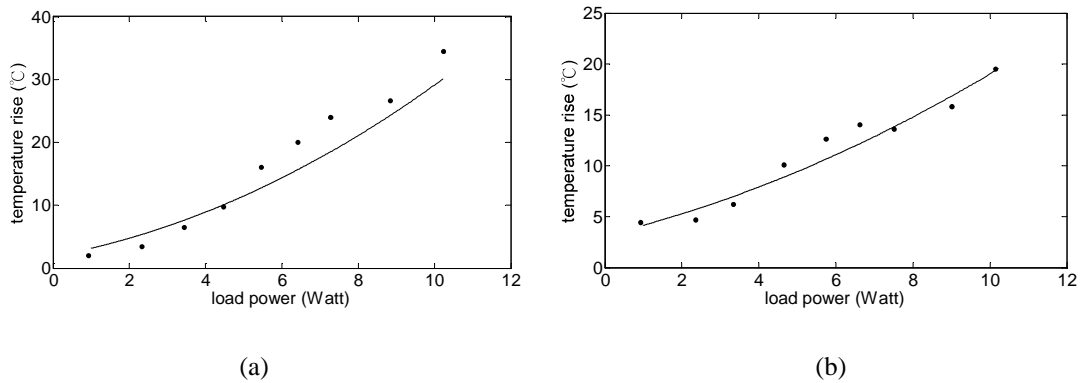


Figure 5-21. The temperature rise of (a) PT-1 (b) PT-2 (solid line: prediction, dot: measurement)

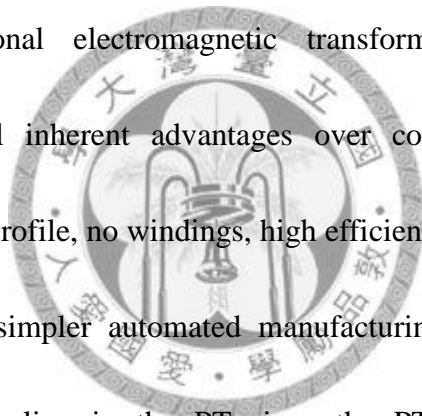


5.3 EMI Analysis of a DC/DC Converter Using a Piezoelectric Transformer

5.3.1 Background

Switching power supplies are widely used in commercial products in recent year. The EMI (Electromagnetic Interference) problem is a significant issue when designing switching power supplies. Poor designs could generate serious interferences to other electronic devices and cause safety issues. Nevertheless, commercial designs have to conform to the local or regional EMI safety regulations. The switching components in power converters are known to be the sources of EMI emissions during the switching periods. There are two possible coupling paths which cause interference to other electronic devices: capacitive coupling and magnetic coupling. Electromagnetic transformers transfer the electrical power but also undesired energy due to the leakage

flux and to capacitive effects. So, they provide the two paths for interferences. The electromagnetic transformer transfers energy through magnetic field, and thus noises can be radiated by the magnetic coupling. Furthermore, the parasitic capacitance of the transformer could also be a path for the propagation of common-mode noises. The EMI problems of conventional electromagnetic transformers in DC/DC converters have been already vastly studied [34, 35]. However, new topologies of power converters based on piezoelectric transformers (PT) are emerging, and the situation will be much different from conventional electromagnetic transformer designs. Piezoelectric transformers have several inherent advantages over conventional electromagnetic transformers, such as low profile, no windings, high efficiency, high power density, high operating frequency and simpler automated manufacturing processes. In addition, there is no magnetic coupling in the PT since the PTs transfer energy through mechanical vibrations. However, there are still parasitic capacitances in the PT to conduct common-mode noises. Piezoelectric transformers are using a high rigidity dielectric material to provide a high degree of insulation. The dielectric breakdown strength can be greater than several kV/mm. However, the dielectric isolation layer also enhances parasitic capacitive coupling between the input section and the output section. Lower EMI noises emitted from the PT implies that the size and the cost of the EMI filter in the power supplies can be reduced significantly. To design an appropriate EMI



filter for PTs, the EMI characteristics of PT based converters should be studied first. Although it is important to understand the common-mode noise characteristics in the PT. Few studies focus on the noises emission of PT based converters [36]. Accordingly, the main scope of this section is to construct a model for the common-mode noises emission of the PT, and using it to verify the EMI characteristics of the PT based power converter. The specifications of the DC/DC converter studied in this paper are set as follows: the switching frequency is set around 85 kHz, the input voltage is 30V, the output voltage is 15V, and the output power can vary from 1 to 10W. The regulation is made by burst-mode hysteretic feedback [37]; the efficiency is higher than 80%.



5.3.2. EMI Emission in the DC/DC Converter

Figure 5-22 shows the block diagram of the tested PT based DC/DC converter.

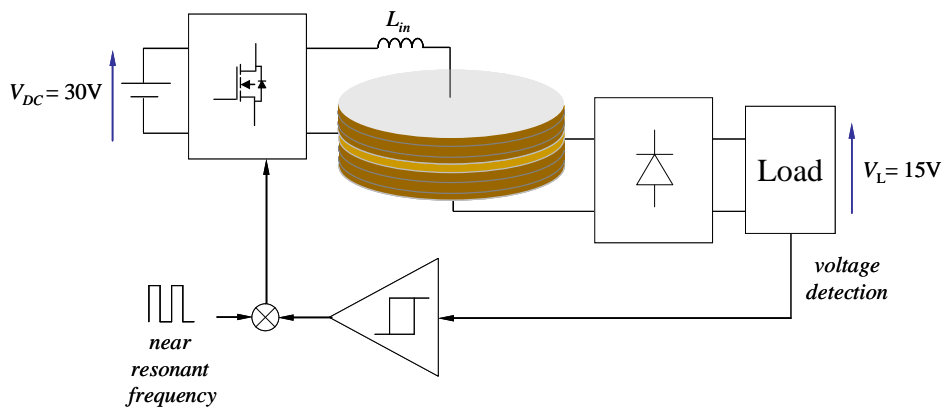


Figure 5-22 The block diagram of the piezoelectric transformer based DC/DC converter

The input driving circuit (DC/AC converter) is used to drive the PT near its resonant frequency. The driving frequency is determined by the gain characteristic of the PT. The PT transfers energy to its output terminal and generates the required DC voltage through the rectifier connected at the secondary of the PT. The regulation is achieved by burst-mode hysteretic feedback control. The circuit topology of the power stage is shown in Figure 5-23, where the equivalent circuit of the PT is clearly illustrated. In order to optimize the energy transfer efficiency, the working condition is always in ZVS (zero voltage switching) condition and the driving frequency is fixed.

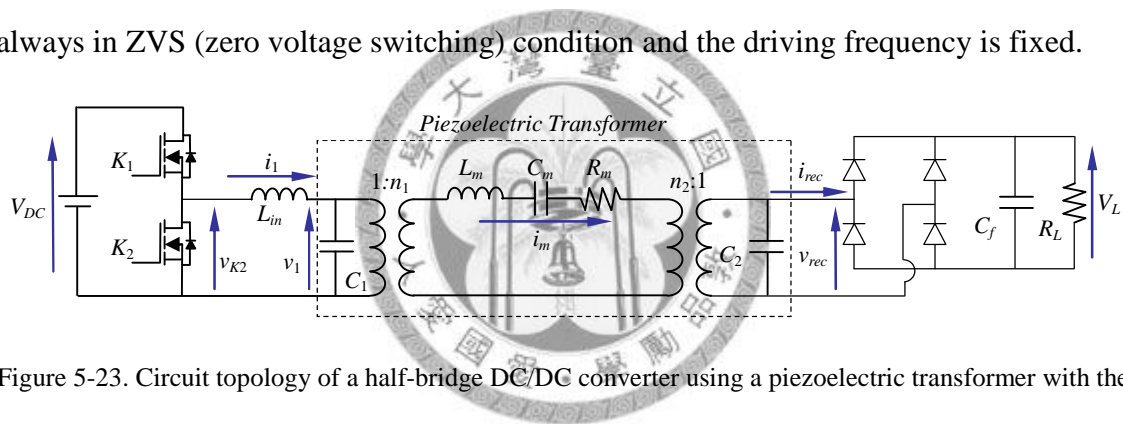


Figure 5-23. Circuit topology of a half-bridge DC/DC converter using a piezoelectric transformer with the series inductor

There are two types of perturbations which generate noises and interferences in an electrical system: the differential mode noise and the common mode noise. The differential-mode current flows into the DC bus, but it is easily filtered out by the bulk input capacitor of the converter. The common mode current flows through the system ground. Since the ground loops can be large and undefined, this current generates radiated fields and voltage drops through the parasitic common impedances. In the switching power system, the main sources of perturbations are the power

semiconductors. The consequence is that the capacitance of the transformer provides a natural path for the propagation on the common mode current.

Figure 5-24 shows the common mode path in the converter, where i_{cm} is the common mode current and C_p is the leakage capacitance between the primary side and the secondary side of the transformer. No matter electromagnetic transformers or piezoelectric transformers, both always exhibit common mode capacitances. It should be noted that the output negative pin of the converter is linked to ground in most applications. In Figure 5-24, the converter input is supplied through a *line impedance stabilization network* (LISN) to measure conducted EMI. In this setup, the capacitive coupling of the PT is obviously a natural path for the common mode current.

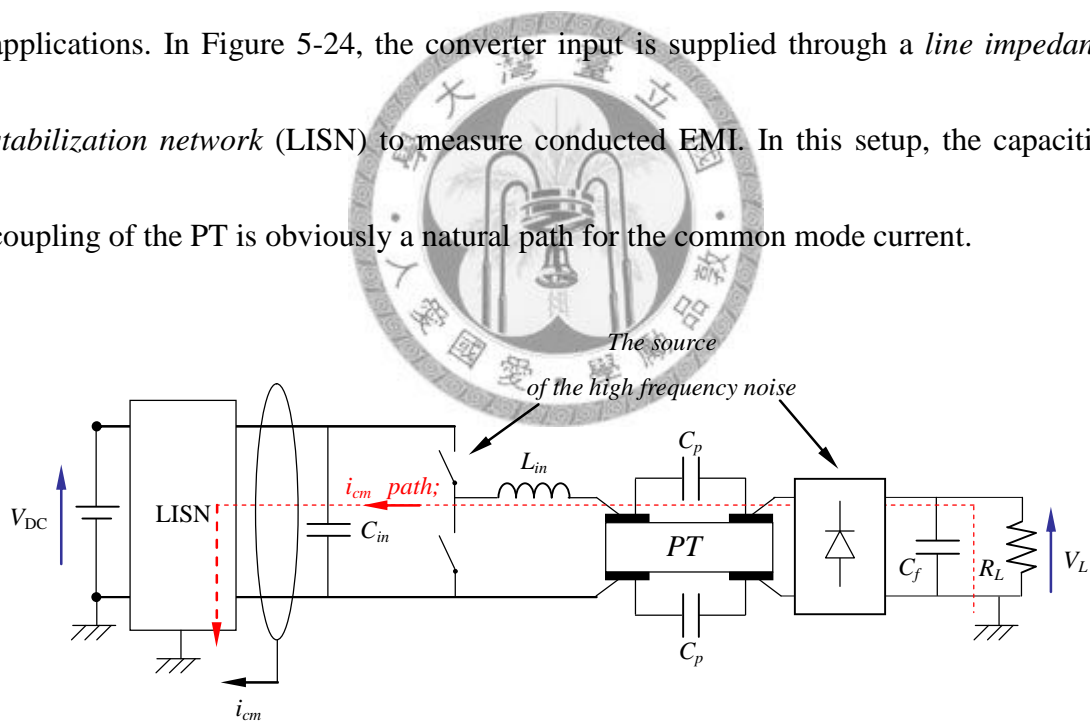


Figure 5-24. Equivalent circuit of the DC-DC converter with LISN setup for common mode noises measurement.

A. Capacitive couplings in the PT

The configuration of the PT specimen is shown in Figure 5-25. This is a stacked disk-type PT, operating in radial mode. The multi-layer structure is composed of 4 input layers and 8 output layers. Primary secondary and insulation layers are made of the same PZT material. Table 5-6 details the layers thicknesses.



Figure 5-25. Pictures of the stacked disk-type piezoelectric transformer operating in radial mode

Table 5-6. Geometrical dimensions of the PT under test.

	Number of layers	Thickness	Radius
Input section	4	0.61mm	13mm
Output section	8	0.61mm	13mm
Insulation	2	0.41mm	13mm

We can see Figure 5-26 that the common mode capacitive coupling in the PT is mainly located between the primary and secondary layers. Compared with electromagnetic transformers where capacitive couplings are distributed in the windings, the capacitive coupling in a PT is mainly located between the bottom electrode of the primary layers and the top electrode of the secondary layers. The three capacitances were measured with a network analyzer HP4194A. The values of these capacitances are:

input capacitance $C_1=34\text{nF}$, output capacitance $C_2=77\text{nF}$ and coupling capacitance $C_p=150\text{pF}$ (Figure 5-26). Considering that the relative permittivity of PZT material is about 1200, the theoretical values of the primary and secondary capacitances are 37nF and 74nF , respectively.

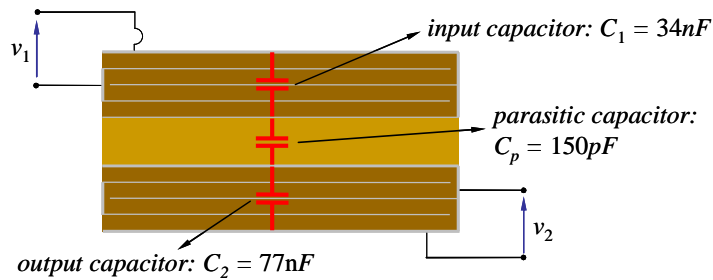


Figure 5-26 Equivalent circuit of the PT parasitic capacitances coupling common mode noises

B. Conducted EMI measurement

An experimental setup has been realized in Figure 5-27, such a configuration is used in automotive or aeronautics. The DC-DC converter is insulated from the ground reference with a two centimetres thick PVC plate. The power source is provided through a line impedance stabilization network (LISN). Table 5-7 indicates the values of the components of the LISN. Common mode noises were measured with a current probe placed between the LISN and the converter.

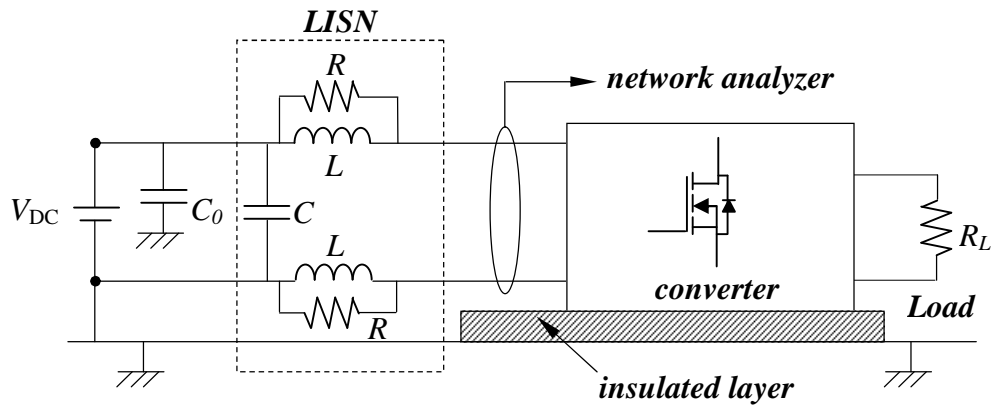


Figure 5-27. Experimental setup for the measurement on conducted noise in the PT based DC/DC

converter

Table 5-7. Component values in the LISN setup

C_0	C	L	R
$10\mu\text{F}$	$100\mu\text{F}$	$1\mu\text{H}$	25Ω

The connection between the PT and the half-bridge circuit plays an important role on the flowing of the common mode current. Two popular configurations of the connection are shown in. In the case of Figure 5-28(a), the middle point of the half-bridge is connected through the inductor L_{in} at the top input electrode of the PT, the stable potential (ground) is connected at the bottom electrode of the primary layer. In the case of Figure 5-28 (b)), the middle point of the half-bridge is connected through the inductor L_{in} to the bottom input electrode of the PT. In this configuration, the voltage of this electrode swings significantly, creating a large common mode current through C_p .

We will show later that the configuration in Figure 5-28(a) is better for the rejection on the common mode current. Figure 5-29 shows the implemented PT DC-DC converter on a printed circuit board.

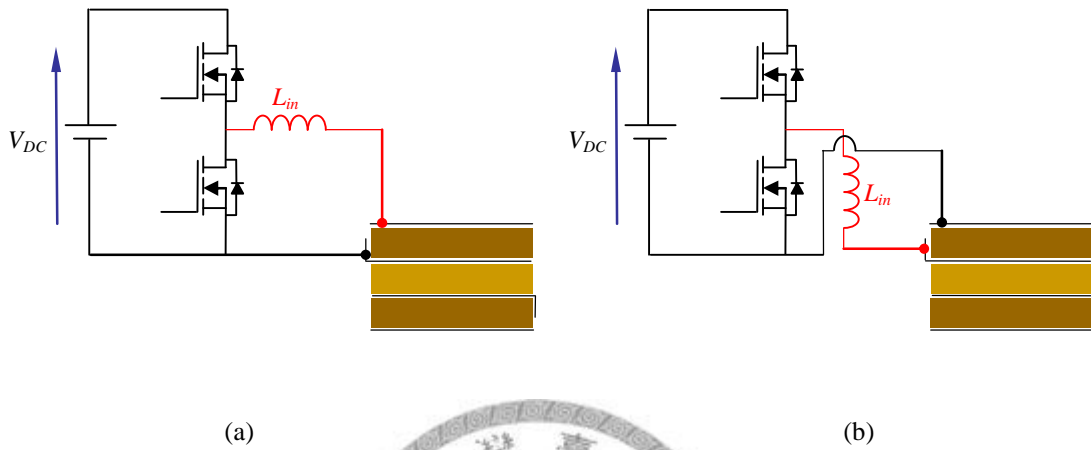


Figure 5-28. The PT and the half-bridge circuit connecting configurations: (a) middle point of the half-bridge is connected with the PT top electrode; (b) middle point of the half-bridge is connected with the PT bottom electrode

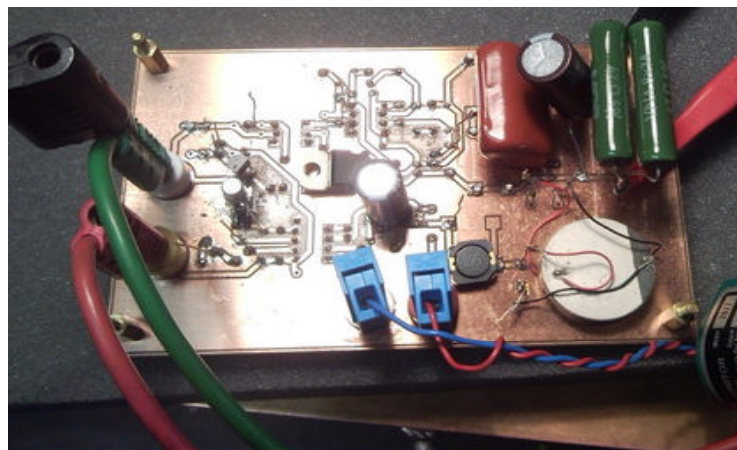


Figure 5-29. Experimental circuit board for measurement on conducted noises in a PT based DC-DC converter

5.3.3 . Circuit Models for conducted EMI

In this section, we present an equivalent circuit model to describe how the common mode currents are created and propagated throughout the converter. Figure 5-30 shows an equivalent model of the converter where the inverter leg is represented by the voltage source v_{K2} . Current source i_m is resulting from the electromechanical conversion of mechanical energy inside the PT (mechanical current). Introducing the capacitors of the PT presented in Figure 5-26, the inverter legs and the series inductor can be connected to top electrodes directly as Figure 5-28(a) (i.e. $A \rightarrow In1$, $B \rightarrow In2$) or connected to electrodes inversely as Figure 5-28(b) (i.e. $A \rightarrow In2$, $B \rightarrow In1$). These two configurations have to be both considered since they lead to much different behaviors.

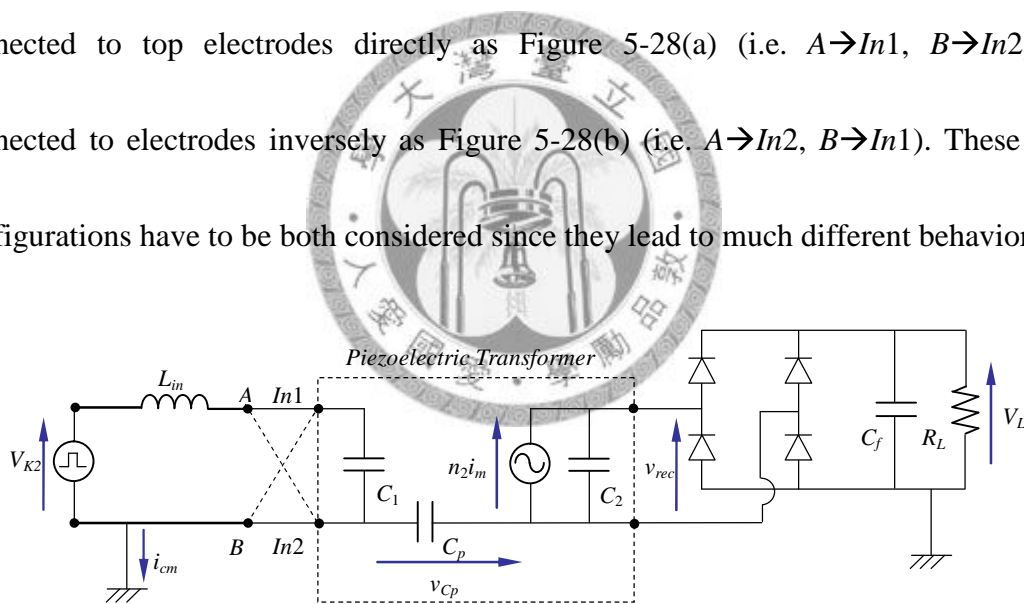


Figure 5-30. The equivalent circuit model for the common mode current analysis

Consider the configuration in Figure 5-28(a) where the inverter legs A and B are directly connected to $In1$ and $In2$ respectively. Waveforms of the mechanical current i_m , common mode current i_{cm} , PT output voltage v_{rec} and parasitic capacitance voltage v_{Cp} are shown in Figure 5-31.

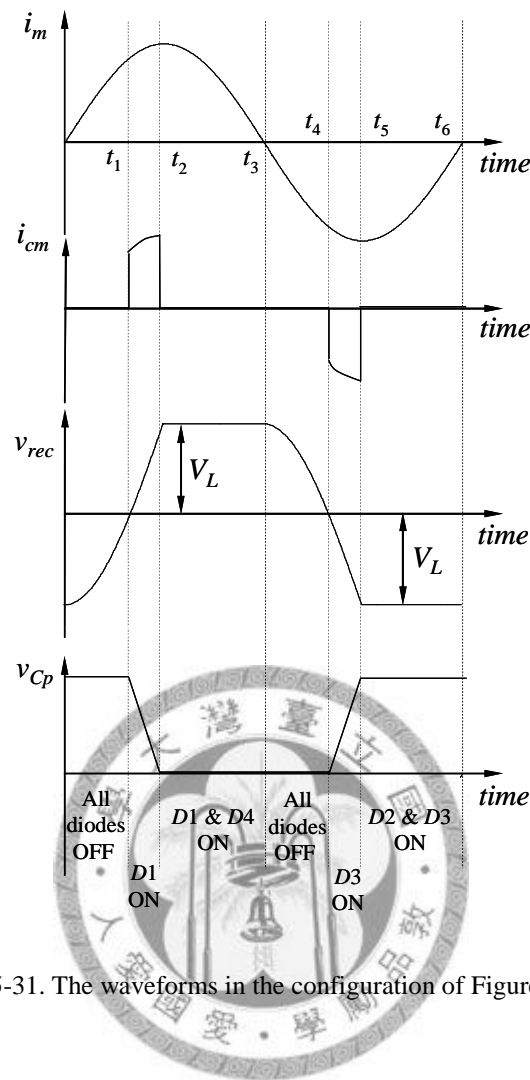


Figure 5-31. The waveforms in the configuration of Figure 5-28a

During time from 0 to t_1 , all diodes in the rectifier are in “OFF” state, capacitor C_2 is charged, and the output voltage v_{rec} is rising. The final voltage of v_{rec} is determined by capacitance C_2 and the charging current i_m . In this period, the voltage v_{Cp} is equal to the load voltage, $v_{Cp}=+V_L$, since the capacitor C_p has been already charged when diodes D_2 & D_3 were conducting in the previous period. At instant t_1 , output voltage v_{rec} approaches 0 and diode D_1 is switched “ON”. Therefore, v_{Cp} varies during period t_1 to t_2 and i_{cm} is proportional to i_m ; the relationship is expressed by equation (5-96).

$$i_{cm} = \frac{C_p}{C_2} i_m \quad (5-96)$$

At instant t_2 , the diode D_4 is switched “ON” because v_{rec} reaches $+V_L$ and $V_{Cp}=0$. At instant t_3 , all diodes are switched “OFF” and the current i_{cm} is null during t_3 to t_4 . At instant t_4 , the diode D_3 is switched “ON” because v_{rec} reaches 0. From t_4 to t_5 , v_{rec} decreases to $-V_L$ while v_{Cp} rises oppositely. Consequently, i_{cm} is no longer null and can be predicted by the same expression (5-96) as previously.

Consider now the configuration of Figure 5-28(b), that is, the inverter legs are linked inversely to electrodes ($A \rightarrow In2$ & $B \rightarrow In1$). In this configuration, parasitic capacitance C_p works similarly as in the first configuration. More specifically, the current still passes through the period $[t_1, t_2]$ and period $[t_4, t_5]$ according to the switching condition of the diodes. However, the common-mode current is not only determined by the connected rectifier and the load but also depends on the input voltage v_{K2} . Accordingly, capacitance C_2 and the diode bridge allow this current to flow in both directions. Therefore, the common mode current results from the sum of these two effects. The resulting common mode current i_{cm} is represented in Figure 5-32.

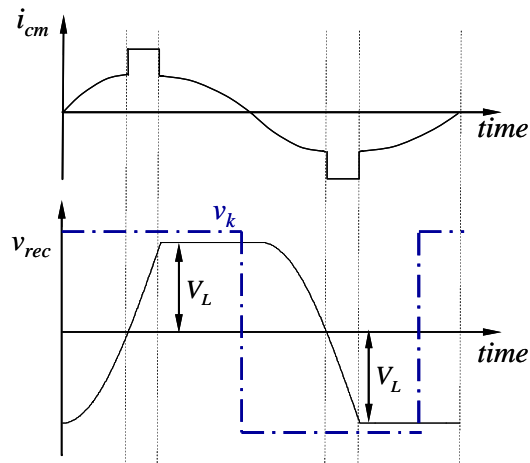
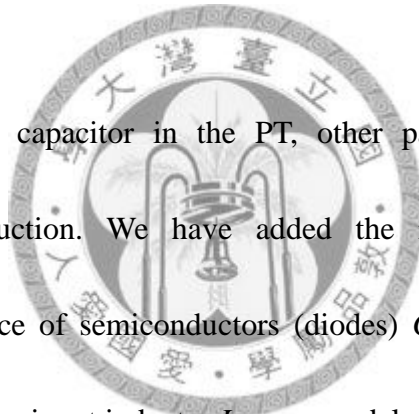


Figure 5-32. The waveforms of the common mode current i_{cm} and the PT output voltage in the configuration of Figure 5-28 (b)



Besides the parasitic capacitor in the PT, other parasitic effects would also contribute to EMI conduction. We have added the inductance of connections $L_C=1000\text{nH}$, the capacitance of semiconductors (diodes) $C_D=50\text{pF}$, impedance of the LISN (see Table 5-7) and the input inductor L_{in} was modeled as a parallel RLC network. The complete model is shown in Figure 5-33. This one can lead to more accurate prediction of common mode current i_{cm} , but it is too complex to analyze analytically. The simulation results are shown in Figure 5-34. The circuit behavior depicted previously can be verified, but the waveform is slightly different because of contribution from other parasitic effects such as the diode capacitances or the inductance of connections.

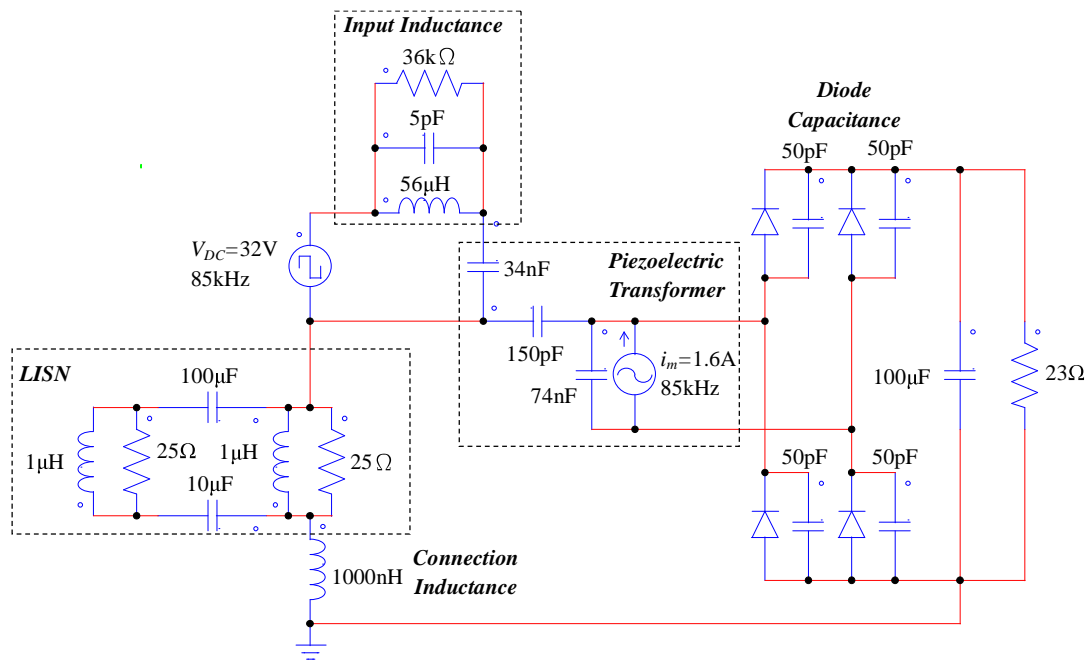


Figure 5-33. Complete circuit model with parasitic effects on the common mode noises conduction used



in PSIM simulation

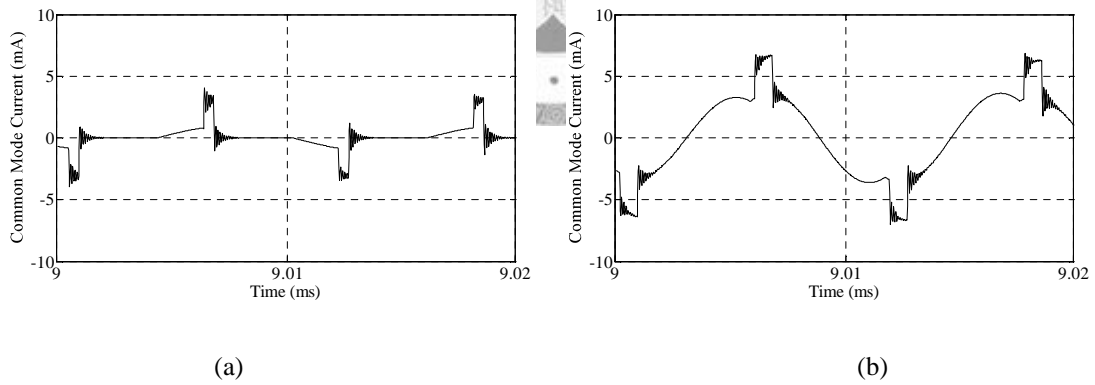


Figure 5-34. The simulation results of the common mode current i_{cm} : (a) i_{cm} in configuration of Figure

5-28a (b) i_{cm} in configuration of Figure 5-28b

5.3.4 Experimental Results and Discussions

Figure 5-35 shows the waveforms measured at different points of the converter using a Tektronix TDS3014B oscilloscope (100MHz bandwidth and 1.25GHz sampling rate with four-input channels), under the following working conditions: $V_{DC}=30V$, $V_L=15V$, $R_L=23.5\Omega$, $f=85kHz$. The waveforms represented are (from upper to lower): voltage v_{K2} at the MOSFET switch K_2 , the PT output voltage v_{rec} , and the common mode current i_{cm} of the two configurations. We can see that, as predicted, the connection of the inverter leg maximizes the common mode current in the configuration of Figure 5-28b and the configuration in Figure 5-28a minimizes it.

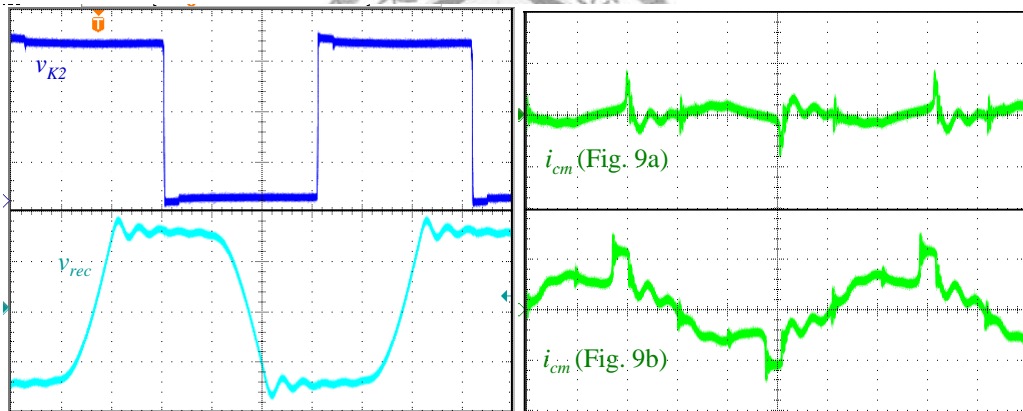


Figure 5-35. Left plots: waveforms v_{K2} in 10V/div and v_{rec} in 10V/div of configuration Figure 5-28a.

Right plots: i_{cm} in 5mA/div of configuration Figure 5-28a and i_{cm} in 5mA/div of configuration Figure

5-28b (horizontal scale: $2\mu s/div$)

Measurements shown in Figure 5-35 confirm the above analysis on the connection between the inductor and PT electrodes is crucial in the conduction of the common mode current. Specifically, in the configuration of Figure 5-28(a), the connection of the

inverter to the primary electrodes can minimize the common mode current. However, even in the opposite case (Figure 5-28(b)), the input inductor L_{in} and the PT input capacitance C_1 constitute a low-pass filter to filter out the high-frequency components of the square wave voltage v_{K2} and generate a sinusoidal-like waveform at the PT input. Therefore, the input signal of the PT only influences the first harmonic of the spectrum of the common mode current. On the other hand, the output rectifier also makes a very specific contribution to the common mode current. The sharp switching of the rectifier (see Figure 5-31 and Figure 5-35) generates high frequency ringing in the common mode circuit because of the inductive connection; this is proper to PT technology.

Figure 5-36 and Figure 5-37 show the spectrum of common mode current i_{cm} in the two configurations. The frequency range is set from 10 kHz to 30MHz. The amplitude of the first harmonic corresponding to the switching frequency (85 kHz) is 40 μ dBa in the configuration of Figure 5-28(a) and 62 μ dBa in the configuration of Figure 5-28(b), matched with our analysis. As a final point, these spectrums show the specific conducted perturbations emitted by a PT based DC/DC converter, mainly determined by the circuit connected at the output terminal and the intrinsic nature of the piezoelectric transformer.

This section studies the emission of conducted common mode current in a DC/DC converter using a stacked disk-type piezoelectric transformer, operating in radial mode.

The study focused on the specific capacitive coupling behaviors of the PT and also on the analysis of the conduction of the common mode currents. We have shown that the connection between the inverter and the input electrodes of PTs significantly influences the intensity of the first harmonic of the common mode current. The parasitic switching of the rectifier, due to the output of the PT contributes largely to the HF harmonics. Finally, we have shown that our model can predict accurately the common mode current in a PT based DC/DC converter. Future studies will focus on how to find out a solution avoiding this phenomenon.

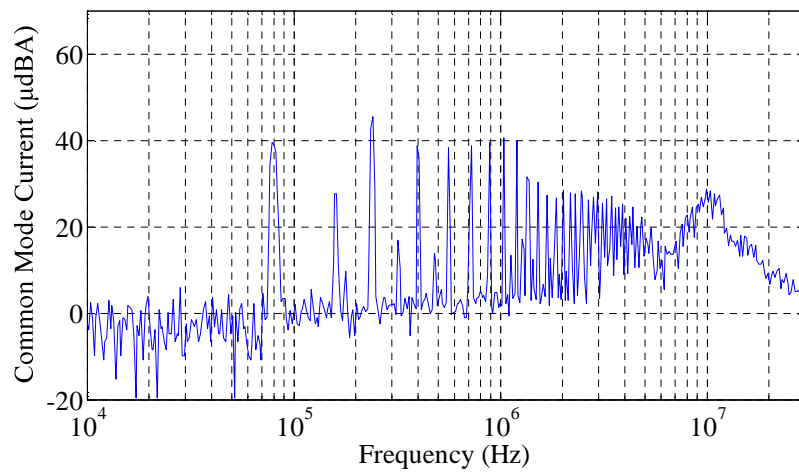


Figure 5-36. The spectrum of the common mode current when middle point of the half-bridge is connected at the top PT electrode (the configuration of Figure 5-28a)

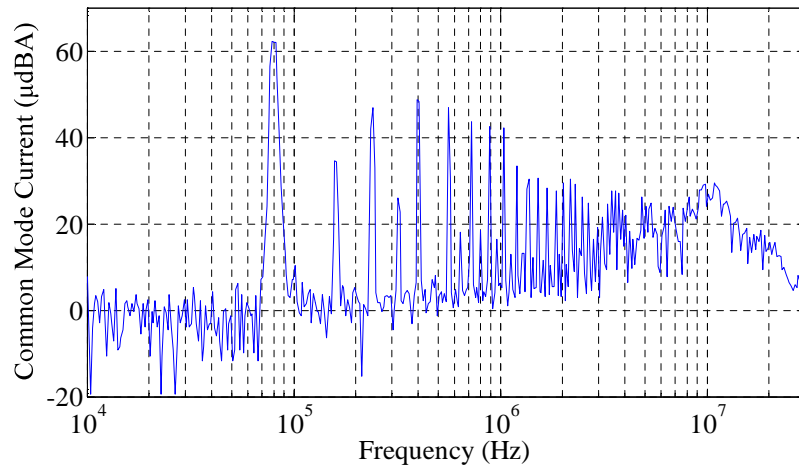


Figure 5-37 The spectrum of the common mode current when middle point of the half-bridge is connected at the bottom PT electrode. (the configuration of Figure 5-28b)



5.4 Summary

In this chapter, we developed a complete design rule for the piezoelectric transformers DC/DC converter with constant load voltage. The models of two PT fed rectifier, half-wave rectifier and the full-wave rectifier were developed first. The full-wave rectifier was then selected due to the higher power density. The vibration velocity, dimensional constraints, energy balance, quality factor correction and ZVS conditions are all considered to develop the complete design procedure. The 10Watt/15V DC/DC converter was designed based on the proposed procedure. The proposed converter can keep at least 82% efficiency and within 10°C temperature rise with 1-10 Watt load variations. The model of the conducted EMI was then developed by

the converter.



Chapter 6. Velocity controlled Piezoelectric Layer fed

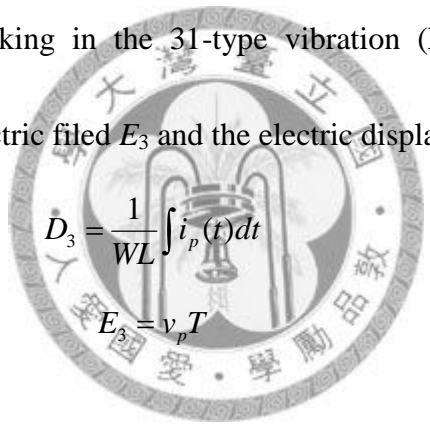
Rectifiers

The major topic in this chapter is to define an optimal piezoelectric layer fed rectifier. In the previous section, the full-wave rectifier was adopted as the rectifier for the piezoelectric transformer based converters. However, the full-wave rectifier is not the best rectifier based on the viewpoint of the power density. To optimize the piezoelectric layer fed rectifier, the piezoelectric voltage has to follow the mechanical current to correct the power factor of the piezoelectric layer. To simplify the analysis, the concept of the work cycle or said the energy cycle is introduced in this chapter. The optimal rectifier proposed herein is called velocity controlled piezoelectric layer fed rectifier (VPR). This rectifier can be applied in many converters and particularly to the piezoelectric damper application to suppress the vibration of the structure. The results presented hereafter show that the displacement of the vibration can be cancelled effectively by using the VPR.

6.1 Work Cycle Observation for the Piezoelectric Layer

In the previous chapter, we have developed a full design procedure of a PT in different applications. In each design, to get the higher power density PT is a topic of

interest. Besides to improve the material properties and adopted different vibration modes of PT, the design of the circuit topologies is also an important part to optimum the power density. To observe the power density of piezoelectric structure, the concept of the “work cycle” [15] is introduced in this chapter. The work cycle is the energy path of the PT on the stress/strain plane or electric field/electric displacement. In practice, the stress, strain, electric field and the electric displacement can be observed based on the voltage waveform and the current waveform of the PT. First of all, assume the piezoelectric layer is working in the 31-type vibration (Figure 6-1). Applying the electrostatic equations, electric field E_3 and the electric displacement D_3 leads to:



$$D_3 = \frac{1}{WL} \int i_p(t) dt \quad (6-1)$$

$$E_3 = v_p T \quad (6-2)$$

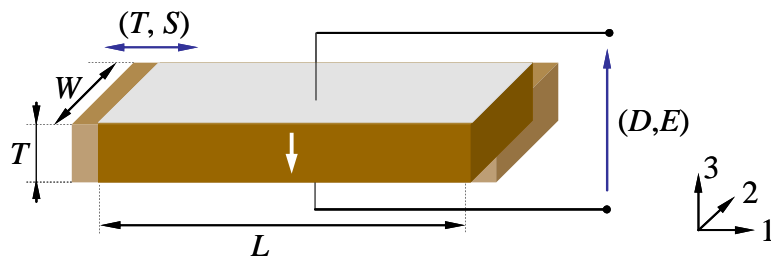


Figure 6-1. Mechanical and electrical coupling of the piezoelectric 31-type vibration

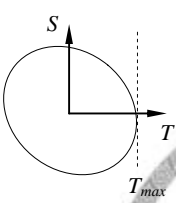
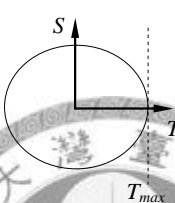
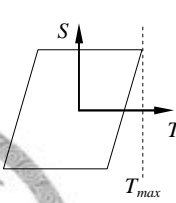
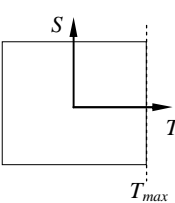
Next, the normal stress T_1 and the normal strain S_1 of the PT can also be obtained from the constitutive law:

$$T_1 = (D_3 - \epsilon_{33}^T E_3) / d_{31} \quad (6-3)$$

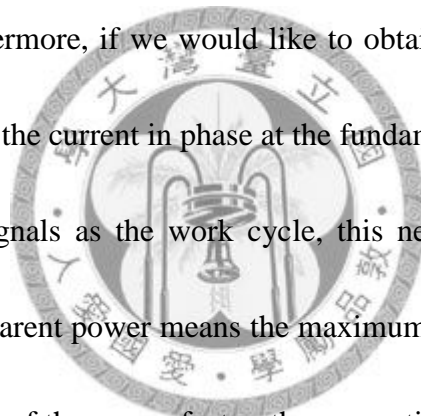
$$S_1 = s_{11}^E T_1 + d_{31} E_3 \quad (6-4)$$

Before examine the real rectifier, two typical waveforms, the sinusoidal waveform and the square waveform, are examined first. The work cycles corresponding to these two typical waveforms are showed in Table 6-1.

Table 6-1. The work cycles with the basic waveforms

	Oblique Ellipse	Ellipse	Parallelogram	Rectangular
Shape of work cycle				
Voltage/current Waveform	Sinusoidal/ Sinusoidal with phase difference	Sinusoidal/ Sinusoidal in phase	Square/Sinusoidal with phase difference	Square/ Sinusoidal in phase
Energy (Joules) (area of work cycle)	$\pi S T \cos \theta$	$\pi S T$	$2S(2T - \frac{2S}{s_{33}^E})$	$4ST$
<p>T_{\max} is the maximum stress</p> <p>f is the operating frequency (Hz)</p>				

There are several important factors that can be extracted by the work cycle method. First of all, the area of the work cycle represents the energy density, and we can find the maximum physical quantity on the work cycle. For example, the maximum stress is indicated by the dotted line in Table 6-1. For the other import factor, we can also estimate the power factor from the work cycle. If there is no phase difference between the voltage and the current, the work cycle should be symmetric to the axis without a rotating angle. In other words, the symmetry of the work cycle implies the information of the power factor. Furthermore, if we would like to obtain the optimal power factor, we can put the voltage and the current in phase at the fundamental frequency first. Then, plotting these two new signals as the work cycle, this new work cycle is related to “apparent power”. The apparent power means the maximum possible transferring power. According to the definition of the power factor, the area ratio between the original work cycle and the apparent work cycle is the power factor. Table 6-1 demonstrates that the rectangular work cycle has the highest power density, because it spans largest area on the work cycle under the maximum stress condition. Moreover, the rectangular work cycle also has the best power factor (power factor = 1) due to the symmetry. Undoubtedly, the rectangular work cycle is ideally the one. To obtain the best power capacity of the piezoelectric layer, the voltage waveform and the current waveform should not only be set in phase but also be set in squared and sinusoidal waveform



respectively.

More specifically, to have rectangular work cycle, there are two requirements on the PT fed rectifier: The first one is to put the piezoelectric voltage and the mechanical current in phase, and that is equivalent to the concept of power factor correction. Figure 6-2 shows the basic idea to implement the power factor correction. The mechanical current is detected to control the phase of the rectifier voltage (piezoelectric voltage).

Since the rectifier is controlled by the mechanical current (velocity), this rectifier is called “velocity controlled piezoelectric layer fed rectifier (VPR)”. Besides tracking the phase, the rectifier also has to shape the piezoelectric voltage in squared waveform. The

implemented circuit topology of the VPR is shown in Figure 6-3. To put the mechanical current and the piezoelectric voltage in phase, four switches are used to control the

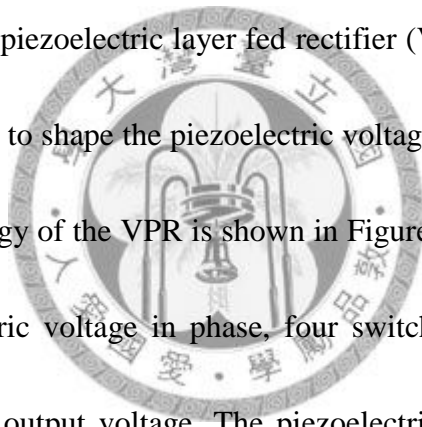
phase of the piezoelectric output voltage. The piezoelectric current sensor is used to

detect the mechanical current (velocity) of the piezoelectric layer. When the mechanical current is positive, switches *SL1* and *SR2* are ON and switches *SL2* and *SR1* are OFF

(Figure 6-3(a)). The piezoelectric voltage is thus positive and equal to the load voltage in this period. When the mechanical current is negative, switches *SL1* and *SR2* are ON

and switches *SL2* and *SR1* are OFF (Figure 6-3(b)). The piezoelectric voltage is thus equal to negative load voltage in this period. Accordingly, the mechanical current and

the piezoelectric voltage are then in phase. The ideal waveforms are shown in Figure



6-4.

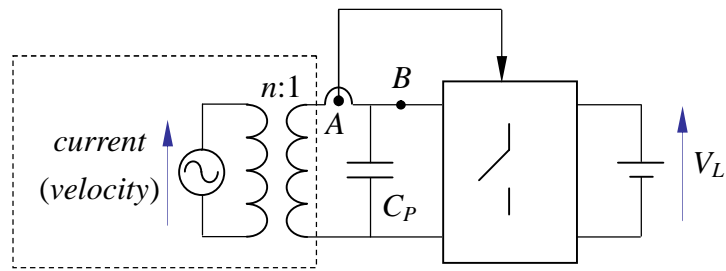


Figure 6-2. The block diagram of the velocity-controlled piezoelectric layer fed rectifier

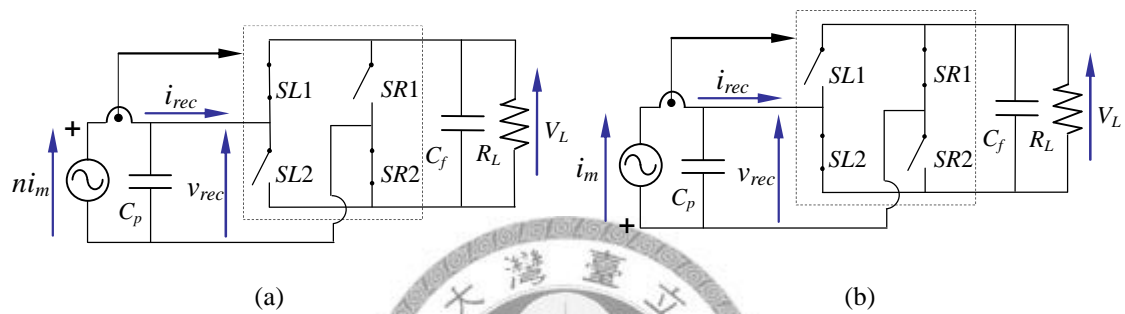


Figure 6-3. The velocity controlled piezoelectric layer fed rectifier (VPR)

(a) when mechanical current is positive (b) when mechanical current is negative

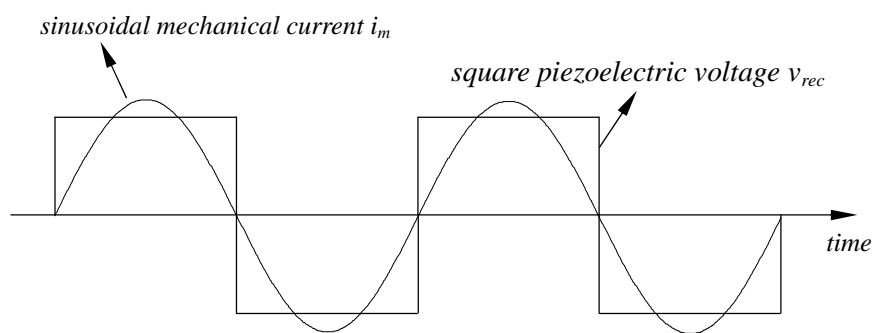


Figure 6-4. The ideal waveform of the velocity controlled piezoelectric fed switching rectifier

On the other hand, there are several possible PT fed rectifiers. Some important characteristics of the PT fed rectifiers, including MPPT (Maximum Power Point

Tracking), PFC (Power Factor Correction) and work cycle are summarized in Table 6-2.

The basic rectifier is case 1, *i.e.* voltage-mode full-wave rectifier. This rectifier is the simplest one but it does not have good characteristics due to the contribution of the piezoelectric output capacitor C_2 . Similarly to the case of the resistive load in Chapter

2, an inductor is added to compensate the contribution of the PT output capacitor. The parallel inductor still has better characteristics than series inductor, especially on the

power factor. In case 4, a series inductor is put after the rectifier. Different from the cases of inductors added before the rectifier, this series inductor should approximately

match two times of the operating frequency because of the fundamental frequency is doubled after the rectifier. However, putting a series inductor *before* the rectifier can

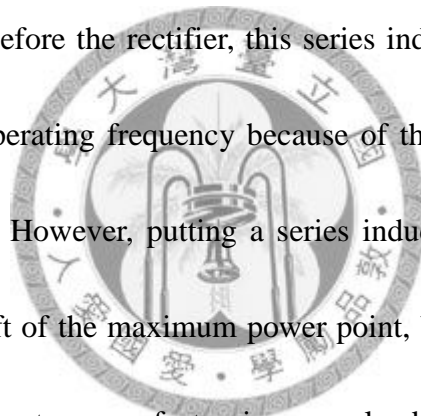
improve the frequency shift of the maximum power point, but putting a series inductor *after* the rectifier can correct power factor in some loading ranges. Moreover, the

parallel inductor can both solve the MPPT and PFC problems. On the other hand, the

active rectifier is adopted in Case 5 and 6 are controlled by the mechanical current. The main purpose of the velocity-controlled rectifier is to achieve MPPT and PFC at the

same time. The output voltage of the PT is forced to be in phase with the mechanical current, and the mechanical current source always operates as an equivalent resistor.

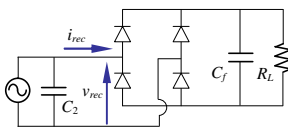
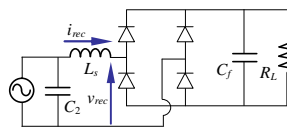
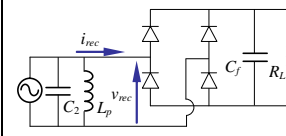
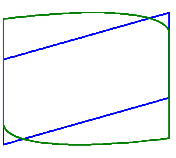
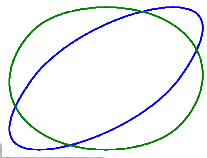
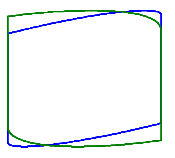
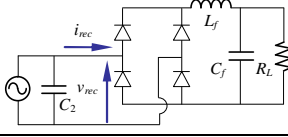
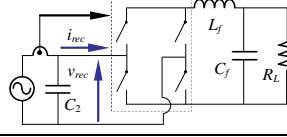
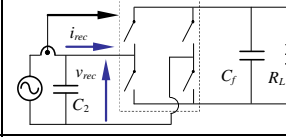
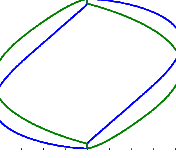
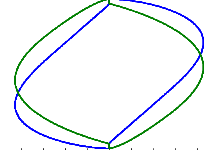
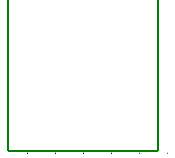
However, there are active switching problems on active rectifier based circuits. The series inductor is thus added to alleviate the switching problem but also keep MPPT and



PFC functions. More detailed characteristic curves of these PT fed rectifiers are shown

in the Appendix A.

Table 6-2. Six PT fed rectifiers

	1. voltage-mode rectifiers	2. series inductor before the rectifier	3. parallel inductor before the rectifier
Topologies			
Typical work cycle			
MPPT Condition	No	$L_s = \frac{1}{\omega^2 C_2}$	$L_p = \frac{1}{\omega^2 C_2}$
PFC Condition	No	No	$L_p = \frac{1}{\omega^2 C_2}$
Other advantages /drawbacks	Simple, no magnetic components	No	Not suitable in high load voltage
	4. series inductor after the rectifier	5. velocity controlled rectifier with an inductor	6. velocity controlled rectifier
Topologies			
typical work cycle			
MPPT Condition	No	Always	Always
PFC Condition	$L_f \cong \frac{1}{4\omega^2 C_2}$	$L_f \cong \frac{1}{4\omega^2 C_2}$	Always
Other advantages	Small load range	need extra driver	1. extra driver needed 2. extra switching losses

/drawbacks			
Note: blue/green work cycles are original/apparent work cycle respectively			

6.2 Velocity-Controlled Switching Piezoelectric Damping

One of the applications of the piezoelectric layer fed rectifier is shunt damping for structures [38, 39, 40]. In a piezoelectric damping system, the piezoelectric layer is bonded to a host structure. Once the host structure vibrates, piezoelectric layers can transfer the vibration energy to the electrical energy and dissipates the energy to a connected shunt circuit. Piezoelectric passive shunt damping was widely adopted in the vibration suppression.

Compared to active vibration control, passive shunt damping is easier to accomplish as it does not need heavy amplification. However, the typical passive shunt damping only has good performance in relative small bandwidth. On the other hand, the semi-active shunt damping has larger control bandwidth and does not need heavy power supply, thus the semi-active shunt damping is the most popular technique in recent years. Several semi-active control methods were proposed, such as state-switched absorber [41, 44] and synchronized switching damping (SSD) techniques [42, 43, 44, 45], which could improve the conventional method. However, there are two significant problems of the semi-active damping to be addressed:

- 1) The first problem is that the semi-active damping has poorer performance than

the typical passive damping although the semi-active damping is more adaptive.

2) The second problem is that the analysis of the semi-active damping is not easy to do, due to the nonlinearity. The concept of the VPR can be used as the shunt circuit since it owns the optimal square work cycle.

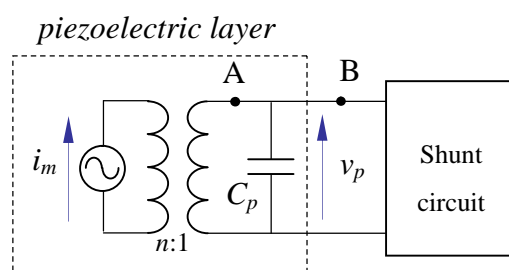


Figure 6-5. Equivalent circuit of the PT with a shunt circuit

To understand the power dissipation in the piezoelectric shunt damping more clearly, the power generated from the structure vibration is examined first. The equivalent circuit of the PT with a shunt circuit is shown in Figure 6-5. Considering the simple case when the shunt circuit is purely passive components, the mechanical current source and the piezoelectric voltage are both sinusoidal, i.e. $i_m = I_m \sin \omega t$, $v_p = V_p \sin(\omega t + \theta)$, at the structure resonant frequency. In such a case, the vibration power is a function of velocity i_m , piezoelectric voltage v_p and their phase difference θ . More specifically, the power generated from the piezoelectric layer P_m can be expressed as:

$$P_m = \frac{n I_m V_p}{2} \cos \theta \quad (6-5)$$

where n is the electromechanical transformation ratio, which is marked in Figure 6-5.

Equation (6-5) expresses power at point "A" in Figure 6-5, which represents the power

generated from the vibration. As the mechanical current source (mechanical velocity) is assumed to be constant first, power is determined by the piezoelectric voltage v_p and the phase angle θ . In fact, the piezoelectric voltage v_p and the phase angle θ are mainly decided by the piezoelectric shunt network. For example, when the shunt circuit is set as a short-circuit, the piezoelectric voltage is zero. There is no power flowing out of the piezoelectric layer. When the shunt circuit is set as an open circuit, the mechanical current and the piezoelectric voltage have 90 degree phase difference due to the piezoelectric inherent capacitor. There is also no power flowing out of the piezoelectric layer. It should be noted that these two critical cases both cannot obtain any power/energy from the piezoelectric layer but the fundamental reasons are not the same.

To obtain the largest power out of the piezoelectric layer, a large piezoelectric voltage v_p and zero phase difference ($\theta=0$) are both required. To have zero phase difference between the velocity and the piezoelectric voltage, the topology VPR is applied. The velocity is detected at point “A” to control the active rectifier to get power factor correction as well as the rectangular work cycle. In addition, to enlarge power dissipation in the shunt damping, the resistive load of the VPR is changed to a DC voltage sink. This DC voltage sink can be adjusted to increase the piezoelectric voltage. Accordingly, the piezoelectric layer is able to generate larger power to the shunt circuit from the vibration. The damping factor can be thus increased. Similarly, as in the VPR

case, the piezoelectric voltage follows the vibration velocity. Therefore, this innovative damping technique is called velocity-controlled switching damping (VSPD). The implemented circuit of the VSPD is shown in Figure 6-6, and the operation is the same as for the VPR, it is presented in Table 6-3. It should be noted that this methodology is adapted not only for the specific frequency but for a wide frequency range. The bandwidth of the VSPD is mainly depending on the sensing observability of the sensor itself. Actually, the wider bandwidth is the key advantage of the semi-active control compared to the passive shunt circuit.

Table 6-3. The operation of the VSPD

	Mechanical current is positive	Mechanical current is negative
L1 and R2	ON	OFF
L2 and R1	OFF	ON

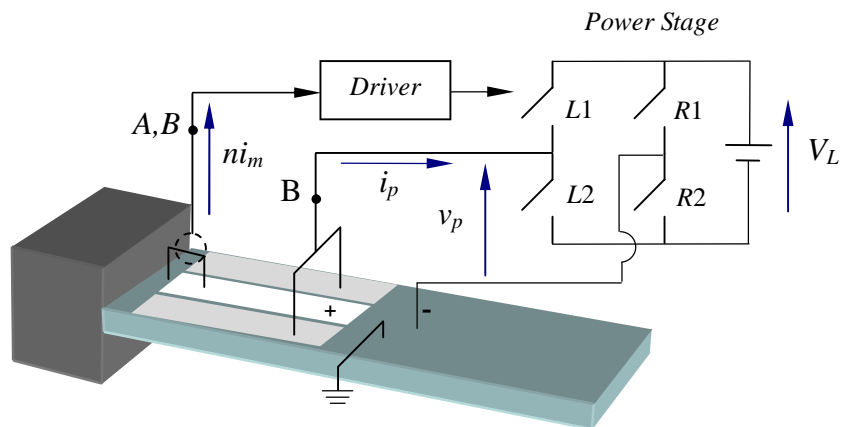


Figure 6-6. The system block diagram and circuit topology of the VSPD system

The semi-active control such as the VSPD is a nonlinear control method essentially, and it is not easy to analyze. To make the analysis more intuitive, the work cycle (or energy cycle) mentioned in last section is used to analyze the shunt circuit. To draw the work cycle, piezoelectric charge and piezoelectric voltage should be obtained from the waveforms of the mechanical current and the piezoelectric voltage. The observing point of interest is point “A” because the power at this point represents the power generated from the mechanical part. At point “A”, the average power out of the piezoelectric layer in a period can be expressed as:

$$P_r = \frac{1}{T_p} \int_0^{T_p} i_m(t) v_p(t) dt \quad (6-6)$$

Where T_p represents the period of the vibration, i.e. $T_p=1/\omega$. Accordingly, the energy flowing out of the piezoelectric in one vibration cycle layer can be expressed as:

$$E_r = P_m T_p = \int_0^{q_m(T_p)} v_p(t) dq_m(t) \quad (6-7)$$

where $q_m(t)$ represents the equivalent charge. The integration in equation (6-7) also stands for the area in the charge-voltage plane, representing the energy flowing out of the piezoelectric layer. The real energy which flows out of the piezoelectric layer is the key issue in damping design. The larger energy flows out of the piezoelectric layer, the larger the vibrating energy loss in the piezoelectric shunt circuit in each cycle. The work cycle is the trace on piezoelectric charge-voltage plane.

On the other hand, it is mentioned that the phase difference between the velocity

and the piezoelectric voltage is the key to design the shunt damping. Nevertheless, the phase difference in the charge-voltage plane is a key parameter of interest. With phase difference, a portion of the power generated from the piezoelectric layers and flowing into the shunt circuit will flow back to the piezoelectric layer. This situation corresponds to a power factor smaller than 1. However, equation (6-7) has only the information on the real power but no information on the apparent power. To obtain the apparent power P_a , the velocity and the piezoelectric voltage are put in phase:

$$P_a = \frac{1}{T_p} \int_0^{T_p} i_m(t) v_p(t-t_0) dt \quad (6-8)$$

where t_0 is the time delay between the piezoelectric voltage and the velocity at the fundamental frequency. The area of the work cycle, i.e. the corresponding energy form, can be written as:

$$E_a = P_a T = \int_0^{q_m(T)} v_p(t-t_0) dq_m(t) \quad (6-9)$$

According to the definition of the power factor, PF ,

$$PF = \frac{P_r}{P_a} = \frac{E_r}{E_a} \quad (6-10)$$

In summary, there are two work cycles in the charge-voltage plane. One cycle tracks for the real power and the other cycle tracks for the apparent power. The areas of the work cycles represent the corresponding energy flows in one vibration period and the area ratio between the two work cycles represents the power factor.

The typical resonant shunt damping circuit [39] shown in Figure 6-7 is examined

by the work cycle first. It is known that the resonant shunt damping topology has good performances only when the inductor-capacitor electrical resonant frequency matches with the mechanical resonant frequency of the structure. When the mechanical and electrical resonant frequencies are mismatch, the work cycles are shown in Figure 6-8(a). We can see that the power factor in this case is poor. However, when the mechanical frequency and the electrical resonant frequency are close to each others, the areas of the apparent work cycle and the real work cycle are almost equal (Figure 6-8 (b)). Specifically, good power factor leads to good performances, this is due to the power does not flow back to the piezoelectric layer. Typical resonant shunt damping circuit uses the inductor to compensate the contribution of the piezoelectric intrinsic capacitance, but only at the resonant frequency. This is the underlying reason why the resonant shunt damping only has good performances with small bandwidth near the resonant frequency. Most importantly, the work cycle observation is really an effective way to examine the damping performances.

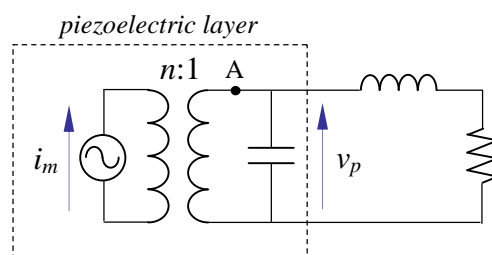


Figure 6-7. The piezoelectric resonant shunt damping topology

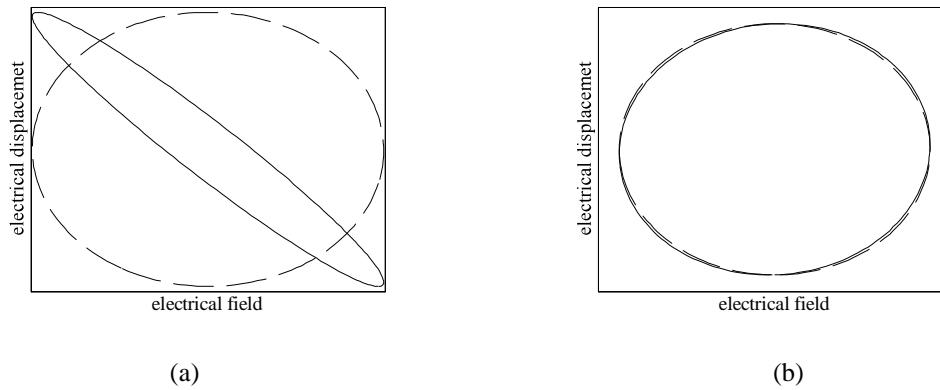


Figure 6-8. The work cycle of the piezoelectric resonant shunt damping topology (a) mismatches the resonant frequency (b) matches the resonant frequency (solid line: the apparent work cycle; dotted line: the real work cycle)

There are three conclusions we can get from the work cycles analysis to evaluate the performances of a damping circuit.

1. The maximum power transfer out of the piezoelectric layer can be described as maximum area of the real work cycle, which is actually squared shape in the charge-voltage plane.
2. The optimum damping situation corresponding to the area ratio of two work cycles is equal to one, and the corresponding power factor should also be one.
3. In the whole controllable bandwidth, the power factor should be always equal to 1 in all frequencies within the bandwidth.

Actually, the VSPD technique can fit all these three requirements well. The work cycle of the VSPD is rectangular because of the waveforms of the velocity and the voltage are sinusoidal and squared respectively (Figure 6-4). The rectangular work cycle will have

the maximum area under the same physical limitations. Furthermore, the power factor of the VSPD is equal to one in all frequencies range due to the piezoelectric voltage always follow the phase of the velocity. The ideal work cycle of the VSPD is shown in Figure 6-9. The work cycles of the apparent power and the real power are both squared and overlapping well even though the frequency may vary. In other words, the VSPD system has the optimal energy cycle, and is the best semi-active damping method. From the viewpoint of power electronics, VSPD is actually a power factor correction circuit to force the power factor to be one.

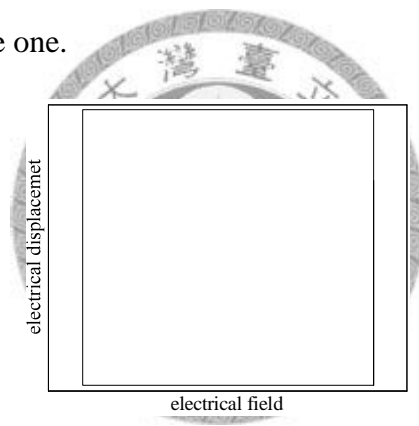


Figure 6-9. The work cycles (the apparent work cycle and the real work cycle overlapping) of VSPD

6.3 Analysis of Velocity-Controlled Switching Piezoelectric Damping

To connect the VSPD system to the structure, the single-mode governing equation of the structure with piezoelectric layers is mentioned in chapter 2 re-written here:

$$M\ddot{u} + D\dot{u} + Ku = f - nv_p \quad (6-11)$$

$$i_p = n\dot{u} + C_p \dot{v}_p \quad (6-12)$$

where u represent the displacement, which is only related to the temporal domain, *i.e.*

$u=u(t)$.

Three cases are discussed:

1. Short circuit state

In short circuit state, i.e. $v_p=0$, the dynamic of the structure can easily be expressed in frequency domain:

$$\left. \frac{u}{f} \right|_{short} = \frac{1}{K - M\omega^2 + jD\omega} \quad (6-13)$$

$$\omega_r = \sqrt{\frac{K}{M}} \quad (6-14)$$

$$U_M = \frac{F_M}{D\omega} \quad (6-15)$$

where ω_r is the resonant angular frequency in the short circuit state. F_M and U_M represent the amplitude of the external force and the amplitude of the displacement at resonant frequency respectively.

2. Short circuit state

Similarly, in open circuit state, the current out of the piezoelectric layer is equal to zero, i.e. $i_p=0$. Substituting equations (6-11) into equation (6-12), the dynamics of the structure can be written as:

$$\left. \frac{u}{f} \right|_{open} = \frac{1}{K + \frac{n^2}{C_p} - M\omega^2 + jD\omega} \quad (6-16)$$

$$\omega_r = \sqrt{\frac{K + n^2 / C_p}{M}} \quad (6-17)$$

$$U_M^{open} = \frac{F_M}{D\omega} \quad (6-18)$$

3. VSPD technique

In the case of VSPD, the voltage on the piezoelectric layer is determined by the switching circuit. More specifically, the piezoelectric voltage is closed to squared waveform and the amplitude is based on the connected DC voltage. According to Fourier theory, the first harmonic of the waveform in VSPD is:

$$v_p = \frac{4}{\pi} V_{DC} \sin(\pi d) \text{signe}(\dot{x}) \quad (6-19)$$

where d is the duty cycle of the VSPD switches. It should be noted that the piezoelectric voltage follows the velocity, so the term $\text{signe}(\dot{x})$ is added in equation (6-19). Substituting equation (6-19) into equation (6-11) and writing it in the frequency domain leads:

$$(K - M\omega^2)u + jD\omega u = f - jn \frac{4}{\pi} V_{DC} \sin(\pi d) \quad (6-20)$$

At resonant frequency, the displacement of VSPD is:

$$U_M^{VSPD} = \frac{F_M - n \frac{4}{\pi} V_{DC} \sin(\pi d)}{D\omega} \quad (6-21)$$

Compared with equation (6-22) and equation (6-15), the theoretical attenuation of the displacement can be obtained:

$$A_{VSPD} = 20 \log_{10} \left(1 - n \frac{4}{\pi} \frac{V_{DC}}{F_M} \sin(\pi d) \right) \quad (6-22)$$

According to equation (6-22), it can be noticed that the vibration is possibly cancelled

out totally if the DC sink V_{DC} is set properly. However, when the V_{DC} is set too large, equation (6-22) is no longer correct. The limitation of the DC sink voltage is:

$$V_{DC} \leq \frac{\pi}{4n} \frac{F_M}{\sin(\pi d)} \quad (6-23)$$

Under this maximum dc voltage limitation, the DC voltage works like a sink. However, once the dc voltage is set above the maximum value, it works like a source. The voltage source will excite the vibration of the structure. The piezoelectric layer becomes actuator but no longer a damper. The theoretical analyses are summarized in Table 6-4.

Another semi-active damping technique, SSDV (synchronous switching damping on a voltage source), is also listed in Table 6-4 to compare with the VSPD technique.

Table 6-4. Comparison between SSDV and VSPD techniques.

	SSDV [43, 44]	VSPD
Topologies		
Dissipated energy	$\frac{1 + \gamma}{1 - \gamma} \left(\frac{4n^2}{C_p} u_M^2 + 4nu_M V_{DC} \right)$	$4nV_{DC}u_M$
Operating rules	<p>SP “ON”: when minimum displacement occur</p> <p>SN “ON”: when minimum displacement occur</p> <p>SP & SN are both “OFF”: else</p>	<p>L1&R2 “ON”: positive mechanical current</p> <p>L1&R2 “OFF”: negative mechanical current</p>

Work cycles	parallelogram	rectangular
Maximum voltage	$\frac{\pi}{4n} \frac{1+\gamma}{1-\gamma} F_M$	$\frac{\pi}{4n} \frac{F_M}{\sin(\pi d)}$

6.4 Experiment Setup

The experimental structure under test is a cantilever steel beam. The beam was excited by an electromagnetic shaker at the fix end of the beam. Two 31-type piezoelectric ceramic layers were bonded on the beam. A displacement sensor was set to measure the displacement at the free end of the beam. The signal from the displacement sensor is used in the signal processor to synchronize the switching signal of the shunt circuit. The detailed experimental setup is shown in Figure 6-10. Table 6-5 shows the dimension of the beam and the piezoelectric layers and Table 6-6 arranges the model parameters. It should be mentioned that, the parameters in first row of Table 6-6 were measured, and the third row can be calculated by the first two rows. The detailed relationships between the measured data (first row) and the corresponding model parameter (third row) are arranged in the last row of Table 6-6.

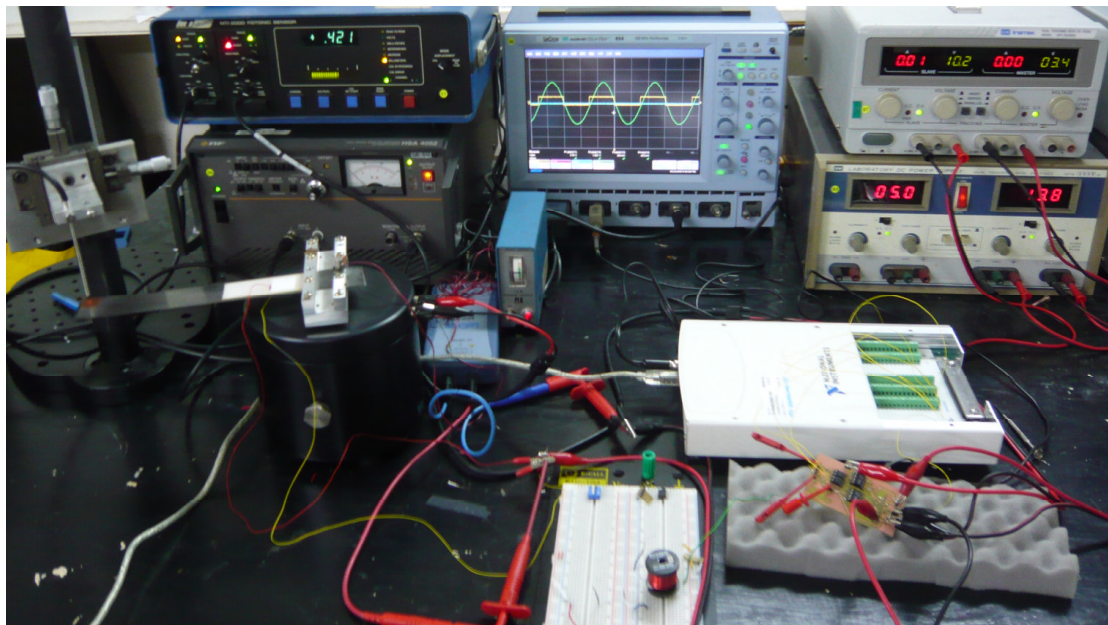
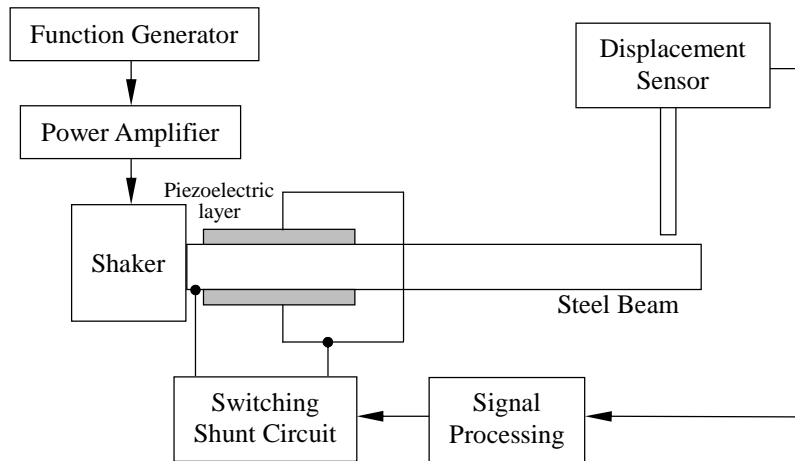


Figure 6-10. Experimental setup of the piezoelectric switching damping

Table 6-5. The piezoelectric layer and Steel Beam

	Steel Beam	Piezoelectric layer
length	242.3mm	70mm
width	35mm	30mm

thickness	0.5mm	0.7mm
Location	none	2mm from fixed end

Table 6-6. The model parameters of the piezoelectric/beam system

f_{short}	f_{open}	ζ	C_p	λ
16.4Hz	16.5Hz	0.0154	81nF	2467Vm ⁻¹
k^2	n	K	M	D
0.0122	0.0004212 NV ⁻¹	180Nm ⁻¹	16.9g	0.0538Nm ⁻¹ s ⁻¹

Definitions:

1. measured data

- 1) f_{short} : short circuit resonant frequency (Hz)
- 2) f_{open} : open circuit resonant frequency (Hz)
- 3) ζ : short circuit resonant frequency
- 4) C_p : piezoelectric inherent capacitor (nF)
- 5) λ : The ratio between the free end displacement and open circuit voltage (Vm⁻¹)

2. calculated data

- 1) $k^2 = \frac{f_{open}^2 - f_{short}^2}{f_{short}^2}$: the square of electromechanical coupling factor
- 2) $n = \lambda C_p$: electromechanical ratio (NV⁻¹)
- 3) $K = \frac{n\lambda}{k^2}$: modal stiffness (Nm⁻¹)

$$4) \quad M = \frac{K}{4\pi^2 f_{short}^2} \text{ (kg)}$$

$$5) \quad D = 4\pi\zeta M f_{short}^2 \text{ (Nm}^{-1} \text{ s}^{-1}\text{)}$$

The experimental results are shown in Figure 6-11. The DC voltages of the VSPD testing system were set at 0V, 5V, 10V, 15V and 17V. In Figure 6-11, it can be seen that when the voltage increases, the attenuation increases as well. The displacement can be cancelled effectively in the case of 17V DC sink from 3.7mm to 1.2mm. The residual displacement is closed to the vibration in the non-resonant state. The last DC voltage was set at 17V because the experimental maximum voltage is around 17.4V. Once the DC voltage was set exceeding 17.4 V, the VSPD system is no longer a damper but an actuator. The displacement amplitude rises again after the maximum voltage reached. The experimental waveform of the VSPD system with DC voltage is set to 17V at resonance frequency and shown in Figure 6-12(a). In Figure 6-12(a), the displacement signal and the piezoelectric voltage are sinusoidal and squared waveform respectively.

We can see that the piezoelectric voltage and the displacement have a 90 degree phase difference. The underlying reason is that the piezoelectric voltage follows the vibration velocity, and the displacement and the velocity are in 90 degree phase difference generally. Putting the displacement waveform and the piezoelectric voltage together, the work cycle has been plotted in Figure 6-12(b). As our design predicted, the

work cycle is rectangular. The VSPD system indeed owns the optimal work cycle. Furthermore, according to equation (6-22) and model parameters in Table 6-6, the attenuation of the vibration at open circuit resonant frequency, 16.5 Hz, was calculated and plotted in Figure 6-13. In Figure 6-13, the experimental results match the theoretical result quite well. The predicted curve in Figure 6-11 can be completed to Figure 6-14. Some more experimental points were plotted at different frequencies (16.3Hz, 16.4Hz, 16.5Hz), and the experimental maximum voltage 17.4 V has been plotted in Figure 6-14. It should be noted that there is an extreme point where is situated the theoretical boundary value of the DC maximum voltage. The theoretical maximum DC voltage is 17.9V, which is close to the predicted maximum DC voltage, 17.4V.

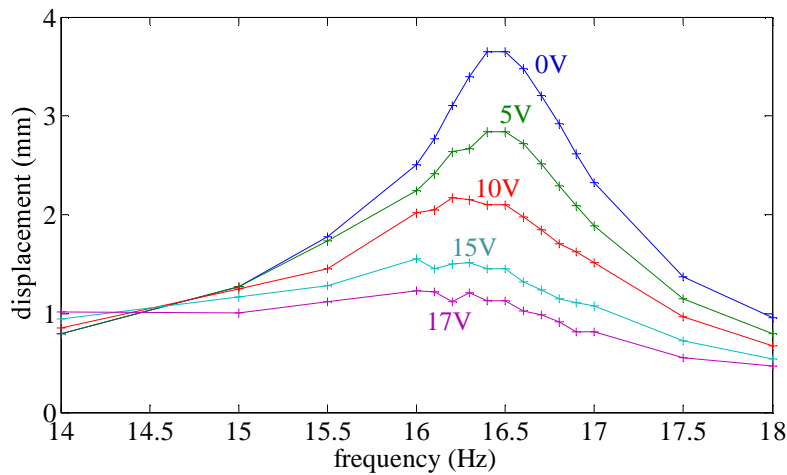


Figure 6-11. The frequency response the VSPD system

(a) the displacement and the voltage waveforms (b) the work cycle

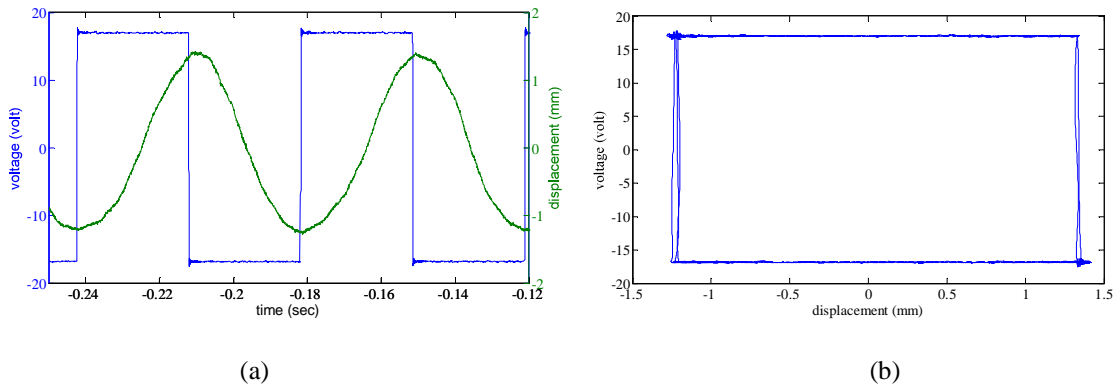


Figure 6-12. The experimental waveform of the VSPD system (a) the displacement and the voltage waveforms (b) the work cycle

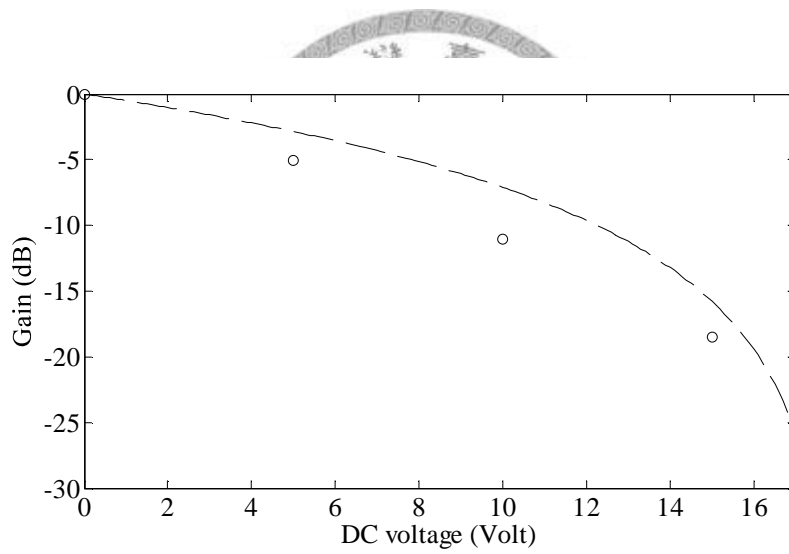


Figure 6-13. The experimental results (points) and the theoretical prediction (line) of the VSPD

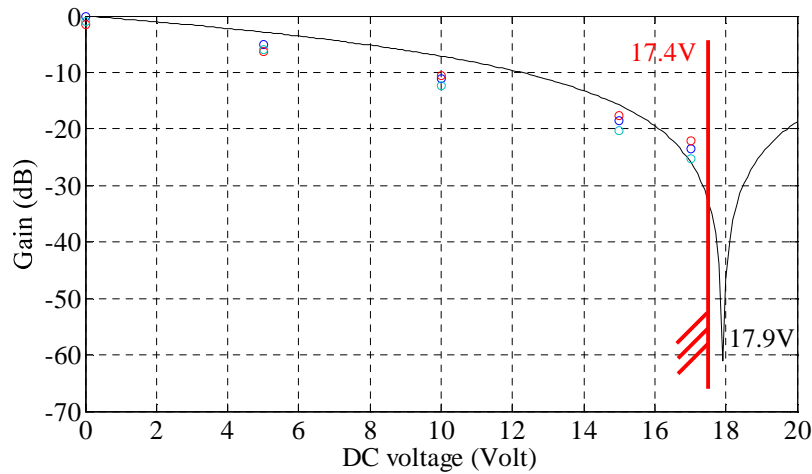
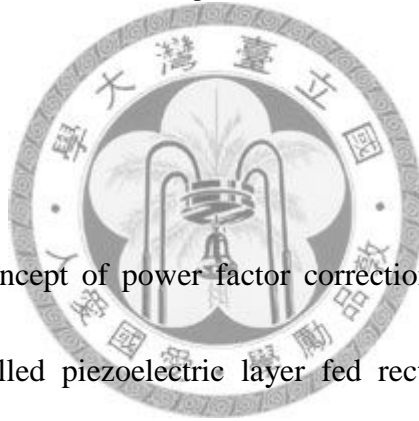


Figure 6-14. The experimental results (points) and the theoretical prediction (line) of the maximum dc voltage (Red points: 16.6Hz, Blue points: 16.5Hz, Green points: 16.4Hz)



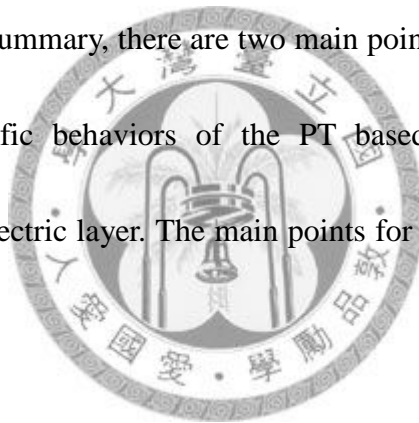
6.5 Summary

According to the concept of power factor correction and the rectangular work cycle, the velocity controlled piezoelectric layer fed rectifier was proposed in this chapter. The concept of VPR can be applied to the semi-active damping, which is called velocity controlled piezoelectric switching damping (VSPD). The theoretical prediction and the experimental results of the VSPD were both demonstrated in this chapter and were proved as an effective damping technique. The displacement at resonance was suppressed 23dB at the resonance, and the final suppressed displacement was closed to the displacement at non-resonance.



Chapter 7. Summary and Discussion

The theoretical prediction and the design procedure of two piezoelectric transformers (PT) based converters: the CCFL inverter and the DC/DC converter were detail in chapter 4 and chapter 5 respectively. The selection of circuit topology of the PT based DC/DC converter and the specific conducted EMI behavior of PT based DC/DC converter also demonstrated in chapter 5. The work cycle of the piezoelectric layer were detailed and thus derived the piezoelectric layer fed rectifier which applied to the vibration control. In brief summary, there are two main points of this dissertation: 1) the design rule and its specific behaviors of the PT based converter, 2) the energy optimization of the piezoelectric layer. The main points for the PT designer are detailed in the following sections.



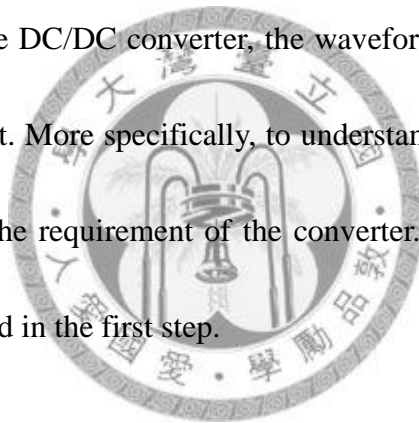
7-1. The Systematic Design Rule for the PT Based Converter

In this dissertation, the complete design procedure of the piezoelectric transformer based CCFL inverter, piezoelectric transformer based DC/DC converter and the piezoelectric layer fed velocity controlled rectifier were full developed. One of the main points in this dissertation is that the typical optimal loading condition should not be a design criterion but the mechanical current is the key to the design the piezoelectric transformer. The dimensional parameters of the piezoelectric transformers can change

power curve significantly which are the major design factor to the piezoelectric transformer. According to the previous chapters 3, 4 and 5, we can summarize a general design procedure as follows:

1. Examine the load characteristics.

For example, in the case of CCFL, we understand its negative increment impedance and crest factor to understand the suitable waveforms and the power tendency. In the case of the DC/DC converter, the waveform at the PT output terminal was discussed in detail first. More specifically, to understand the load characteristics of the load is to understand the requirement of the converter. This is the most important thing and should be checked in the first step.



2. Examine the relationship between the mechanical current and the load characteristics.

As different PTs has some equivalent circuit, the relationship between the mechanical current and the load variation can be found by the equivalent circuit first. Since the load characteristics have been understood in the first step, in this step we can know the required mechanical current of the PT. Furthermore, according to the load characteristics, we can also know which kind of the piezoelectric transformer should be

adopted. For example, in the application of high voltage/low current application, we may only need single-layer piezoelectric transformer. In the application of low voltage/high current application, the multi-layer piezoelectric transformers are preferred. This step is usually strait-forward as long as the load characteristics have already understood well.

3. Connect the equivalent circuit to the dimensional parameters

Although the equivalent circuit components can help designer have an institutive concept to understand the requirement of the PT. However, the equivalent circuit components are virtual components. The dimensional parameters are practical design parameters for the PT designer. Different PT configurations have the different relationship between the equivalent circuit and the dimensional parameters although their equivalent circuit topologies are the same. This step can give the PT designer a basic view to choose the proper size of the PT.

4. Adjust the proper dimension and efficiency

Designers can be found that the dimension and the efficiency of the piezoelectric transformers are trade-off. More specifically, the larger PT leads to the higher efficiency but the smaller PT leads to the smaller efficiency. We can adjust the dimension and the

required efficiency according to the application. This point is similar to the electromagnetic components, *i.e.* the inductor of the larger size can endure larger current in general.

5. *Check the ZVS condition can be achieved*

The half-bridge driving with a series inductor can achieve the ZVS condition in fixed load impedance. When the load varies, the ZVS condition may not be achieved again according to the phase between the switch voltage and switch current are varied with the load condition. Since the burst-mode control was adopted in this dissertation, the equivalent load value is almost a constant when the PT passing through the energy. The ZVS condition can be kept well change in the steady state. Normally, the ZVS condition is design at heavy load condition or typical operating points since the efficiency of these two conditions are most important. The choice of the series inductor was detail in chapter 3. The resonant frequency of the input LC resonant tank formed by the series inductor and the PT input capacitor is better set between the PT resonant frequency and PT following parasitic resonant frequency.

6. *Make the feedback controller*

The burst mode control is good control method for the PT, since it can keep the PT

efficiency as well as the ZVS condition. However, it may sacrifice the dynamics range of the converter. The hysteretic burst-mode control method was thus adopted. If the PTs were designed properly, the controller is quite easy to fit the requirement. It mentioned that the typical PWM control is not good for the PT since the variation of the duty cycle would excite the useless inefficient vibration mode of the PT. Another possible control method is the variable frequency control such as PFM (pulse frequency modulation) control. However, we did not detailed in this dissertation since this dissertation focus on the fixed frequency control method.

7. *Conclusion for the proposed design rule*

The steps mentioned above are general for each PT based converters. The analysis and the experimental results shown in this dissertation indicated that the typical optimal loading condition method is only suitable for the fixed load value. The design based on the mechanical current can improve efficient under the case of the load variation.

7-2. Examine the power density of the piezoelectric layer

There were several interface circuit of the piezoelectric proposed, including the application of the shunt dampers, harvesters and the piezoelectric transformers. However, it is not easy to compare the performance of the all the interface circuit their

performance, especially in the case of non-linear interface circuits. Chapter 7 mentioned the work cycle in this paper is the most efficient way to analyze the performance. The steps to analyze the energy from piezoelectric layer are summarized as follows:

1. Find out the waveform of the displacement and the waveform of the piezoelectric voltage

In the single frequency exciting system, the displacement is usually sinusoidal-like, especially in the low coupling system. The piezoelectric voltage is mainly based on the interface circuit. In the case that the interface circuit only includes the passive components, the voltage is sinusoidal. In the case of the rectifier or the switching circuit, however, it could be any kind waveform. Since the waveforms of the displacement and the voltage are the easiest measured waveform, which is good to use to analyze the work cycle although the energy can be in terms of other physical parameters. Once these two waveforms are discovered, the “shape” of the waveform can be explored.

2. Examine the relationship between the displacement and the piezoelectric voltage

Although the shape of the work cycle was checked in the first step, but most important thing is to know is the area of the work cycle since it represents the real energy from the piezoelectric layer. To make it intuitively, only one parameter, such as

displacement was used. Once the relationship between the displacement and the piezoelectric voltage was discovered, the area of the work cycle can be discovered as mentioned in chapter 7.

7-3. The future works

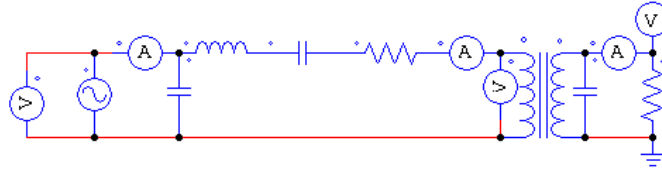
Since the design procedure and the energy analysis in this dissertation of the piezoelectric transformer were fully developed. Since the mechanical current is the basic physical limitation of the PT, so increasing the PT output current is a very important topic in the future. There are several possible ways to increase the PT output current:

1. Change the vibration type, such as the shear-mode vibration which has the possibility to own the larger electromechanical coupling than in-plane vibration. [46, 47, 48]
2. Improve the material properties has the potential to increase the output current. The single crystal piezoelectric material has better characteristic than PZT material. [49]
3. Piezoelectric transformer parallel techniques. Parallel the PTs can increase the PT output current. However, the paralleled PTs may have the interaction. It is an important and interesting topic. [50]

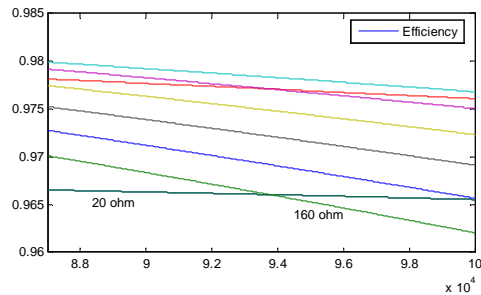
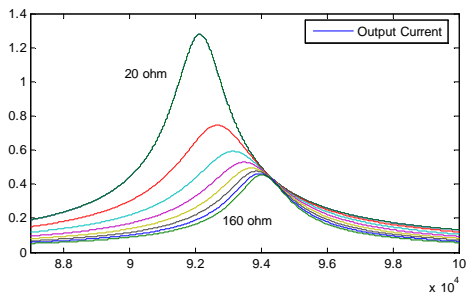
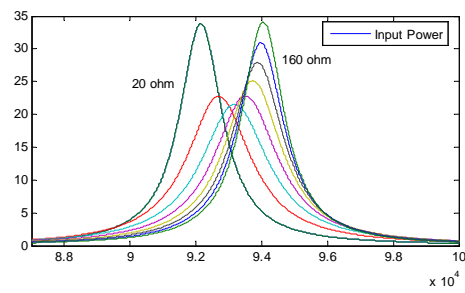
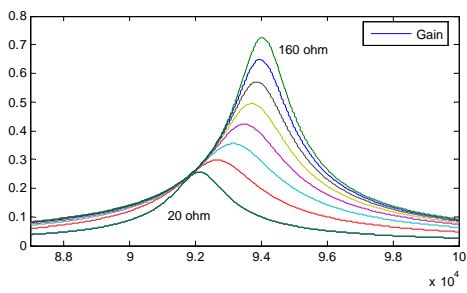


Appendix A. Work Cycles in Different Circuit Topologies

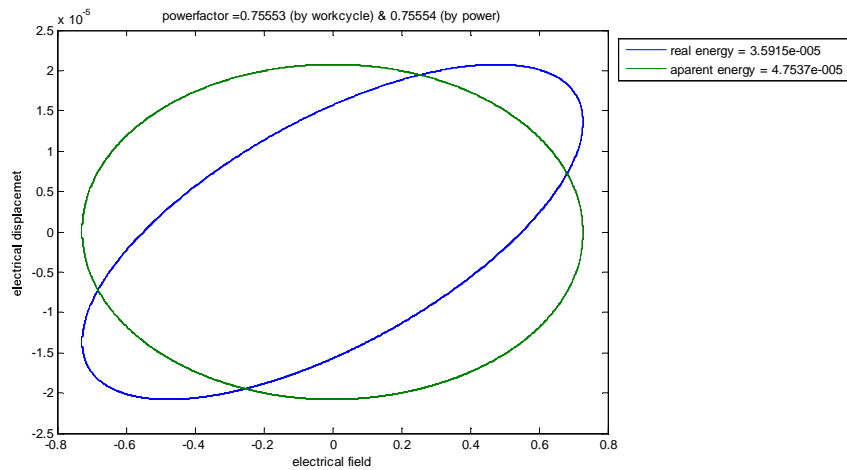
Case 1. pure resistive load:



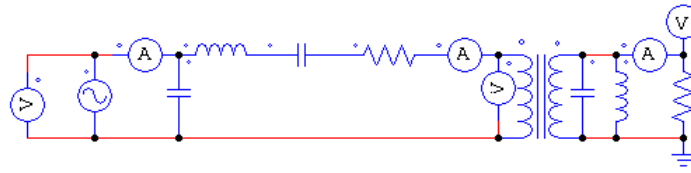
Characteristics:



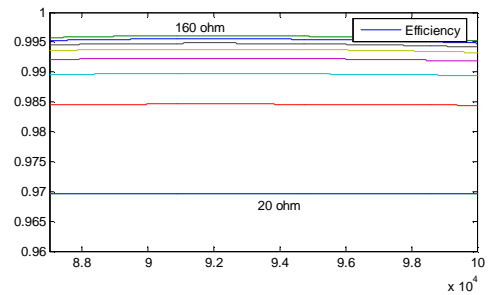
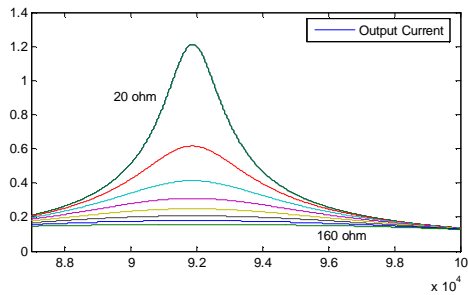
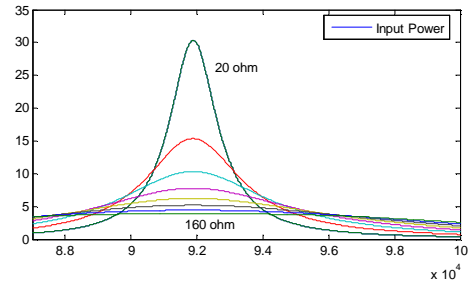
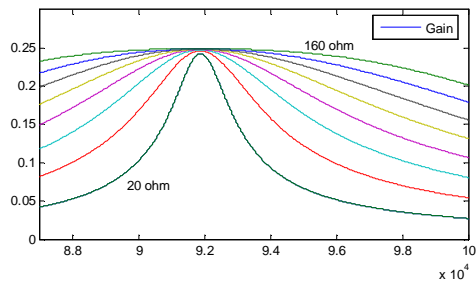
work cycle & power factor:



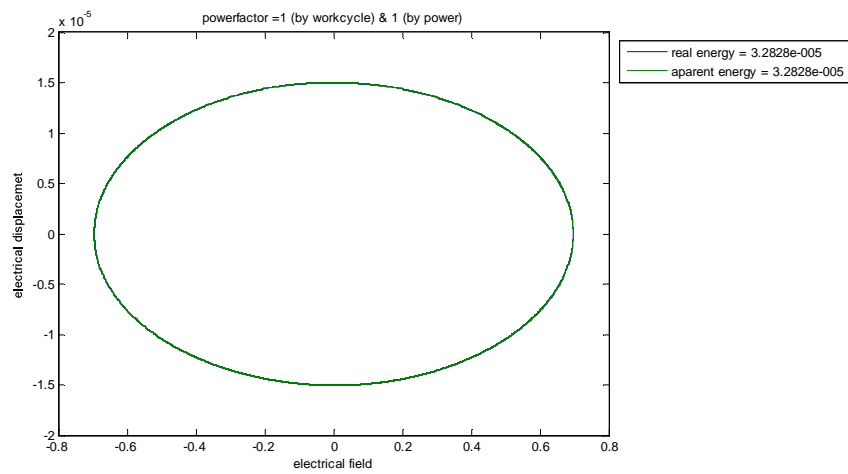
Case 2. parallel inductor with resistive load:



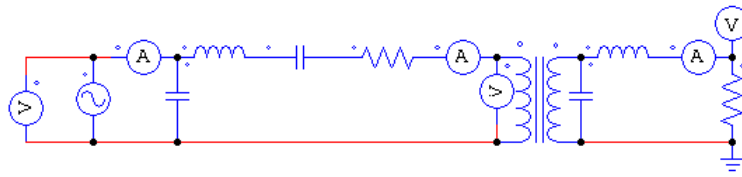
Characteristics:



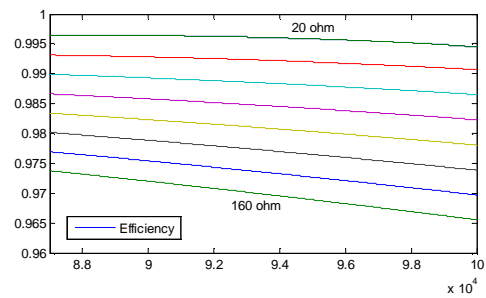
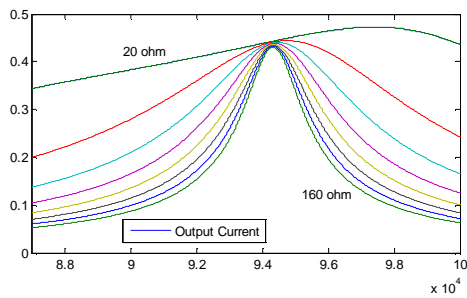
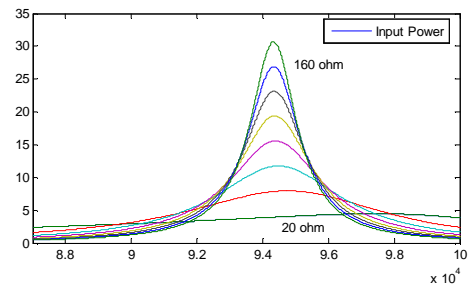
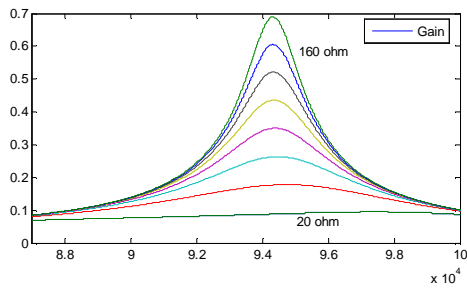
work cycle & power factor:



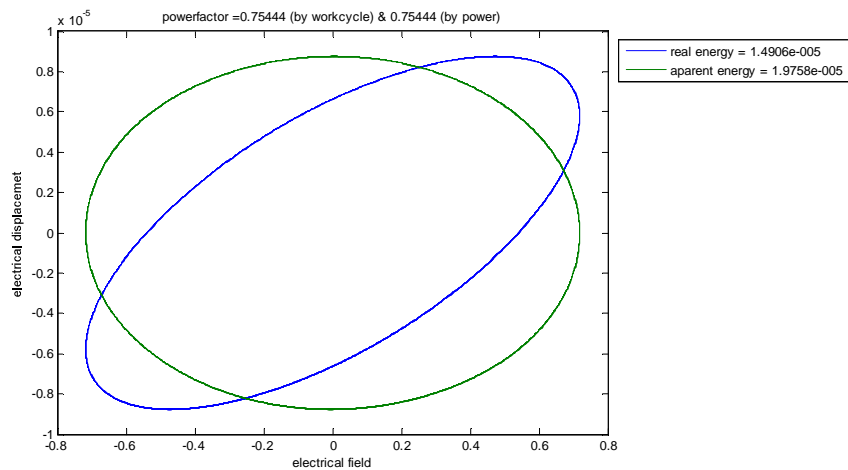
Case 3. series inductor with resistive load:



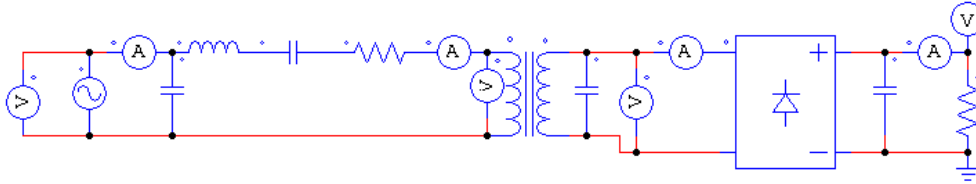
Characteristics:



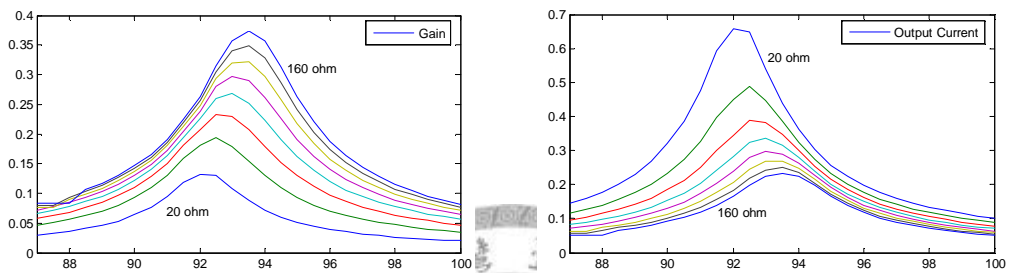
work cycle & power factor:



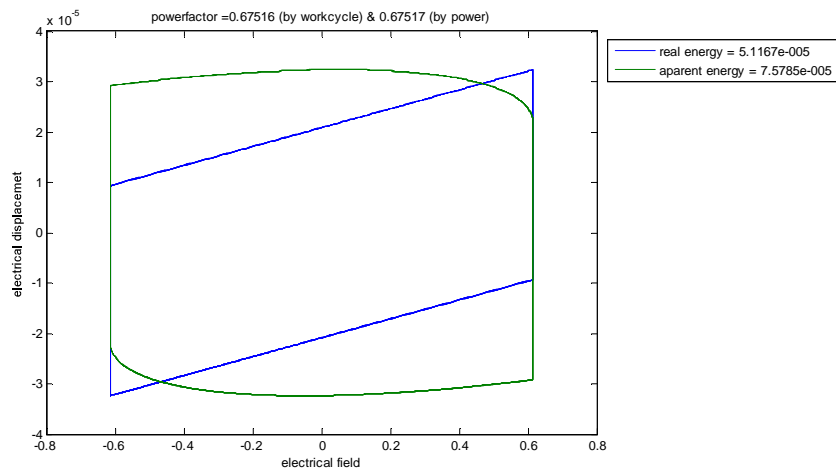
Case 4. voltage mode rectifier:



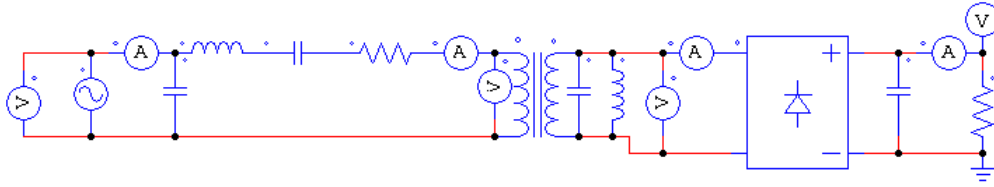
Characteristics:



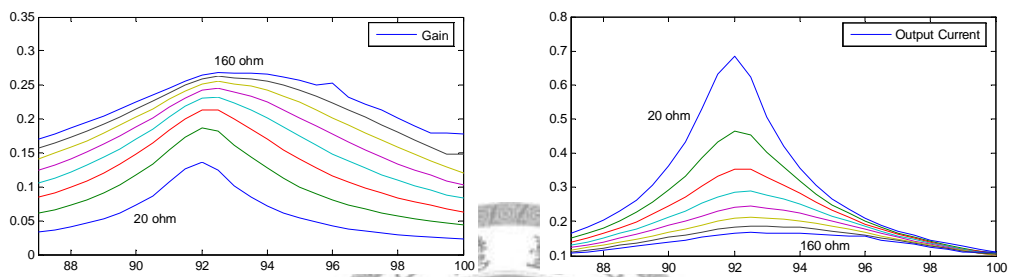
work cycle & power factor:



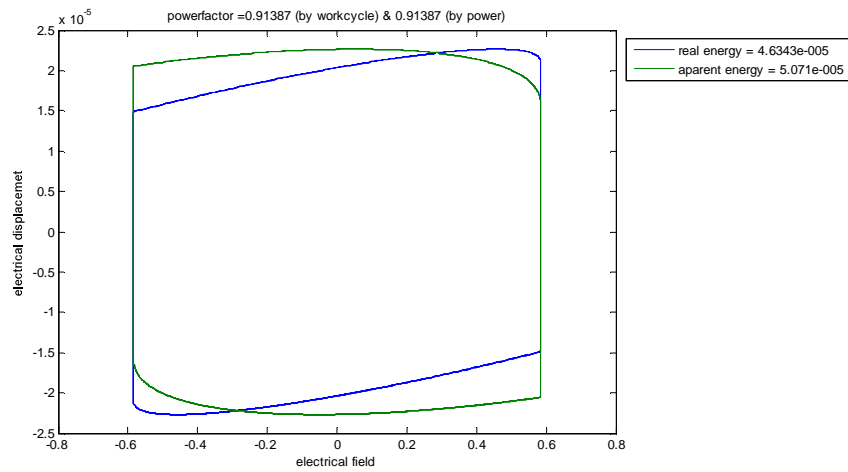
Case 5. parallel inductor before the rectifier:



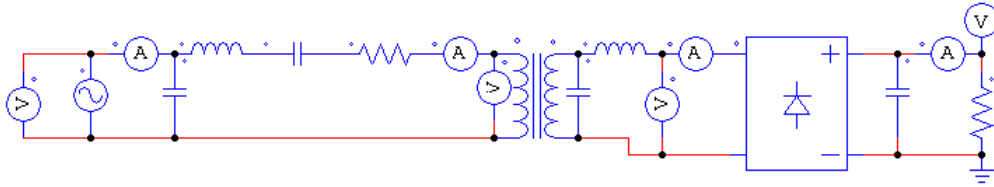
Characteristics:



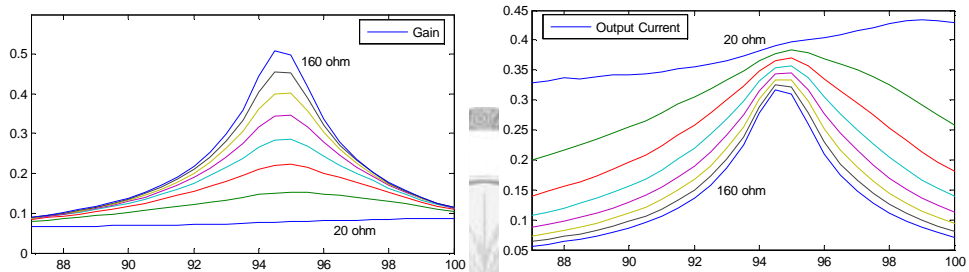
work cycle & power factor:



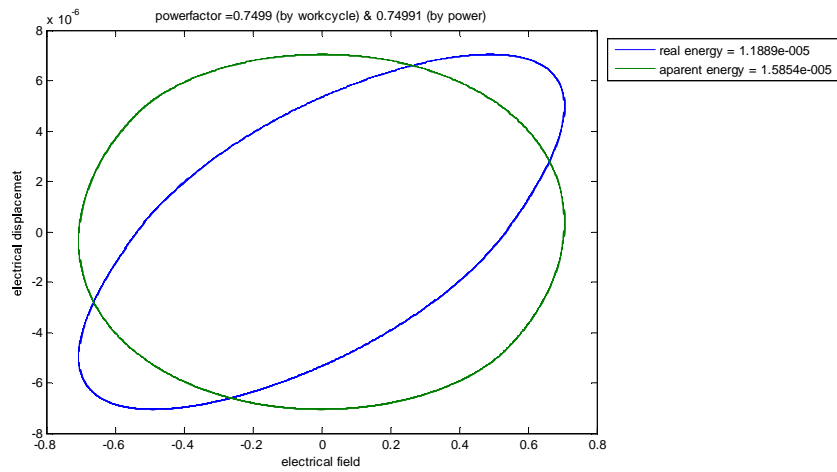
Case 6. series inductor before the rectifier:



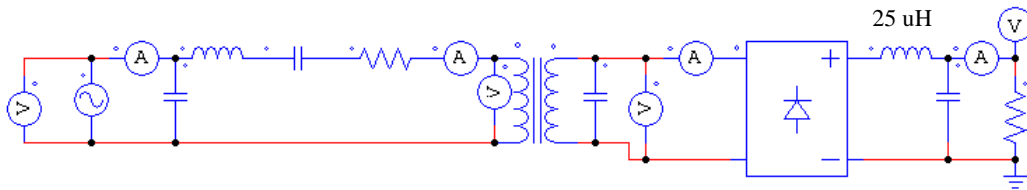
Characteristics:



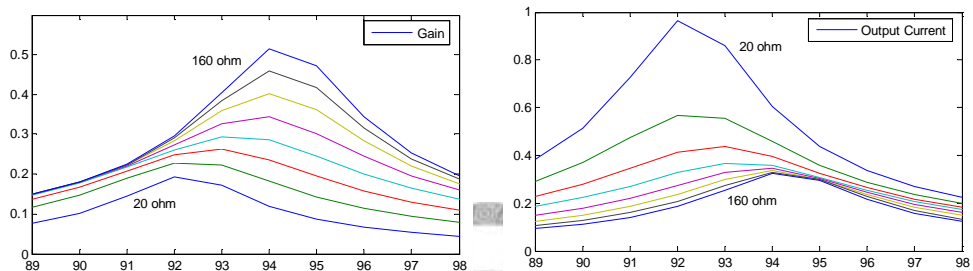
work cycle & power factor:



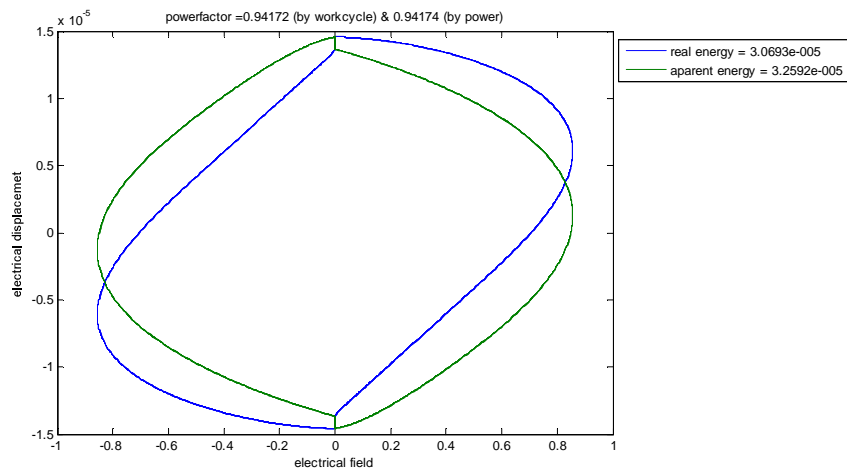
Case 7. series inductor after the rectifier:



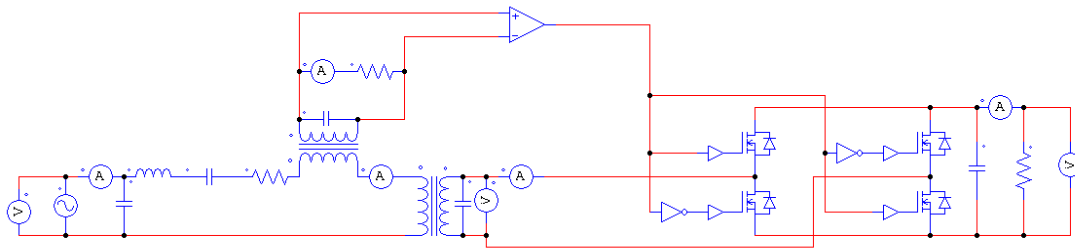
Characteristics:



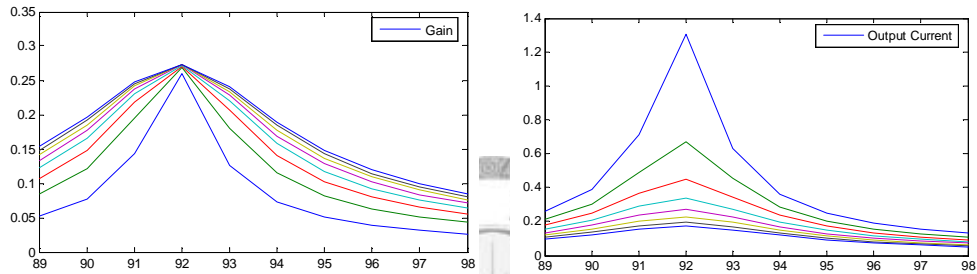
work cycle & power factor:



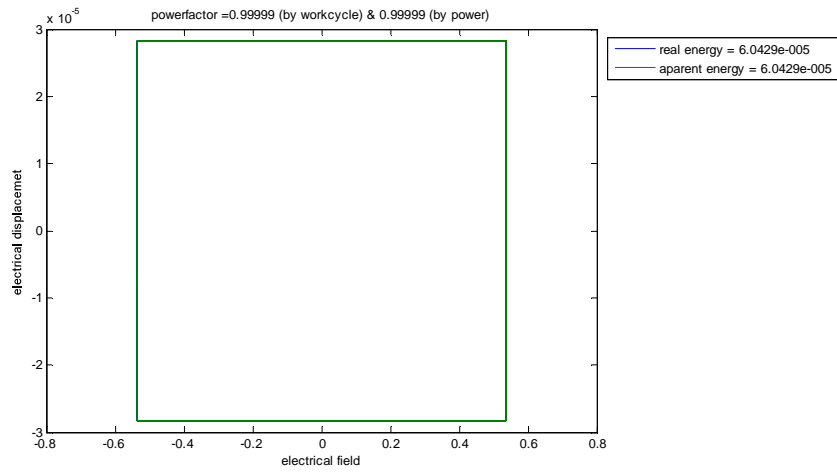
Case 8. velocity controlled rectifier:



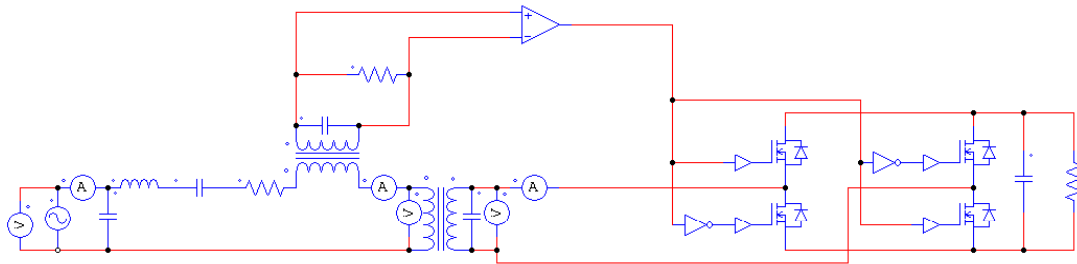
Characteristics:



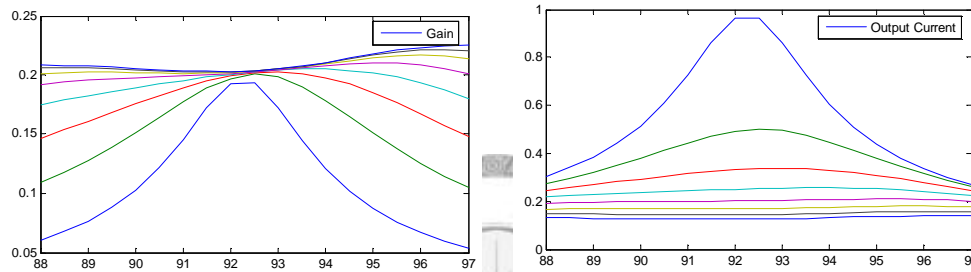
work cycle & power factor:



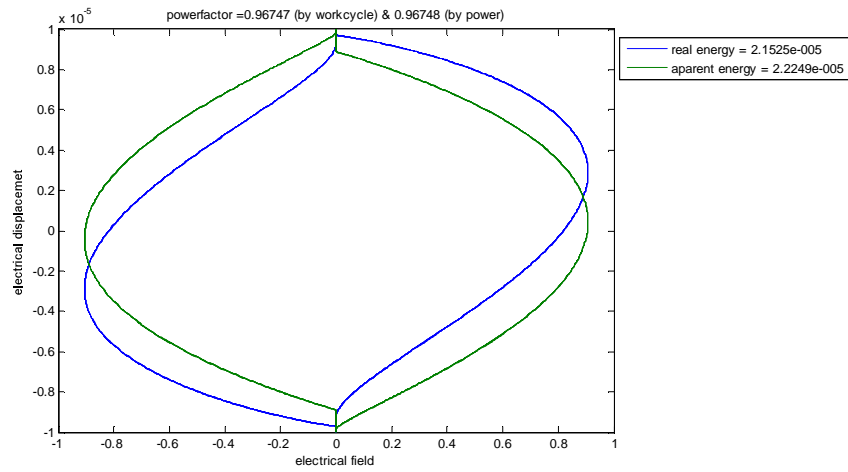
Case 9. velocity controlled rectifier with the inductor:



Characteristics:



work cycle & power factor:



Reference

- [1] C.A. Rosen, "Piezoelectric Transformers," *United States Patent*, Patent number 2,830,274, 1958.
- [2] G. Ivensky, I. Zafrany, and S. Ben-Yaakov, "Generic operational characteristics of piezoelectric transformers," *IEEE Transactions on Power Electronics*, vol. 17, no. 6, pp. 1049-1057, 2002.
- [3] Y. H. Hsu, C. K. Lee, and W. H. Hsiao, "Optimizing piezoelectric transformer for maximum power transfer," *Smart Materials & Structures*, vol. 12, no. 3, pp. 373-383, 2003.
- [4] K. Uchino, and S. Hirose, "Loss mechanisms in piezoelectrics: How to measure different losses separately," *IEEE Transactions on Ultrasonics Ferroelectrics and Frequency Control*, vol. 48, no. 1, pp. 307-321, Jan, 2001.
- [5] K. Uchino, J. H. Zheng, Y. H. Chen et al., "Loss mechanisms and high power piezoelectrics," *Journal of Materials Science*, vol. 41, no. 1, pp. 217-228, Jan, 2006.
- [6] M. Yamamoto, Y. Shimada, Y. Sasaki et al., "A multilayered piezoelectric transformer operating in the third order longitudinal mode and its application for an inverter," *IEICE Transactions on Electronics*, vol. E85C, no. 10, pp.

1824-1832, Oct, 2002.

- [7] Y. T. Huang, C. K. Lee, and W. J. Wu, "High-powered backlight inverter for LCD-TVs using piezoelectric transformers," *Journal of Intelligent Material Systems and Structures*, vol. 18, no. 6, pp. 601-609, 2007.
- [8] Y. T. Huang, W. J. Wu, Y. Y. Chen et al., "A modal actuator-based single-layer piezoelectric transformer for coilless soft switching inverters," *Smart Materials & Structures*, vol. 16, no. 6, pp. 2046-2055, Dec 2007.
- [9] Y. T. Huang, W. J. Wu, Y. C. Wang et al., "Multilayer modal actuator-based piezoelectric transformers," *IEEE Transactions on Ultrasonics Ferroelectrics and Frequency Control*, vol. 54, no. 2, pp. 359-367, 2007.
- [10] Y. K. Lo, and K. J. Pai, "Feedback design of a piezoelectric transformer-based half-bridge resonant CCFL inverter," *IEEE Transactions on Industrial Electronics*, vol. 54, no. 5, pp. 2716-2723, Oct, 2007.
- [11] C. Y. Lin and F. C. Lee, "Design of a Piezoelectric Transformer Converter and Its Matching Networks," *PESC 94 Record - 25th Annual IEEE Power Electronics Specialists Conference*, vol. 1, pp. 607-12, 1994
- [12] C. Y. Lin, "Design and analysis of piezoelectric transformer converters," *Ph.D. dissertation*, Polytechnic Institute and State University., Blacksburg, 1997.
- [13] G. Ivensky, S. Bronstein, and S. Ben-Yaakov, "A comparison of piezoelectric

- transformer AC/DC converters with current doubler and voltage doubler rectifiers,”
IEEE Transactions on Power Electronics, vol. 19, no. 6, pp. 1446-1453, Nov, 2004.
- [14] G. Ivensky, M. Shvartsas, and S. Ben-Yaakov, “Analysis and modeling of a voltage doubler rectifier fed by a piezoelectric transformer,” *IEEE Transactions on Power Electronics*, vol. 19, no. 2, pp. 542-549, Mar, 2004.
- [15] A. M. Flynn, and S. R. Sanders, “Fundamental limits on energy transfer and circuit considerations for piezoelectric transformers,” *IEEE Transactions on Power Electronics*, vol. 17, no. 1, pp. 8-14, Jan, 2002.
- [16] D. Guyomar, C. Magnet, E. Lefeuvre et al., “Power capability enhancement of a piezoelectric transformer,” *Smart Materials & Structures*, vol. 15, no. 2, pp. 571-580, Apr, 2006.
- [17] C. H. Park, "Dynamics modelling of beams with shunted piezoelectric elements," *Journal of Sound and Vibration*, vol. 268, pp. 115-129, 2003.
- [18] P. Laoratanakul, A. V. Carazo, P. Bouchilloux, and K. Uchino, "Unipoled disk-type piezoelectric transformers," *Japanese Journal of Applied Physics Part 1-Regular Papers Short Notes & Review Papers*, vol. 41, pp. 1446-1450, Mar 2002.
- [19] R. L. Lin, “Piezoelectric transformer characterization and application of electronic ballast,” *Ph.D. dissertation*, Virginia Polytechnic Institute and State University, USA, 2001.



- [20] E. M. Baker, D. Y. Huang, D. Y. Chen and F. C. Lee, "Radial mode piezoelectric transformer design for fluorescent lamp ballast application," *Proceeding of IEEE Power Electronics Specialists*, pp 1289–1294, 2002.
- [21] Y. H. Hsu, C. K. Lee, and W. H. Hsiao, "Electrical and mechanical fully coupled theory and experimental verification of Rosen-type piezoelectric transformers," *IEEE Transactions on Ultrasonics Ferroelectrics and Frequency Control*, vol. 52, pp. 1829-1839, 2005.
- [22] S. T. Ho, "Modeling of a disk-type piezoelectric transformer," *IEEE Transactions on Ultrasonics Ferroelectrics and Frequency Control*, vol. 54, pp. 2110-2119, Oct 2007.
- [23] J. H. Yang, "Piezoelectric transformer structural modeling - A review," *IEEE Transactions on Ultrasonics Ferroelectrics and Frequency Control*, vol. 54, pp. 1154-1170, Jun 2007.
- [24] W. C. Su and C. L. Chen, "ZVS for PT backlight inverter utilizing high-order current harmonic," *IEEE Transactions on Power Electronics*, vol. 23, pp. 4-10, Jan 2008.
- [25] S. Ben-Yaakov, M. Shvartsas, and S. Glozman, "Statics and dynamics of fluorescent lamps operating at high frequency: Modeling and simulation," *IEEE Transactions on Industry Applications*, vol. 38, pp. 1486-1492, Nov-Dec 2002.

- [26] S. Ben-Yaakov and M. M. Peretz, "Cold cathode fluorescent lamps driven by piezoelectric transformers: Stability conditions and thermal effect," *IEEE Transactions on Power Electronics*, vol. 22, pp. 761-768, 2007.
- [27] E. Deng, "I. Negative Incremental Impedance of Fluorescent Lamp," *Ph.D. dissertation*, California Institute of Technology, Pasadena, 1995.
- [28] E. Deng and S. Cuk, "Negative incremental impedance and stability of fluorescent lamp," *Proceeding of IEEE APEC'97*, pp. 1050–1056, 1997.
- [29] M. Yamamoto, Y. Sasaki, A. Ochi, T. Inoue, and S. Hamamura, "Step-down piezoelectric transformer for AC-DC converters," *Japanese Journal of Applied Physics*, vol. 40, pp. 3637-3642, 2001.
- [30] Y. P. Liu, D. Vasic, F. Costa, W. J. Wu and C. K. Lee, "Design of Fixed-Frequency Controlled Piezoelectric Transformers for DC/DC Converter Application", *Smart Materials and Structures*, Vol. 18, no.8, August 2009.
- [31] A. M. Sanchez, M. Sanz, R. Prieto, J. A. Oliver J A, P. Alou and J. A. Cobos , "Design of piezoelectric transformers for power converters by means of analytical and numerical methods" *IEEE Transactions on Industrial Electronics*, vol. 55, pp. 79–88, 2008.
- [32] J. M. Seo, H. W. Joo and H. K. Jung "Optimal design of piezoelectric transformer for high efficiency and high power density", *Sensors Actuators A*, vol.121, pp.

520–526, 2005

[33] S. Priya, "High power universal piezoelectric transformer," *IEEE Transactions on Ultrasonics Ferroelectrics and Frequency Control*, vol. 53, pp. 23-29, Jan 2006.

[34] M. Jin, M. Weiming, P Qijun, K Jun, Z. Lei, and Z. Zhihua, "Identification of essential Coupling path models for conducted EMI prediction in switching power converters," *IEEE Transactions on Power Electronics*, vol. 21, No. 6, pp. 1795-1803, November 2006.

[35] F. Lin and D. Y. Chen, "Reduction of Power Supply EMI Emission by Switching Frequency Modulation," *IEEE Transactions on Power Electronics*, vol. 9, pp. 132-137, 1994.

[36] S. Hamamura, T. Zaitzu, T. Ninomiya, and M. Shoyama, "Noise characteristics of piezoelectric transformer DC-DC converter", *IEEE PESC'1998*, Vol. 2, pp. 1262-1267, May 1998.

[37] J. Diaz, F. Nuno, J. M. Lopera, and J. A. Martin-Ramos, "A new control strategy for an AC/DC converter based on a piezoelectric transformer," *IEEE Transactions on Industrial Electronics*, vol. 51, pp. 850-856, Aug 2004.

[38] N. W. Hagood and A. Von Flotow, "Damping of Structural Vibrations with Piezoelectric Materials and Passive Electrical Networks," *Journal of Sound and Vibration*, Vol. 146, Issue. 2, pp. 243–68, April 1991.

[39] S. Y. Wu, "Method for Multiple Mode Shunt Damping of Structural Vibration using a Single PZT Transducer," *Proceedings of SPIE Smart Structures and Materials: Smart Structures and Intelligent Systems*, Vol. 3327, pp. 159–68, March 1998.

[40] C. H. Park and D. J. Inman, "Enhanced piezoelectric shunt design," *Shock and Vibration*, vol. 10, pp. 127-133, 2003.

[41] W. W. Clark, "Vibration Control with State-Switched Piezoelectric Materials," *Journal of Intelligent Material Systems and Structures*, Vol. 11, No. 4, pp. 263-271, 2000.

[42] C. Richard, D. Guyomar, D. Audigier, and H. Bassaler, "Enhanced Semi-Passive Damping using Continuous Switching of a Piezoelectric Device on an Inductor," *Proceedings of SPIE, Smart Structures and Materials: Damping and Isolation*, Vol. 3989, pp. 288-299, April 2000.

[43] E. Lefevre, A. Badel, L. Petit, C. Richard and D. Guyomar, "Semi-passive Piezoelectric Structural Damping by Synchronized Switching on Voltage Sources," *Journal of Intelligent Material Systems and Structures*, May 2006.

[44] L. R. Corr and W. W. Clark, "Comparison of low-frequency piezoelectric switching shunt techniques for structural damping," *Smart Materials and Structures*, Vol. 11, pp. 370–376, May 2002.

- [45] A. Badel, G. Sebald, D. Guyomar, M. Lallart, E. Lefeuvre, C. Richard, and J. Qiu, "Piezoelectric vibration control by synchronized switching on adaptive voltage sources: Towards wideband semi-active damping," *Journal of the Acoustical Society of America*, vol. 119, pp. 2815-2825, May 2006.
- [46] J. S. Yang and X. Zhang, "Analysis of a thickness-shear piezoelectric transformer," *International Journal of Applied Electromagnetics and Mechanics*, vol. 21, pp. 131-141, 2005.
- [47] J. L. Du, J. H. Hu, and K. J. Tseng, "Vibration distribution in output sections of a piezoelectric transformer operating at thickness shear mode," *IEEE Transactions on Ultrasonics Ferroelectrics and Frequency Control*, vol. 54, pp. 1984-1991, Oct 2007.
- [48] L. M. Xu, Y. Zhang, H. Fan, J. H. Hu, and J. S. Yang, "Theoretical Analysis of a Ceramic Plate Thickness-Shear Mode Piezoelectric Transformer," *IEEE Transactions on Ultrasonics Ferroelectrics and Frequency Control*, vol. 56, pp. 613-621, Mar 2009.
- [49] X. L. Chao, Z. P. Yang, G. Li, and Y. Q. Cheng, "Fabrication and characterization of low temperature sintering PMN-PZN-PZT step-down multilayer piezoelectric transformer," *Sensors and Actuators A-Physical*, vol. 144, pp. 117-123, May 2008.
- [50] T. Inoue, S. Hamamura, M. Yamamoto, A. Ochi, and Y. Sasaki, "AC-DC Converter

Based on Parallel Drive of Two Piezoelectric Transformers," *Japanese Journal of Applied Physics*, vol. 47, pp. 4011-4014, May 2008.





